ABSTRACT

Title of dissertation: CASIMIR-LIFSHITZ FORCES AND TORQUES

David A. T. Somers, Doctor of Philosophy, 2018

Dissertation directed by: Professor Jeremy Munday
Department of Physics

Quantum electromagnetic field fluctuations result in the well-documented Casimir-Lifshitz force between macroscopic objects. If the objects are anisotropic, theory predicts a corresponding Casimir-Lifshitz torque that causes the objects to rotate and align. In this work, we report the first measurements of the Casimir-Lifshitz torque, which confirm the predictions first made decades ago. The experimental design uses a nematic liquid crystal separated from a birefringent crystal by an isotropic Al_2O_3 layer with a thickness $\leq$ 25 nm. The molecular orientation of the liquid crystal is fixed with a rubbed counterplate, and, by varying the rubbing and Al_2O_3 thickness, we measured the Casimir-Lifshitz torque as a function of angle and distance.

Along the way, we developed a simpler formulation for calculating the Casimir-Lifshitz interaction in planar systems, which facilitated further theoretical study of the Casimir-Lifshitz torque. Using this method, we outline the conditions for a repulsive Casimir-Lifshitz force between birefringent materials that would allow for an angularly-dependent sign of the force. We also report an unexpected

enhancement of the torque from two sources: an intermediate dielectric medium and the finite speed of light.

CASIMIR-LIFSHITZ FORCES AND TORQUES

by

David A. T. Somers

Dissertation submitted to the Faculty of the Graduate School of the
University of Maryland, College Park in partial fulfillment
of the requirements for the degree of
Doctor of Philosophy
2018

Advisory Committee:
Professor Jeremy Munday, Chair/Advisor
Professor Ian Appelbaum
Professor Luz Martínez-Miranda
Professor Steven Rolston
Professor Victor Yakovenko

For Grandma

Acknowledgments

I owe thanks to many people for their contributions to this work and to my personal development. First, I would like to thank my dissertation committee: Professors Ian Appelbaum, Luz Martínez-Miranda, Steven Rolston, and Victor Yakovenko. I have worked with many talented researchers and good friends in the Munday group. I owe a special thank you to my fellow Casimir researcher and frequent collaborator, Joe Garrett, and to Joe Murray, who helped build the measurement apparatus. Of course, Jeremy Munday has also provided guidance and a unfailingly positive attitude, for which I am deeply grateful. Several undergraduate researchers assisted with this work and associated side projects, so I also owe thanks to Sean Gillen, Bart Tararuj, and Pat Goggins.

My family and friends have been constant sources of support over these years. To Mom, Dad, Kate, Ben, Marisa, Emmy, Zack, Grandpa, and extended family—thank you for reminding me what's really important. Thank you as well to all of the friends who kept me sane and happy throughout these years.

Thank you to the staff of IREAP, especially Dottie Brosius, Nancy Boone, Leslie Delabar, and Taylor Prendergast, who made sure I was paid, insured, and otherwise well-equipped. This research was only possible with support from the NanoCenter FabLab and its staff, especially John Abrahams and Tom Loughran, and the IREAP machine shop and its staff, especially Nolan Ballew. This work was supported by the National Science Foundation under Grant No. PHY-1506047.

Table of Contents

List of Tables

List of Figures

List of Abbreviations

ALD	Atomic layer deposition
IREAP	Institute for Research in Electronics and Applied Physics
LC	Liquid crystal (assumed to be nematic in this work)
MEMS	Microelectromechanical Systems
PE-CVD	Plasma-enhanced chemical vapor deposition
UV	ultraviolet
IR	infrared
PVA	polyvinyl alcohol
TE	Transverse electric
TM	Transverse magnetic

List of Variables

Chapter 1	
d	distance between two plates
F_c/A	Casimir force per unit area between two plates, as originally derived

Chapter 2	
ε	dielectric function of a material, usually evaluated at imaginary frequency
D	dispersion relation for surface modes in planar geometry (when $D = 0$)
D_n	dispersion relation at finite temperate for nth Matsubara number
n	whole number index used in Matsubara summation
T	temperature in Kelvin
ξ_n	Matsubara frequency, equal to $2\pi k_{\mathrm{B}}/\hbar$
r	radial component of a wavevector $\mathbf{k}$
φ	azimuthal component of a wavevector $\mathbf{k}$
$\boldsymbol{r}$	Fresnel reflection matrix
r_{ss},r_{sp},r_{ps},r_{pp}	Fresnel reflection coefficients for polarized light
f	thickness of an isotropic film covering an arbitrary dielectric
$\mathbf{k}$	wavevector
u	x-component of wavevector $\mathbf{k}$
v	y-component of wavevector $\mathbf{k}$
q	z-component of wavevector $\mathbf{k}$
ρ	z-component of a wavevector times $-\mathrm{i}$
ω	real frequency
ξ	frequency, used as $\varepsilon(\mathrm{i}\xi)$
ε	dielectric tensor
$\mathbf{F}$	eigenmode for electric field in a material, normalized so that F_x=1
F_y	y-component of $\mathbf{F}$
F_z	z-component of $\mathbf{F}$
r_D	common denominator of Fresnel reflection coefficients
$\mu, \Lambda, Q, g, h, \nu, \gamma$	simplifying substitutions in expressions for Fresnel reflection coefficient
k	$= \omega/c$ (wavenumber)
R_θ	rotation matrix of angle θ about z-axis

Chapter 3	
$\varepsilon_\perp$	ordinary dielectric coefficient
$\varepsilon_\parallel$	extraordinary dielectric coefficient
A_{Ham}	Hamaker coefficient
Ω	Helmholtz free energy per unit area of Casimir-Lifshitz interaction
F	Casimir-Lifshitz force per unit area
M	Casimir-Lifshitz torque per unit area
θ	angle between extraordinary axes of two birefringent materials

$A_{\mathrm{Ham},n}$	nth Matsubara term of Hamaker coefficient
C_{UV}	strength of UV oscillator in Ninham-Parsegian dielectric model
C_{IR}	strength of IR oscillator in Ninham-Parsegian dielectric model
ω_{UV}	frequency of UV oscillator in Ninham-Parsegian dielectric model
ω_{IR}	frequency of IR oscillator in Ninham-Parsegian dielectric model
A_0	$= A_{\mathrm{Ham}}(d=0)$, Nonretarded Hamaker constant
A_{NR}	$= A_{\mathrm{Ham}}(d=0)$, Nonretarded Hamaker constant
r_n	$= 2\sqrt{\varepsilon_3}\xi_n d/c$, dimensionless retardation factor of nth Matsubara term
δ_i	$= \frac{\varepsilon_i - \varepsilon_3}{\varepsilon_3}$ series expansion term for small birefringence of ith material
$\zeta(r_n)$	effect of retardation on the anisotropic Casimir-Lifshitz interaction for nth Matsubara term for weakly-birefringent materials

Chapter 4	
$\hat{\boldsymbol{n}}$	liquid crystal director
k_{11}	bend elastic constant for liquid crystals in Oseen-Frank theory
k_{22}	twist elastic constant for liquid crystals in Oseen-Frank theory
k_{33}	splay elastic constant for liquid crystals in Oseen-Frank theory
ϕ_x,ϕ_y	phase imparted by birefringent material along x- and $y-$axes
$\Delta\phi_x$	$= 2\pi\Delta n t/\lambda$, phase difference (retardance) imparted by birefringent material
λ	wavelength of visible light
M_{LC}	Jones matrix for liquid crystal layer

Chapter 5	
E_{elastic}	elastic energy per unit area associated with liquid crystal twist
M_{elastic}	torque associated with twist energy E_{elastic}
$A(d)$	$= M/\sin(2\theta)$torque coefficient per unit area
$I(\theta_a, \lambda)$	normalized intensity of light measured by spectrometer with analyzer angle θ_a at wavelength λ
θ_a	analyzer angle
$\Delta\theta$	$= \theta_{\mathrm{rub}} - \theta_1$ liquid crystal twist
θ_1	liquid crystal director direction near birefringent crystal
θ_{rub}	liquid crystal director direction near rubbed PVA layer

Chapter 6	
n	refractive index of a material, usually at optical frequencies
n_{o}	ordinary refractive index of a material
n_{e}	extraordinary refractive index of a material
d_j	Debye oscillator strength in Ninham-Parsegian dielectric model
τ_j	Debye relaxation time in Ninham-Parsegian dielectric model
f_j	oscillator strength in Ninham-Parsegian dielectric model
ω_j	oscillator frequency in Ninham-Parsegian dielectric model
g_j	oscillator damping term in Ninham-Parsegian dielectric model

Publications

The following works appear partially or entirely in this thesis:

> **D. A. T. Somers** and Jeremy N Munday. Rotation of a liquid crystal by the Casimir torque. *Physical Review A*, 91(3):032520, March 2015.
>
> **D. A. T. Somers** and Jeremy N. Munday. Conditions for repulsive Casimir forces between identical birefringent materials. *Physical Review A*, 95(2):022509, February 2017.
>
> **D. A. T. Somers** and Jeremy N. Munday. Casimir-Lifshitz Torque Enhancement by Retardation and Intervening Dielectrics. *Physical Review Letters*, 119(18):183001, November 2017.

I also contributed calculations of Casimir forces to the following works:

> J. L. Garrett, **D. Somers**, and J. N. Munday, *Journal of Physics: Condensed Matter* 27, 214012 (2015).
>
> J. L. Garrett, **D. A. T. Somers**, and J. N. Munday, *Physical Review Letters* 120, 040401 (2018).

Finally, the work outlined in Chapter 6 and Chapter 7 has been submitted to an academic journal:

> **Somers, D. A. T.**, Garrett, J. L., & Munday, J. N. Measurement of the Casimir Torque (in review).

Chapter 1: Introduction to Casimir-Lifshitz Interactions

1.1 Overview

In an introductory physics or chemistry course, students learn that charged particles of opposite sign are attracted while those of alike signs are repelled. Molecules or macroscopic objects experience an electrostatic force depending on their net charge, which depends on the number of stray electrons that have been added to or removed from the object. Beyond the static case, there exists an electromagnetic force between uncharged objects as well. This force arises from the random motion of negatively-charged electrons, which are relatively mobile compared to the positively-charged atomic nuclei. As two uncharged objects are brought near, the random motion of their electrons becomes correlated. That is, an instantaneous dipole in the first object causes an instantaneous dipole of opposite direction in the other. These anti-aligned dipoles contribute to an attractive force in the brief moment of their existence. This process happens continuously in bulk materials, but the resulting force is small compared to that between objects with a net charge.

In 1948, Casimir derived an attractive force between two uncharged, metallic plates at zero temperature caused by quantum fluctuations of the electromagnetic

field [1]. In his calculation, he considered the ground state free energy of an infinite number of modes confined by the metal boundaries. Although this energy is infinite, it changes by a finite amount as the plates are brought closer together. This results in a finite force per unit area:

$$F_c = -\frac{\pi^2 \hbar c}{240 d^4}, \tag{1.1}$$

where $\hbar$ is the reduced Planck constant, c is the speed of light in vacuum, and d is the separation between two plates. We can make sense of Eq. 1.1 with dimensional analysis: $\hbar$ has units of energy times time (eV s), c has units of speed ($\mathrm{m\,s^{-1}}$), and d has units of length (m). Together, $\hbar c/d^4$ has units of $\mathrm{eV\,m^{-3}} = \mathrm{N\,m^{-2}}$, or pressure.

The force between two uncharged atoms or molecules is known as the London force [2]. The London force is part of a family of intermolecular forces that includes the attraction between two randomly-oriented permanent dipoles (Keesom force) and between a permanent dipole and an uncharged molecule (Debye force) [3]. In chemistry, this group is often referred to as van der Waals forces, although sometimes this name refers to the London force only (and sometimes to additional forces as well). Before Casimir's derivation of the attractive force between conductors, Hamaker calculated the attractive force between bulk polarizable materials by integrating the molecular London force over spherical particles [4]. Casimir also helped to generalize the short-range London force to include the finite speed of light, the effect of which is referred to as retardation [5]. In the same work, he and coauthor Polder derived the force between a neutral

atom and a perfectly conducting plane, which is called the Casimir-Polder force [1].

The close connection between the London/van der Waals/Hamaker forces and the Casimir force was made explicit by Lifshitz in 1956 [6] (which was generalized in a follow-up work written with Dzyaloshinskii and Pitaevskii in 1961 [7]). He considered the simple geometry of three materials, two half-spaces separated by vacuum. He then added a randomly-fluctuating electric field to Maxwell's equations and solved for the stress tensor, thereby deriving an electromagnetic force. The resulting formulation can be used to calculate the dispersion force between arbitrary planar dielectrics, accounting for the materials' polarizability (*i.e.*, dielectric functions), temperature, and separation. The Casimir force is recovered in the case where the materials are perfect conductors ($\varepsilon \to \infty$ for all frequencies) and temperature is 0 K. Lifshitz's formulation also includes the effect of retardation, which generally weakens the force at larger separations.

The Casimir force between metals, the Casimir-Lifshitz force between dielectrics, the London force betwen neutral atoms, and the Casimir-Polder force between a plate and an atom all have the same underlying mechanism of randomly fluctuating electric fields. The difference in nomenclature refers to the geometry, material properties, and separation of the materials in question (see Table 1.1). Along with the London, Debye, and Keesom forces, the phrase "van der Waals force" often includes the Casimir, Casimir-Lifshitz, and Casimir-Polder forces as

[1] In the same work, they also derived the force between two neutral atoms (London force) in the retarded/long-range regime. In the literature, Casimir-Polder typically refers to the plate-particle geometry.

well. Several books have succinctly derived and described the Casimir-Lifshitz/van der Waals interactions from a variety of physical pictures [3, 8–10].

Table 1.1: Summary of some the nomenclature used to describe electromagnetic fluctuation forces between uncharged objects in various systems. The phrase "van der Waals force" is used ambiguously, but, depending on context, can refer to the entire table, the London, Debye, and Keesom forces, the London force alone, or all of these plus additional forces. When the separation distance d is small, retardation effects are usually ignored.

Name	Geometry	Objects	Distance	Power law of free energy
Casimir	plate-plate	ideal, uncharged conductors	large	d^{-3}
Casimir-Lifshitz	plate-plate	uncharged dielectrics	any	$d^{-2} \to d^{-3}$
Casimir-Polder	particle-plate	uncharged dielectrics	large	d^{-7}
London	particle-particle	induced dipole + induced dipole	small	d^{-6}
Debye	particle-particle	permanent dipole + induced dipole	small	d^{-6}
Keesom	particle-particle	permanent dipole + permanent dipole	small	d^{-6}

1.2 Casimir-Lifshitz torques

In 1972, Parsegian and Weiss calculated the nonretarded interaction between two anisotropic materials separated by a third anisotropic material as a function of their orientations [11]. Because the free energy depends on the relative orientation of the materials, there arises a torque that causes the materials to rotate. Barash later independently calculated the interaction between two anisotropic materials across an isotropic medium including retardation effects, a feat which required the solving of a homogeneous system of 18 equations by hand and resulted in a page-long expression [12]. A major result from the present work has been to simplify and generalize Barash's calculation, which has charitably been referred to as "very lengthy" [13] [2]. The Casimir torque in the planar geometry was rederived by van Enk [16], Kenneth and Nussinov [17], Shao [18], and Torres-Guzmán and Mochán [19, 20]. Several authors have derived the Casimir torque in other geometries and configurations, such as the torque between thin rods [21], ellipsoidal particles [22], metallic nanorods in fluid [23], corrugated metal plates [24], rotating, isotropic plates [25], and anisotropic layered media [26]. Dryden, Hopkins *et al.* have developed a free-to-use software package called "Gecko Hamaker" for the calculation of van der Waals effects with retardation, and have used it to study the effects of dielectric media, geometric anisotropy, optical anisotropy, and retardation [27, 28]. Several theoretical and numerical

[2] it has also been referred to as intractable [14] and "algebraically very complicated and untransparent, with little hope of a fundamental simplification" [15].

studies have suggested that the anisotropic van der Waals interaction can cause oriented adsorption of anisotropic particles on anisotropic substrates [29–31]. The nonretarded van der Waals torque is also believed to have an effect on liquid crystal alignment. We discuss the relevant literature in Section 4.4.

1.2.1 Proposed measurement methods

The field of Casimir force measurements is mature compared to theoretical discussions of Casimir-Lifshitz torques, let alone torque measurements. However, several groups have proposed various experiments that could feasibly measure the Casimir-Lifshitz torque. Munday *et al.* proposed an experiment that would measure the torque on microscopic disks of a birefringent crystal, such as lithium niobate ($LiNbO_3$) or calcite ($CaCO_3$) [32, 33]. The birefringent disks would float in ethanol above a birefringent plate, held in place by a balance of gravitational and repulsive Casimir forces. Chen and Spence calculated the effect of the Casimir torque on the oscillation of a torsion pendulum, and concluded that the torque could be measured with such a system [34]. Esquivel-Sirvent and Schatz suggested that the torque between $BaTiO_3$ slabs and arrays of silver nanoparticles could be measurable [35]. Guérout *et al.* designed an experiment in which a gold grating suspended by fibers would twist as it is lowered towards a second gold grating [36]. We proposed a liquid-crystal based experiment in 2015, the results of which comprise the latter part of this work [37]. Our experiment is similar in spirit to an earlier proposal by Smith and Ninham [38]. Xu and Li suggested that the torque on a nanorod suspended

above a birefringent with optical tweezers could be measured [39]. To the best of our knowledge, the only experiment that has been carried out to completion is our own, which is presented in Chapters 6 and 7.

1.3 Device applications

Currently, most research in the field of Casimir physics is either theoretical or focuses on precision measurements to check the validity of various approximations and models. However, some researchers have proposed potential applications in the field of Micro- and Nanoelectromechanical systems (MEMS/NEMS). Capasso wrote a review that included many such devices that could operate using Casimir forces and torques [40]. Chan *et al.* have constructed a number of on-chip MEMS devices that measure or use the Casimir force [41–43]. Emig suggested that the Casimir force could be used in a microscopic ratchet device [44]. Sheehan suggested that the Casimir-Lifshitz interaction could even catalyze chemical reactions [45]. The Casimir force can also cause unwanted stiction in MEMS devices [46], which helped motivate measurements of a repulsive Casimir force [47]. In nature, the van der Waals/Casimir-Lifshitz force is the means by which geckos' feet stick to surfaces [48]. Because this work represents the first Casimir torque measurements, there are relatively few device designs that employ it. But, for example, the Casimir torque could potentially be used for non-contact power transmission in a MEMS or NEMS device.

1.4 Anisotropic Casimir force

There have been several studies on the effect of anisotropy on the Casimir force, beginning with Parsegian's pioneering work that predicts an orientation-dependent sign of the force [11]. In Chapter 3, we expand on Parsegian's work and outline the necessary conditions for Casimir repulsion in planar, anisotropic systems [49]. Romanowsky *et al.* predicted a strongly-dependent orientation effect [50], and Banishev *et al.* measured the angular dependence of the force between corrugated plates [51]. In other theoretical works, Shao *et al.* considered the combined effects of anisotropy and magnetic permeability [52], and Rosa *et al.* and Zeng *et al.* considered the force between anisotropic metamaterials [53, 54].

Chapter 2: Calculation of Casimir-Lifshitz free energy in planar systems

2.1 Overview

Two objects experience a Casimir-Lifsthiz force whenever the free energy of the fluctuating electromagnetic fields depends on the separation of the objects. Analogously, a torque exists whenever the free energy depends on the relative orientation of the objects. This requires the materials to have either optical or geometric anisotropy. The effects of optical and geometric anisotropy are intertwined, but in this work we limit our focus to optically anisotropic systems only. In particular, we consider planar slabs separated by an isotropic medium (Fig. 2.1). The planar slabs can be layered media and have any thickness in the $z-$direction but must be uniform and infinite in the xy-plane. We also assume that the materials are indistinguishable from vacuum to magnetic fields ($\mu(\omega) = 1$) and consider the electric field contributions only. The Helmholtz free energy per unit area is typically written in terms of a dispersion equation $D(\omega) = 0$ for surface waves (those that decay exponentially away from the interface) [11]. That is, after writing out Maxwell's equations with the appropriate boundary conditions

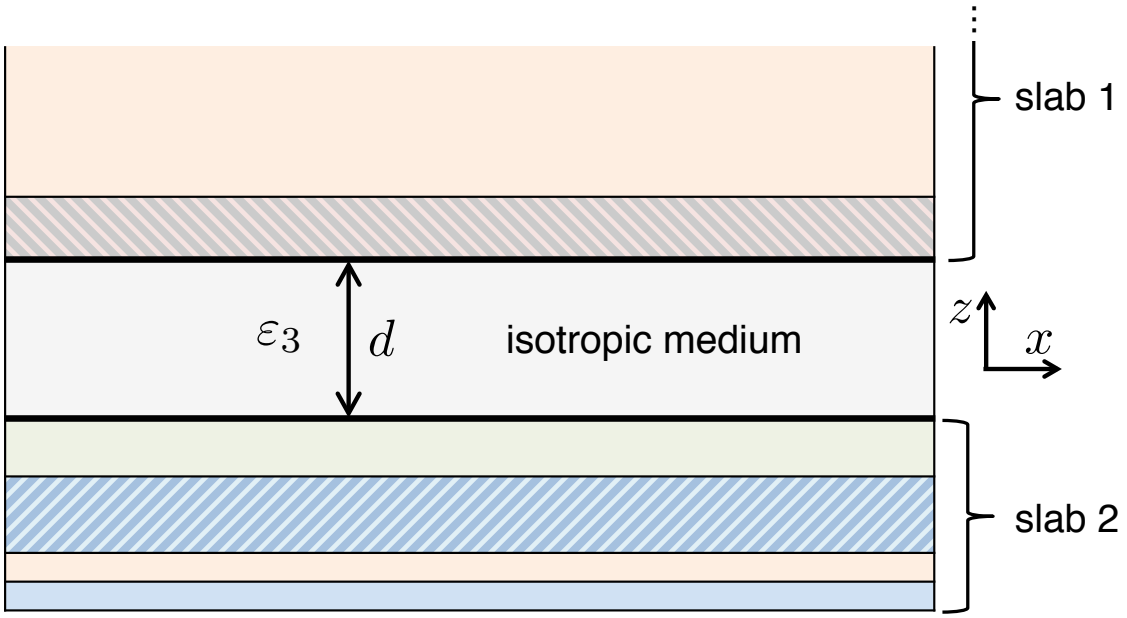

Figure 2.1: We calculate the Casimir-Lifshitz interaction between two slabs of infinite expanse in the xy-plane separated by an isotropic medium. The slabs can be optically anisotropic, layered, and arbitrarily thick (slab 1 continues indefinitely in the $z-$direction), so long as the reflection coefficients of polarized light from their surface can be calculated.

for some configuration of materials, the resulting equations can be combined into one and rearranged into the form $D(\omega) = 0$. At zero temperature, the free energy (per unit area, here and throughout this work) is [20]

$$\Omega_{0\,\mathrm{K}}(d) = \frac{\hbar}{8\pi^3} \int_0^\infty \mathrm{d}\xi \int_0^\infty r\mathrm{d}r \int_0^{2\pi} \mathrm{d}\varphi \log D(d, r, \varphi, \xi), \tag{2.1}$$

where r and φ are azimuthal components of a wavevector, $\xi = \mathrm{i}\omega$ is a complex frequency, and $D(d, r, \varphi, \xi) = 0$ represents the dispersion condition. At finite temperatures, the integral over ξ becomes a finite sum evaluated at complex

frequencies $\mathrm{i}\xi_n = \mathrm{i}n\,(2\pi k_B T/\hbar)$:

$$\Omega(d) = \frac{k_B T}{4\pi^2} {\sum_{n=0}^{\infty}}' \int_0^\infty r\mathrm{d}r \int_0^{2\pi} \mathrm{d}\varphi \log D_n(d, r, \varphi), \tag{2.2}$$

where the prime on the summation indicates that the $n = 0$ term is to be halved. Curiously, Eq. 2.2 exactly corresponds to a trapezoidal integration of Eq. 2.1 with variable transform $\mathrm{d}\xi \to \mathrm{d}n\,(2\pi k_B T/\hbar)$, with abscissae spacing proportional to T [55]. The effect of temperature is mathematically equivalent to the error of a left Riemann sum integration.

For any real material, the integral over ξ (or sum over n at finite temperature) converges because all materials are transparent beyond some frequency, which is manifest by a decay of $D_n(\xi)$ to 0 as $\xi \to \infty$. As T increases, the $n = 0$ term contributes a larger and larger fraction to the total interaction as the $D_n(n > 0)$ terms are evaluated at higher and higher frequencies.

The rest of this chapter is dedicated to relatively simple expressions for D_n, which for decades has been a source of anguish for any researcher studying the Casimir-Lifshitz torque.

2.2 Dispersion relation for planar systems

Lambrecht *et al.*, following the work of Kats [56], demonstrated that the dispersion relation in the Casimir-Lifshitz calculation can be written in terms of the Fresnel reflection matrices of the two surfaces that bound the medium of thickness d [57]:

$$D_n = \det\left(\mathbf{1} - \boldsymbol{r}_1 \boldsymbol{r}_2 e^{-2\rho_3 d}\right) \tag{2.3a}$$

$$\boldsymbol{r}_i = \begin{pmatrix} r_{ss,i} & r_{sp,i} \\ r_{ps,i} & r_{pp,i} \end{pmatrix}, \tag{2.3b}$$

where d is the distance between the two materials, ρ_3 is the z-component of the $\boldsymbol{k}$-vector in the intervening medium, r_{sp} indicates the ratio of the reflected electric field with $s-$polarization (transverse electric, or TE) to an incident electric field with $p-$polarization (transverse magnetic, or TM) (and likewise for r_{ss}, r_{pp}, and r_{ps}), and the index i refers to the interface between the ith slab and the isotropic medium. Torres-Guzmán and Mochán rederived the same result, explicitly including anisotropic materials [20]. This formulation clarifies the connection between Casimir's derivation of the force with Lifshitz's bulk calculation: even though Lifshitz considered field fluctuations in infinitely thick materials, the calculated force depends only on the reflection at the boundaries between the materials and the intervening dielectric medium (Fig. 2.2).

In fact, Torres-Guzmán's effective cavity approach allows for a relatively simple calculation of any planar Casimir-Lifshitz interaction across an isotropic medium. Whether the interacting materials are anisotropic, layered, or inhomogenous, the Casimir-Lifshitz free energy can be calculated using Eq. 2.3 for any materials whose properties are independent of x and y. Fresnel reflection coefficients for various systems can be determined analytically; for example, Lekner has calculated them for uniaxial materials with arbitrarily rotated axes [58]. The calculation is complicated but not intractable when the intervening medium is anisotropic: a similar procedure can be used with the new eigenmodes of the medium (which will no longer be

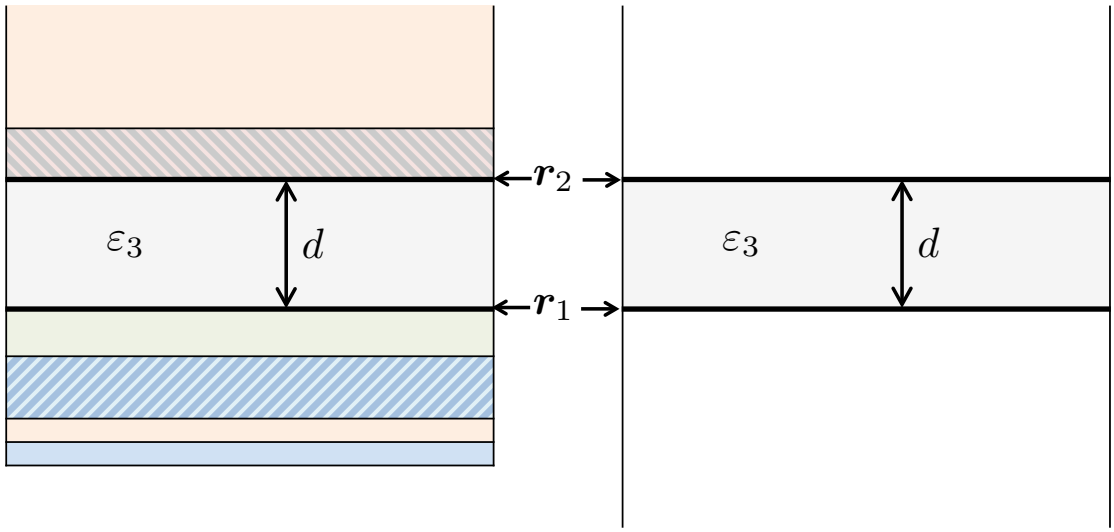

Figure 2.2: Effective cavity model for Casimir-Lifshitz interactions. The dispersion relation used to calculate the Casimir-Lifshitz interaction depends on the Fresnel reflection matrices
bmr_1 and $\boldsymbol{r}_2$ at the interfaces of the isotropic medium. These matrices can be calculated independently for the two slabs in order to find the dispersion relation.

TE and TM waves). This is the method used by Jiang and Wilczek to derive a repulsive, switchable Casimir force between conductors separated by an optically active medium with circularly-polarized eigenmodes [59].

Our strategy for generating expressions for the Casimir-Lifshitz free energy between thick slabs is as follows:

1. calculate the Fresnel reflection matrices from the formulae below

2. transform the expressions into the laboratory coordinate frame (if, for example, one material is to be rotated)

3. compute the Casimir-Lifshitz free energy using Eqs. 2.2 and 2.3.

2.3 Fresnel reflection coefficients

In the following sections, we calculate the reflection coefficients for a system of experimental relevance: a thick, homogeneous, nonmagnetic material with arbitrary dielectric tensor covered with an isotropic film of thickness f (Fig. 2.3). We then apply various simplifications to the somewhat complicated result. Following the method of Lekner [58], the reflection coefficients can be written in terms of the polarization eigenmodes of the anisotropic material. We note that

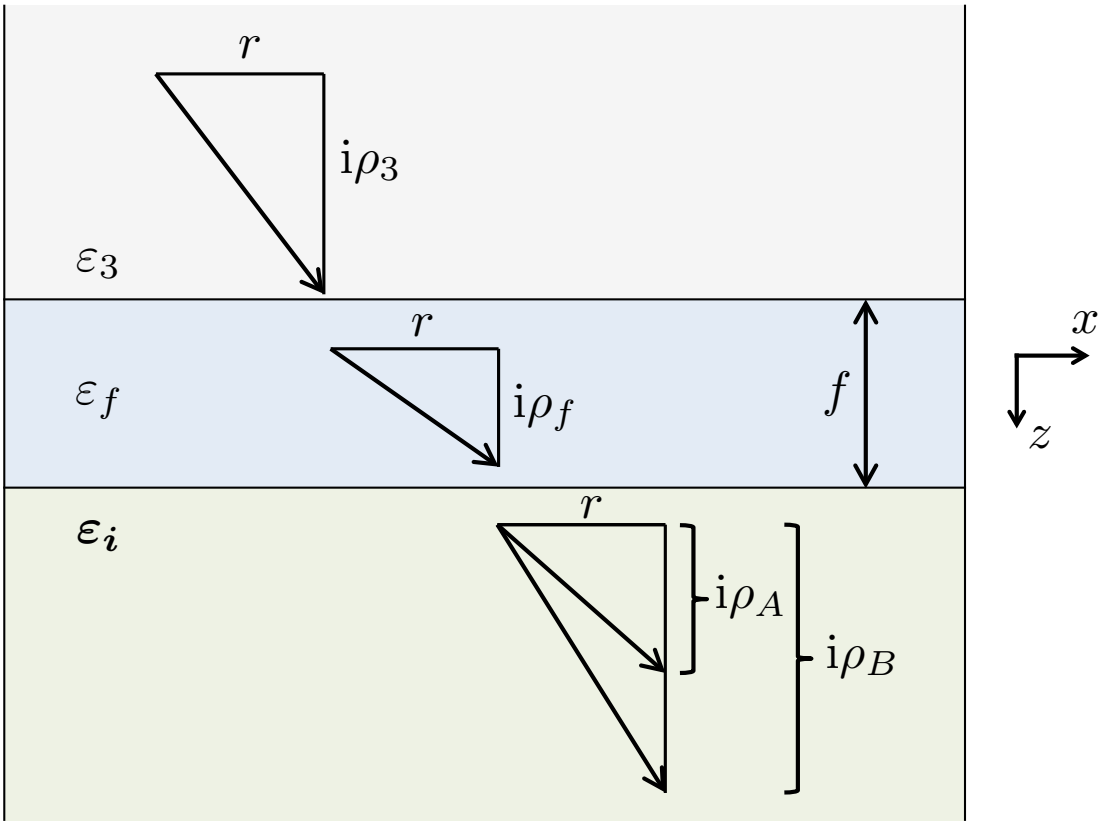

Figure 2.3: Isotropic film on an arbitrary, uniform dielectric. The Fresnel reflection matrix $\boldsymbol{r}_i$ between materials 3 and the film of thickness f can be combined with a second interface to calculate the Casimir-Lifshitz interaction between two dielectrics with films.

most derivations of Fresnel reflection coefficients (such as Lekner's) assume waves

that propagate in z rather than decay. To convert between the two, the z-component of the eigenmodes and wavevector must be multiplied or divided by i. That is, if the wavevector is derived for incoming wave $\boldsymbol{k} = (u, v, q)$, then we substitute $q = \mathrm{i}\rho$. As derived by Barash, $\rho_i = \sqrt{r^2 - \varepsilon_i k}$ for an isotropic material, where $k = \omega/c$ is the wavenumber in vacuum and $r = \sqrt{u^2 + v^2}$ is the radial component of the wavevector. In anisotropic materials, there are two eigenmodes with different wavevectors. Though they are referred to as the fast and slow wave, we denote their z-components as ρ_A and ρ_B. In a uniaxial system, these correspond to ordinary and extraordinary waves.

2.3.1 Arbitrary anisotropic material with isotropic film

Consider a homogeneous, nonmagnetic material with arbitrary dielectric tensor $\boldsymbol{\varepsilon_i}$ (which physically must be symmetric). Let the (unnormalized) eigenmodes be of the form $\boldsymbol{F}_A \sim \left(1, F_y^A, F_z^A\right)$ and $\boldsymbol{F}_B \sim \left(1, F_y^B, F_z^B\right)$. The reflection coefficients, which share the common denominator r_{D}, are then:

$$r_{sp} r_{\mathrm{D}} = +\,2\mathrm{i}k\sqrt{\varepsilon_3}\rho_3 \left[\mathrm{i}r(F_z^A - F_z^B) + \left(\rho_A - \rho_B\right)\right] \operatorname{sech}^2\left(f\rho_f\right) \tag{2.4a}$$

$$r_{ps} r_{\mathrm{D}} = -\,2\mathrm{i}k\sqrt{\varepsilon_3}\rho_3 F_y^A F_y^B \left(\rho_A - \rho_B\right) \operatorname{sech}^2\left(f\rho_f\right) \tag{2.4b}$$

$$\begin{aligned} r_{ss} r_{\mathrm{D}} = &+ F_y^A \left[\Lambda_-^A + Q_-^A \tanh\left(f\rho_f\right)\right] \left[g_-^B + \mathrm{i}F_z^B r\rho_3 - \left(h_-^B - \mathrm{i}F_z^B\mu\right)\tanh\left(f\rho_f\right)\right] \\ &- F_y^B \left[\Lambda_-^B + Q_-^B \tanh\left(f\rho_f\right)\right] \left[g_-^A + \mathrm{i}F_z^A r\rho_3 - \left(h_-^A - \mathrm{i}F_z^A\mu\right)\tanh\left(f\rho_f\right)\right] \end{aligned} \tag{2.4c}$$

$$r_{pp}r_{\mathrm{D}} = -F_y^A\left[\Lambda_+^A + Q_+^A\tanh\left(f\rho_f\right)\right]\left[g_+^B + \mathrm{i}F_z^B r\rho_3 - \left(h_+^B + \mathrm{i}F_z^B\mu\right)\tanh\left(f\rho_f\right)\right]$$
$$+ F_y^B\left[\Lambda_+^B + Q_+^B\tanh\left(f\rho_f\right)\right]\left[g_+^A + \mathrm{i}F_z^A r\rho_3 - \left(h_+^A + \mathrm{i}F_z^A\mu\right)\tanh\left(f\rho_f\right)\right] \tag{2.4d}$$

$$r_{\mathrm{D}} = +F_y^A\left[\Lambda_+^A + Q_+^A\tanh\left(f\rho_f\right)\right]\left[g_-^B + \mathrm{i}F_z^B r\rho_3 - \left(h_-^B - \mathrm{i}F_z^B\mu\right)\tanh\left(f\rho_f\right)\right]$$
$$- F_y^B\left[\Lambda_+^B + Q_+^B\tanh\left(f\rho_f\right)\right]\left[g_-^A + \mathrm{i}F_z^A r\rho_3 - \left(h_-^A - \mathrm{i}F_z^A\mu\right)\tanh\left(f\rho_f\right)\right] \tag{2.4e}$$

with

$$\mu = r\rho_f\varepsilon_3/\varepsilon_f \tag{2.5a}$$

$$\Lambda_\pm^i = \rho_3 \pm \rho_i \tag{2.5b}$$

$$Q_\pm^i = \rho_3\rho_i/\rho_f \pm \rho_f \tag{2.5c}$$

$$g_\pm^i = \rho_3\rho_i \pm \varepsilon_3 k^2 \tag{2.5d}$$

$$h_\pm^i = \varepsilon_f k^2\rho_3/\rho_f \pm \varepsilon_3\rho_i\rho_f/\varepsilon_f. \tag{2.5e}$$

The eigenmodes $\boldsymbol{F}_A$ and $\boldsymbol{F}_B$ themselves are algebraically unwieldy for arbitrary biaxial materials, but nevertheless are analytically solvable. We will focus our attention on in-plane uniaxial materials, which represent the experimental reality of our measurements.

2.3.1.1 Removal of the film

The forms of Eqs. 2.4 and 2.5 permit immediate removal of the isotropic film, yielding the reflection coefficients for a thick, uniform, arbitrary dielectric. By setting $f = 0$, $\tanh(\rho_f f) = 0$, and $\operatorname{sech}(\rho_f f) = 1$, the simplified reflection coefficients are

$$r_{sp} r_{\mathrm{D}} = +\,2\mathrm{i}k\sqrt{\varepsilon_3}\rho_3 \left[\mathrm{i}r(F_z^A - F_z^B) + \big(\,\rho_A - \rho_B\,\big)\right] \tag{2.6a}$$

$$r_{ps} r_{\mathrm{D}} = -\,2\mathrm{i}k\sqrt{\varepsilon_3}\rho_3 F_y^A F_y^B \left(\rho_A - \rho_B\right) \tag{2.6b}$$

$$r_{ss} r_{\mathrm{D}} = +\,F_y^A \Lambda_-^A \left(g_-^B + \mathrm{i}F_z^B r\rho_3\right) - F_y^B \Lambda_-^B \left(g_-^A + \mathrm{i}F_z^A r\rho_3\right) \tag{2.6c}$$

$$r_{pp} r_{\mathrm{D}} = -\,F_y^A \Lambda_+^A \left(g_+^B + \mathrm{i}F_z^B r\rho_3\right) + F_y^B \Lambda_+^B \left(g_+^A + \mathrm{i}F_z^A r\rho_3\right) \tag{2.6d}$$

$$r_{\mathrm{D}} = +\,F_y^A \Lambda_+^A \left(g_-^B + \mathrm{i}F_z^B r\rho_3\right) - F_y^B \Lambda_+^B \left(g_-^A + \mathrm{i}F_z^A r\rho_3\right). \tag{2.6e}$$

2.3.2 Polarization eigenmodes for in-plane uniaxial material

For a uniaxial birefringent material with its optical axis in the xy-plane, the dielectric tensor is of the form

$$\boldsymbol{\varepsilon}_i = R_{\theta_i} \begin{pmatrix} \varepsilon_{i\parallel} & 0 & 0 \\ 0 & \varepsilon_{i\perp} & 0 \\ 0 & 0 & \varepsilon_{i\perp} \end{pmatrix} R_{\theta_i}^{-1}, \tag{2.7}$$

where R_{θ_i} is the rotation matrix of angle θ_i about the z-axis. The incident ray is in the xz-plane, so that θ_i represents the angle between the incident ray and the optical axis of the crystal. As derived by Lekner, the polarization eigenmodes and

$\rho's$ in such a material are of the form

$$\boldsymbol{F}_A \sim (1, -\cot(\theta_i), \mathrm{i}r/\rho_A) \tag{2.8a}$$

$$\boldsymbol{F}_B \sim \left(1, -\varepsilon_{i\perp}\tan(\theta_i)\, k^2/\rho_A^2, \mathrm{i}r\rho_B/\rho_A^2\right) \tag{2.8b}$$

$$\rho_A = \sqrt{r^2 - \varepsilon_{i\perp}k^2} \tag{2.8c}$$

$$\rho_B = \sqrt{r^2 - \varepsilon_{i\parallel}k^2 + \left(\varepsilon_{i\parallel}/\varepsilon_{i\perp} - 1\right) r^2\cos^2\theta_i} \tag{2.8d}$$

where, in this case, ρ_A is the ordinary ray and ρ_B is the extraordinary ray.

2.3.3 Isotropic materials, with and without a film

For isotropic materials, there are two degenerate ordinary waves. It is clear upon examination of Eq. 2.4 that naïve substitution of $B \to A$ will yield nothing. A careful derivation yields the same result as simply striking out the second (or first) term in each sum for Eqs 2.4c–e. On physical grounds, there should be no polarization mixing from an isotropic surface, so the off-diagonal terms in the Fresnel reflection matrix are 0. After some simplification, we find

$$r_{sp} = r_{ps} = 0 \tag{2.9a}$$

$$r_{ss} = \frac{\Lambda_-^A + Q_-^A\tanh(f\rho_f)}{\Lambda_+^A + Q_+^A\tanh(f\rho_f)} \tag{2.9b}$$

$$r_{pp} = \frac{g_+^A + \mathrm{i}F_z^A r\rho_3 - \left(h_+^A + \mathrm{i}F_z^A\mu\right)\tanh(f\rho_f)}{g_-^A + \mathrm{i}F_z^A r\rho_3 - \left(h_-^A - \mathrm{i}F_z^A\mu\right)\tanh(f\rho_f)}. \tag{2.9c}$$

Again setting $f = 0$ to remove the film, these reduce (after substitutions) to the well-known expressions

$$r_{sp} = r_{ps} = 0 \tag{2.10a}$$

$$r_{ss} = \frac{\rho_3 - \rho_A}{\rho_3 + \rho_A} \tag{2.10b}$$

$$r_{pp} = \frac{\varepsilon_3\rho_A - \varepsilon_A\rho_3}{\varepsilon_3\rho_A + \varepsilon_A\rho_3}. \tag{2.10c}$$

We note that an overall $(-)$ sign may appear in expressions for r_{pp} in other works; this is merely a sign convention and has no effect on any calculated results.

2.4 In-plane uniaxial materials

To demonstrate the utility of this method, we pause here to derive the Casimir-Lifshitz free energy for the system considered by Barash (two uniaxial, birefringent half-spaces with extraordinary axes in $xy-$plane, separated by an isotropic medium). This formulation was first published in [49] with slightly different notation. Using the polarization eigenmodes and wavevectors from Eq. 2.8 and the film-free Fresnel coefficients from Eq. 2.6,

$$r_{sp}r_{\mathrm{D}} = r_{ps}r_{\mathrm{D}} = k\sqrt{\varepsilon_3}\varepsilon_\perp\rho_A\rho_3\left(\rho_A - \rho_B\right)\sin\left(2\theta_i\right) \tag{2.11a}$$

$$r_{ss}r_{\mathrm{D}} = \quad \sin^2\left(\theta_i\right)\Lambda_-^B\gamma_+ + \cos^2\left(\theta_i\right)\Lambda_-^A\nu_+ \tag{2.11b}$$

$$r_{pp}r_{\mathrm{D}} = -\sin^2\left(\theta_i\right)\Lambda_+^B\gamma_- + \cos^2\left(\theta_i\right)\Lambda_+^A\nu_- \tag{2.11c}$$

$$r_{\mathrm{D}} = \quad \sin^2\left(\theta_i\right)\Lambda_+^B\gamma_+ + \cos^2\left(\theta_i\right)\Lambda_+^A\nu_+, \tag{2.11d}$$

where we have introduced the substitutions

$$\nu_\pm = \varepsilon_3\rho_A^3 \pm \varepsilon_\perp\rho_A\rho_B\rho_3 \tag{2.12a}$$

$$\gamma_\pm = \varepsilon_\perp k^2\left(\varepsilon_\perp\rho_3 \pm \varepsilon_3\rho_A\right). \tag{2.12b}$$

This represents the $\boldsymbol{r}$-matrix for one material. To combine two materials in Eq. 2.3 to calculate the Casimir-Lifshitz free energy using Eq. 2.2, we write out the

$\boldsymbol{r}$-matrix for each material, using the appropriate dielectric functions. It is convenient to set the optical axis of the first material along x, such that $\theta_1 = \varphi$ (the azimuthal direction of the integrated wavevector) and $\theta_2 = \varphi + \theta$, where θ is now the relative twist between the two materials' optical axes. This formulation produces an algebraically equivalent expression to Barash's but is more transparent and easily implemented in just a few lines of code.

2.5 Summary of Casimir-Lifshitz calculations for planar systems

With Equations 2.2, 2.3, and Fresnel reflection coefficients from Section 2.3 (or from any other method), one can calculate the Casimir-Lifshitz free energy in the planar geometry with relative ease. Though the calculation is still somewhat cumbersome, this formulation is modular, more general, and massively simplified from Barash's expression, which was used from 1978 to the present day. This formulation led to new insights in the field of Casimir physics, some of which are outlined in the next chapter.

Chapter 3: Forces and torques in anisotropic systems

3.1 Overview

The formulation in the previous chapter permits the calculation of Casimir-Lifshitz interactions for complex planar systems and allows for the exploration of interesting phenomena. One feature, first noted by Parsegian and Weiss in the nonretarded calculation [11], is the possibility of a free energy with an orientation-dependent sign. In plain terms, they demonstrated that, with an appropriate intervening dielectric, anisotropic materials could switch between an attractive and repulsive Casimir-Lifshitz force by rotating. We discuss this phenomenon in further detail in [49], outlining the necessary conditions for the attractive/repulsive transition. The intervening dielectric can also enhance the Casimir-Lifshitz torque significantly. We first reported this effect in [60]. In the same work, we examined the surprising effect of retardation in anisotropic systems. Like the dielectric medium, retardation is usually assumed to weaken Casimir-Lifshitz interactions of all kinds. However, we found that the torque is generally enhanced by retardation at the experimentally accessible separations of 0–40 nm. In this chapter, we summarize the results from [49, 60].

3.2 Conditions for repulsive Casimir forces between identical birefringent materials

The work in this section was originally published in [49]. Because attractive Casimir-Lifshitz forces can cause stiction in MEMS or NEMS devices [46], there has been significant effort to engineer systems that exhibit Casimir-Lifshitz repulsion. So far, repulsion has only been measured between two dissimilar materials separated by a third material which has a dielectric response intermediate to the other materials [47, 61]. Some theoretical works have proposed other systems that could exhibit Casimir repulsion. The most common approach among these includes metamaterials with strong magnetic responses at optical frequencies, such as in [62–65]. Rosa *et al.* considered uniaxial out-of-plane metamaterials (among other anisotropic materials), but focused on planar systems separated by vacuum [53]. These systems all require at least one of the plates to have a strong magnetic response. There have also been numerical and analytical studies of geometries that could produce repulsion between metals separated by vacuum, but these systems are unstable to lateral perturbations and therefore difficult to realize experimentally [66, 67]. Deng *et al.* predicted an attractive-repulsive transition of the force between an aligned, uniaxial, in-plane material and a conducting surface separated by vacuum as a function of distance [68]. This system also relies on the magnetic response of the plates to produce repulsion.

However, there is another less commonly discussed system that exhibits

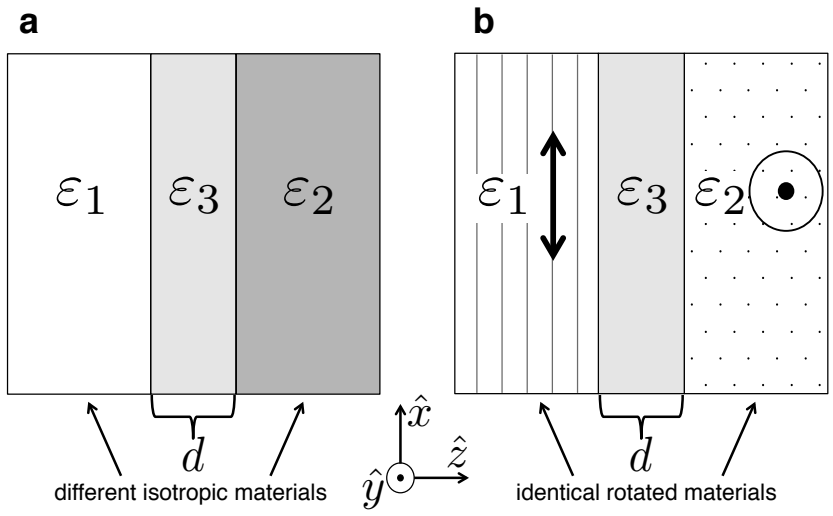

Figure 3.1: Schematic of the systems under investigation. Two infinite dielectric slabs interact across a third dielectric of width d. We compare the Casimir-Lifshitz interaction in (a) the case of two isotropic slabs with dielectric functions ε_1 and ε_2 to (b) the case with two identical birefrigent materials with dielectric function $\varepsilon_{\parallel}$ along the principal axis and $\varepsilon_{\perp}$ in the other directions. In (b) the optical axis for material one is along the x-axis while that of material two is rotated by $\theta = \pi/2$.

Casimir repulsion: nonmagnetic dielectrics with uniaxial in-plane birefringence separated by a dielectric medium, as first noted in [11]. For this case, two *identical* materials can exhibit Casimir-Lifshitz repulsion under specific orientations. Although two planar dielectric bodies with reflective symmetry are almost always attracted [69], a rotational displacement between the two anisotropic materials breaks the reflective symmetry of the system. The force is always attractive when the axes of symmetry are aligned, but can become repulsive when the symmetry is broken. Here we expand on [11] to outline the conditions for which Casimir-Lifshitz repulsion may occur for two identical, anisotropic materials.

3.2.1 Nonretarded Hamaker coefficients for anisotropic systems

We consider two identical, semi-infinite slabs of uniaxial birefringent materials with optical axes in the $xy-$plane, but rotated with respect to each other (Fig. 3.1b). Their permittivity tensors are:

$$\boldsymbol{\varepsilon_1} = \begin{pmatrix} \varepsilon_\parallel & 0 & 0 \\ 0 & \varepsilon_\perp & 0 \\ 0 & 0 & \varepsilon_\perp \end{pmatrix}, \tag{3.1a}$$

$$\boldsymbol{\varepsilon_2} = \begin{pmatrix} \varepsilon_\parallel \cos^2\theta + \varepsilon_\perp \sin^2\theta & (\varepsilon_\perp - \varepsilon_\parallel)\sin\theta\cos\theta & 0 \\ (\varepsilon_\perp - \varepsilon_\parallel)\sin\theta\cos\theta & \varepsilon_\parallel \sin^2\theta + \varepsilon_\perp \cos^2\theta & 0 \\ 0 & 0 & \varepsilon_\perp \end{pmatrix}, \tag{3.1b}$$

where θ is the relative angle between the optical axes of the materials. When their axes are aligned, $\theta = 0$ and $\boldsymbol{\varepsilon_1} = \boldsymbol{\varepsilon_2}$. The Helmholtz free energy per unit area of this system can be calculated using the methods of Chapter 2. In the nonretarded limit (corresponding to the van der Waals regime), the Casimir-Lifshitz free energy per unit area is often expressed in terms of a Hamaker constant A_{Ham}, which is independent of d:

$$\Omega(d,\theta) = -\frac{A_{\text{Ham}}}{12\pi d^2}, \tag{3.2}$$

resulting in a force given by

$$F(d,\theta) = -\frac{\partial\Omega(d,\theta)}{\partial d} = -\frac{A_{\text{Ham}}}{6\pi d^3}. \tag{3.3}$$

The sign of the Hamaker coefficient gives the sign of the force, with $A_{\text{Ham}} > 0$ indicating attraction and $A_{\text{Ham}} < 0$ indicating repulsion.

The dispersion condition can be written as a function of the Fresnel reflection matrices of the two interfaces. In the nonretarded approximation, $r_i^{ss} = r_i^{sp} = r_i^{ps} = 0$, and only r_i^{pp} (corresponding to TM modes) remains, so that:

$$D_n = 1 - r_1^{pp} r_2^{pp} e^{-2\rho_3 d}, \tag{3.4a}$$

$$r_i^{pp} = \frac{\varepsilon_3 - \varepsilon_\perp \sqrt{1 + \left(\varepsilon_\parallel/\varepsilon_\perp - 1\right)\cos^2\left(\theta_i + \varphi\right)}}{\varepsilon_3 + \varepsilon_\perp \sqrt{1 + \left(\varepsilon_\parallel/\varepsilon_\perp - 1\right)\cos^2\left(\theta_i + \varphi\right)}}, \tag{3.4b}$$

where $\theta_1 = 0$, $\theta_2 = \theta$, and φ is an integration variable. In this approximation, the integral over r can be carried out analytically, and the nonretarded Casimir-Lifshitz interaction energy per unit area is proportional to $1/d^2$.

The three dielectric constants in r_i^{pp} can be expressed in terms of two variables, such as $\varepsilon_\parallel/\varepsilon_3$ and $\varepsilon_\perp/\varepsilon_3$. Using Eq. 3.4a, the integral over r in Eq. 2.2 can be performed analytically, and we can write the Hamaker coefficient as a sum of contributions from each Matsubara frequency:

$$A_{\mathrm{Ham}} = {\sum_{n=0}^{\infty}}' A_{\mathrm{Ham},n}, \tag{3.5a}$$

$$A_{\mathrm{Ham},n} = \frac{3k_{\mathrm{B}}T}{4\pi} \int_0^{2\pi} \mathrm{d}\varphi \ \mathrm{Li}_3\left(r_1^{pp} r_2^{pp}\right), \tag{3.5b}$$

where Li_3 is the third-order polylogarithm function. The integration over φ is carried out numerically as a function of the ratios $\varepsilon_\parallel/\varepsilon_3$ and $\varepsilon_\perp/\varepsilon_3$ in Fig. 3.2.

The total Hamaker coefficient can be found by summing the values of the dielectric functions at each of the Matsubara frequencies. For comparison, we also consider the interaction between isotropic materials with $\varepsilon_1 = \varepsilon_\parallel$ and $\varepsilon_2 = \varepsilon_\perp$ (Fig. 3.1a). The nonretarded free energy is given by Eq. 3.5, with $r_{i,\mathrm{iso}}^{pp} = \frac{\varepsilon_i - \varepsilon_3}{\varepsilon_i + \varepsilon_3}$. This expression yields Dzyaloshinskii's condition for repulsion between isotropic

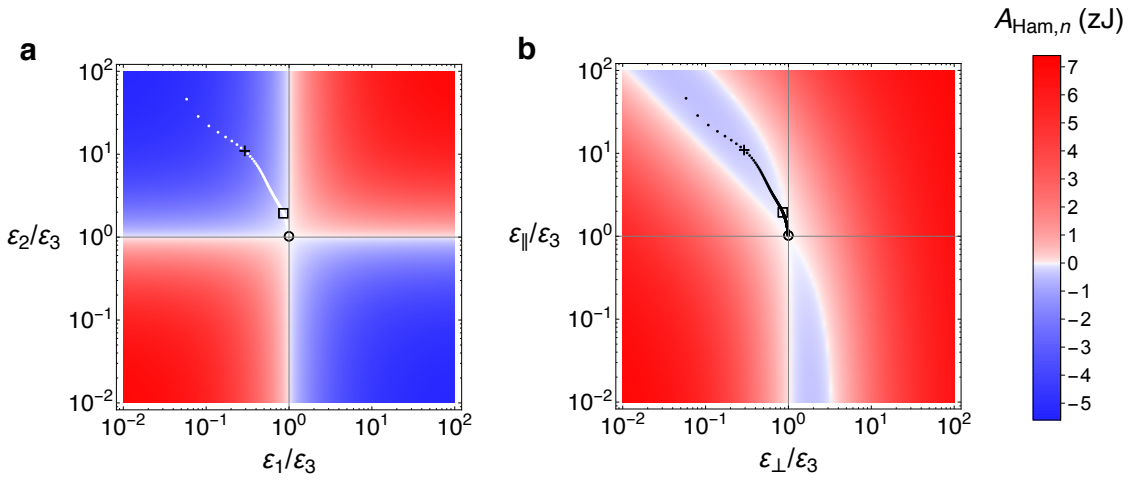

Figure 3.2: The contribution of a single Matsubara term to the total Hamaker coefficient is plotted as a function of the dielectric coefficients. The red regions represent a positive energy (attractive force) and the blue regions represent a negative energy (repulsive force). (a) shows the contributions when the interacting materials are isotropic and not necessarily identical. (b) shows the contributions for two anti-aligned identical birefringent materials. The blue regions correspond to a negative contribution to the free energy (repulsion) for both (a) and (b). For anti-aligned birefringent materials, the greatest negative contribution possible from a single Matsubara term is approximately -0.45 zJ. The points indicate the contributions from the first 1000 Matsubara terms for the gold/ethanol/vacuum system (or gold gratings interacting across ethanol in (b)) at room temperature (Matsubara terms $n = 10, 100, 1000$ are indicated by $+, \square, \bigcirc$, respectively).

materials: $\varepsilon_1 < \varepsilon_3 < \varepsilon_2$ or $\varepsilon_2 < \varepsilon_3 < \varepsilon_1$. These conditions correspond to the blue region in Fig. 3.2a.

By analogy, one might suspect that the repulsion condition for birefringent materials is $\varepsilon_\perp < \varepsilon_3 < \varepsilon_\parallel$ or, for materials with negative birefringence, $\varepsilon_\parallel < \varepsilon_3 < \varepsilon_\perp$. However, the repulsive condition depends on φ (the azimuthal direction of the mode's k-vector), and these inequalities are a necessary (but not sufficient) condition for repulsion. In the nonretarded case, the repulsion condition $r_1^{pp} r_2^{pp} < 0$, which yields a negative integrand in Eq. 3.5, simplifies to

$$\begin{aligned} &\left(\varepsilon_\perp \sqrt{1 + \left(\frac{\varepsilon_\parallel}{\varepsilon_\perp} - 1\right) \cos^2 \varphi} - \varepsilon_3\right) \times \\ &\left(\varepsilon_\perp \sqrt{1 + \left(\frac{\varepsilon_\parallel}{\varepsilon_\perp} - 1\right) \cos^2 (\theta + \varphi)} - \varepsilon_3\right) < 0. \end{aligned} \tag{3.6}$$

Systems that exhibit Casimir-Lifshitz repulsion (and, as a result, an attractive-repulsive transition with θ) will have materials that satisfy Eq. 3.6 for a range of φ at many Matsubara frequencies. In the anti-aligned case where $\theta = \pi/2$, this is achieved for combinations of dielectric functions that fall in the blue regions of Fig. 3.2b. As an example of such a system, we consider a fictional material with high birefringence that has $\varepsilon_\parallel$ modeled by the dielectric response of gold and $\varepsilon_\parallel = 1$. We use the dispersion models from [32] and [70] for ethanol and gold, respectively. The points in Fig. 3.2b correspond to the $A_{\mathrm{Ham},n}$ that contribute to the repulsive nonretarded Casimir-Lifshitz force for this system. For comparison, the points in Fig. 3.2a correspond to the nonretarded Casimir-Lifshitz interaction in a gold/ethanol/vacuum system.

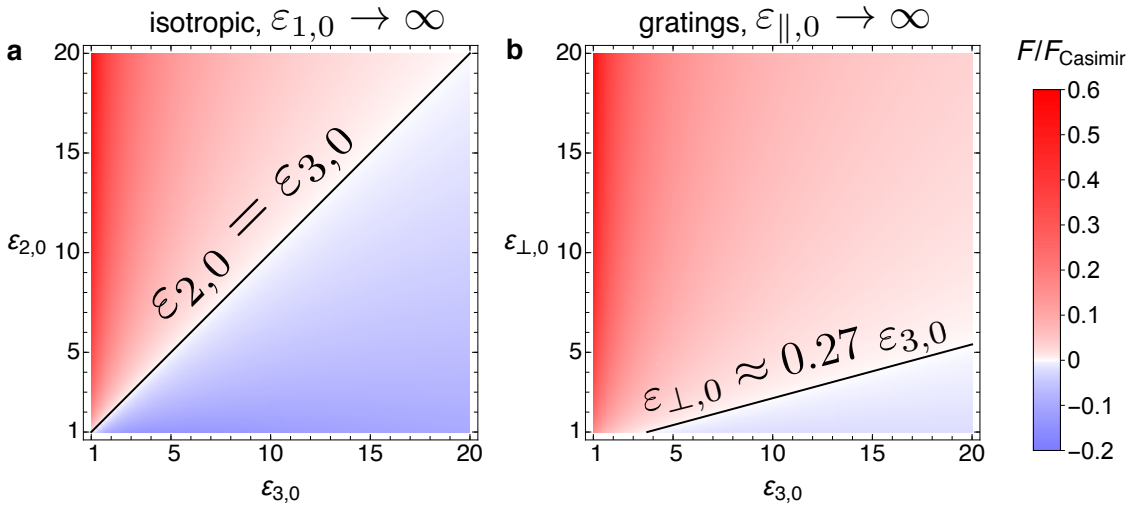

Figure 3.3: The ratio of the zero-temperature, long-range Casimir force for two systems scaled to the Casimir force between two perfect conductors, ($F_{\text{Casimir}} = -\hbar c\pi^2 240/d^4$), with $\varepsilon_{\parallel,0}$ and $\varepsilon_{1,0}$ taken to infinity (as for a perfect conductor). In this case, DC the dielectric constants of the other materials determine the sign of the force. For the isotropic case (a), the condition for repulsion is the usual $\varepsilon_{2,0} < \varepsilon_{3,0}$. For the case with identical, anti-aligned birefringent materials (b), the repulsive condition is numerically found to be $\varepsilon_{\perp,0} \lesssim 0.27\varepsilon_{3,0}$.

3.2.2 Long-range repulsive Casimir force between anisotropic materials

At separations greater than a few nanometers, retardation effects become significant. The Hamaker coefficient usually decreases monotonically with distance, although it may be slightly increased in special cases [27]. The Casimir-Lifshitz force is a result of quantum fluctuations as well as thermal fluctuations, and the quantum fluctuations alone can cause repulsion between anti-aligned, birefringent materials. To illustrate this, we consider the long-range, zero-temperature Casimir effect. In this regime, the force between metals approaches the original expression derived by Casimir [1]: $F_{\text{Casimir}}(d) = -\hbar c\ \frac{\pi^2}{240}\frac{1}{d^4}$. Lifshitz derived the force between

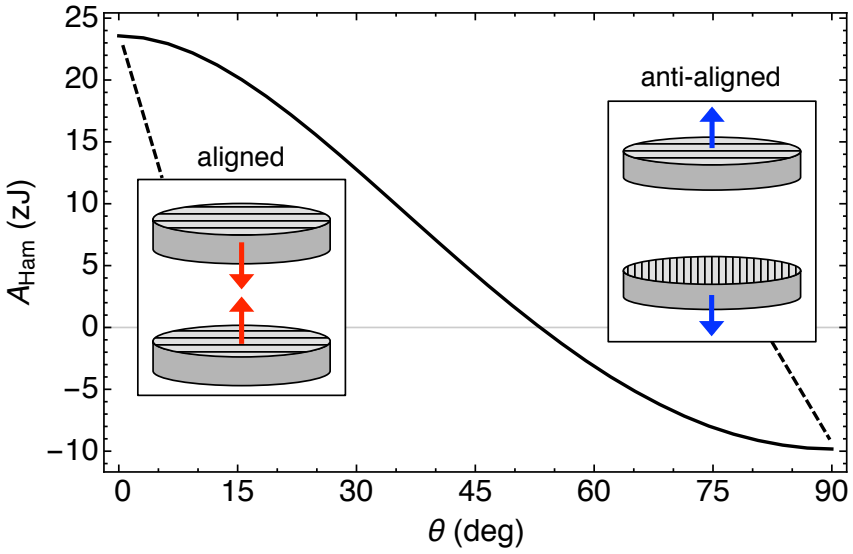

Figure 3.4: The room temperature, nonretarded Hamaker constant between infinite half-spaces of 1D conductors ($\varepsilon_\perp = 1$, $\varepsilon_\parallel = \varepsilon_{\mathrm{Au}}$) separated by ethanol. The slabs experience an attractive force when the conduction axes are aligned, and a repulsive force when the axes are anti-aligned.

dielectrics in the long-range case [6]. Physically, the DC dielectric constant $\varepsilon_{i,0}$ is used to describe the dielectric function over all frequencies because the high frequency terms are damped by retardation. With this approximation, we calculate the long-range Casimir force of anti-aligned gratings when the material is an ideal conductor ($\varepsilon \to \infty$) along its ordinary axes or extraordinary axis, which correspond to 2D and 1D conductors, respectively. When the material is a 1D conductor (Fig. 3.3), there is Casimir repulsion for anti-aligned materials when $\varepsilon_{\perp,0} \lesssim 0.27\varepsilon_{3,0}$. We note that long-range interactions at finite temperatures are dominated by the nonretarded $n = 0$ Matsubara term, which is strictly attractive for 1D conductors ($\varepsilon_\parallel \to \infty$). However, birefringent materials with finite dielectric functions at zero frequency may still exhibit long-range Casimir repulsion if the materials satisfy the conditions in Fig. 3.2b for the $n = 0$ term.

3.2.3 Example with gold, ethanol, and vacuum

To illustrate some of the consequences of an orientation-dependent sign change in the Casimir force, we further consider the interaction between 1D gold conductors across ethanol with retardation effects: $\varepsilon_{\parallel} = \varepsilon_{\mathrm{Au}}$, $\varepsilon_{\perp} = 1$, $\varepsilon_3 = \varepsilon_{\mathrm{ethanol}}$ at room temperature. The anisotropic materials can be thought of as idealized arrays of gold nanowires. As noted in [71], the dielectric models used in calculation can have a nontrivial effect on the calculated results, so these calculations do not precisely represent the physical system. Instead, we present them to demonstrate the sign change in the Casimir force as a function of separation and relative orientation, and emphasize that this effect can occur for other combinations of materials.

At short ranges, this system exhibits attraction for aligned materials and repulsion for anti-aligned materials. The Hamaker coefficient is plotted as a function of relative orientation in Fig. 3.4. The extreme values of A_{Ham} correspond to $\approx 6\ k_{\mathrm{B}}T$ at room temperature, which is a typical value for dielectrics interacting across a medium [3]. We also show the energy of the aligned and anti-aligned materials as a function of distance in Fig. 3.5, noting that the energy has the approximate form of $\Omega(d, \theta) \sim \sin^2\theta$ at a fixed distance. The anti-aligned plates exhibit Casimir repulsion up to a separation of 70 nm. At greater distances the Casimir force is attractive. This sign change is a result of the dispersion of the materials, as in [72].

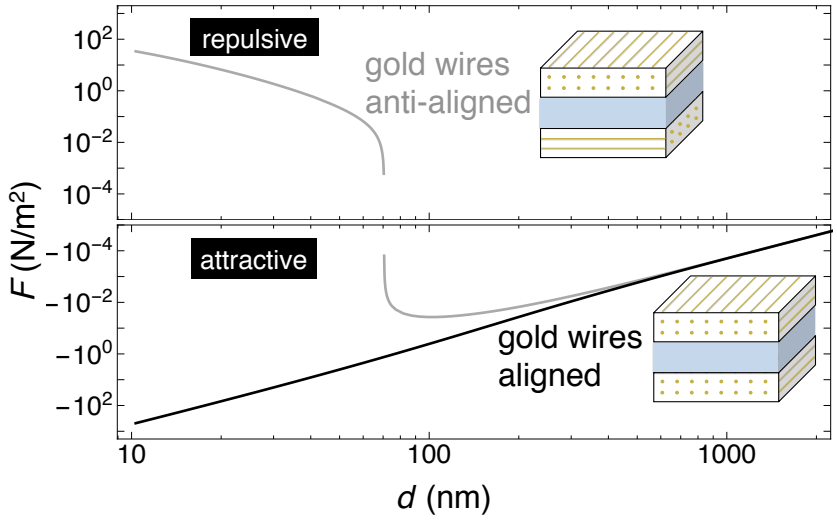

Figure 3.5: The distance dependence of the Casimir-Lifshitz force between two idealized 1D conductors separated by ethanol. When the conductance directions are perpendicular, the two plates are repelled at short distances ($d \lesssim 70$ nm) and attracted at long distances.

3.2.4 Casimir-Lifshitz repulsion between real materials

We have calculated the repulsive force between the hypothetical gold/vacuum gratings in ethanol to demonstrate a strong version of this effect. However, the gratings would surely have different dielectric properties than the simple $\varepsilon_\perp = 1$, $\varepsilon_\parallel = \varepsilon_{\mathrm{Au}}$ system we have described here. In reality, one might consider the effect between two identical, uniaxial crystals with high optical anisotropy. The calculation of Casimir-Lifshitz forces requires the knowledge of $\varepsilon(\mathrm{i}\xi)$ for a very large range of frequencies. These dielectric functions can be constructed from optical data with the Kramers-Kronig relations but usually carry a large degree of uncertainty [3, 73–75]. The repulsive force discussed here requires an intervening dielectric of intermediate strength at a large number of Matsubara terms so given the limited availability of experimentally determined optical properties, it is difficult to confidently predict a

combination of materials that could achieve repulsion.

However, we can suggest properties of materials that could achieve a repulsive force. With an eye towards satisfying Eq. 3.6, we suggest that the uniaxial crystals should have high birefringence. If the intervening material is a liquid, then uniaxial crystals with low indices may make the repulsion condition easier to satisfy (as many liquids have $1 < \varepsilon(\mathrm{i}\xi) < 2$ for the relevant Matsubara frequencies [75]). A system that satisfies Eq. 3.6 for the $n = 0$ Matsubara term, for which static dielectric constants are often well-known, would likely achieve repulsion at large separations where the $n = 0$ term dominates.

In Fig. 3.6, we plot dielectric models of $\varepsilon(\mathrm{i}\xi)$ for four birefringent materials along with $\varepsilon(\mathrm{i}\xi)$ models for liquids that satisfy Eq. 3.6 for some Matsubara terms. We construct Ninham-Parsegian models for $\varepsilon(\mathrm{i}\xi)$ of BaB_2O_4 and $LiIO_3$ using the method of [73], the static dielectric constants from [76], and the optical data from [77] and [78]. The model for $CaCO_3$ is from [74], and the models for iodobenzene and diiodomethane are from [75]. With these dielectric models, the systems with BaB_2O_4, $LiIO_3$, and $CaCO_3$ and chosen liquids would not experience Casimir-Lifshitz repulsion for any relative orientation of the crystals. However, given our limited knowledge of the $\varepsilon(\mathrm{i}\xi)$ functions, it is possible that the proposed systems or others like them could exhibit the repulsive effect described here for slightly modified optical properties.

A system that often satisfies Eq. 3.6 is the intervening 'melt' between two birefringent solids considered by Parsegian [11], which has $\varepsilon_3 = (2\varepsilon_\perp + \varepsilon_\parallel)/3$. This is a common model for liquid crystals in the isotropic state [79]. The lower right figure

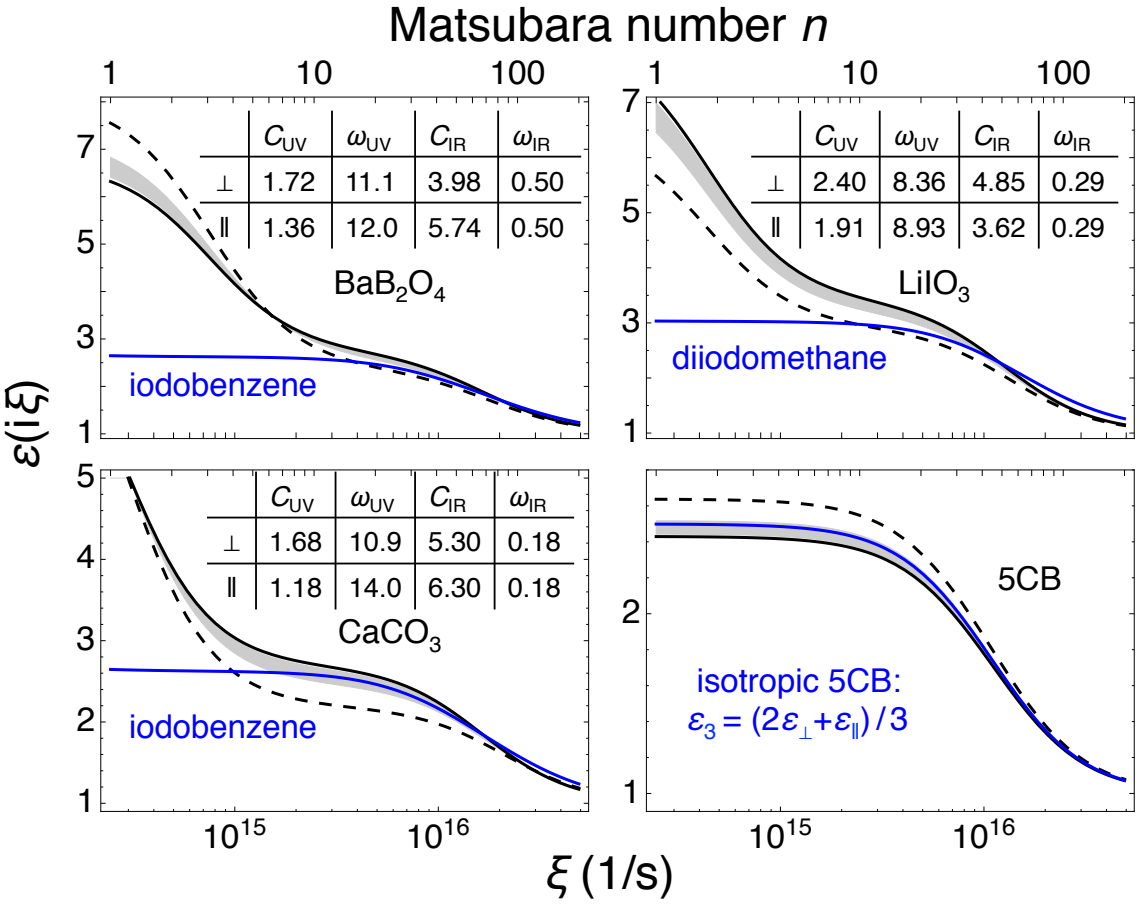

Figure 3.6: The black lines represent the birefringent crystals with solid and dashed lines corresponding to the ordinary ($\perp$) and extraordinary ($\parallel$) axes, respectively. The gray band represents values of $\varepsilon_3(i\xi)$ that satisfy Eq. 3.6. The blue lines represent a liquid chosen to maximize the number of Matsubara terms that satisfy Eq. 3.6. Inset are the values used in the Ninham-Parsegian oscillator model, with values for ω_{UV} and ω_{IR} in eV.

in Fig. 3.6 shows the interaction between anti-aligned 5CB nematic liquid crystal when separated by isotropic 5CB. This uses the dispersion model for 5CB developed in [80]. However, measuring a repulsive force between two liquid layers (separated by a third liquid at a different temperature) presents obvious experimental difficulties.

3.2.5 Summary of Casimir-Lifshitz repulsion between anisotropic materials

We have detailed the conditions for a repulsive Casimir-Lifshitz force to exist between identical birefringent materials in the retarded and nonretarded regimes. The constraint on the dielectric functions (Eq. 3.6) is more restrictive than the $\varepsilon_1 < \varepsilon_3 < \varepsilon_2$ condition for isotropic dielectrics. However, repulsion between identical birefringent materials is achievable. Furthermore, because the force can be changed from attractive to repulsive by rotating one of the materials, it could be used as a switchable force in MEMS or NEMS devices. Because repulsion between identical birefringent dielectrics exists for certain materials over a large range of separations, this effect could be important in many physical systems.

3.3 Casimir-Lifshitz torque enhancement by retardation and intervening dielectrics

The work in this section was originally published in [60]. At small separations, the Casimir-Lifshitz effect is equivalent to a van der Waals interaction. The connection between the Casimir-Lifshitz and van der Waals

formulations is summarized in a recent review by Woods [15]. The van der Waals free energy per unit area between two optically isotropic, planar dielectrics is often written in terms of a Hamaker constant A_0:

$$\Omega(d) = -\frac{A_0}{12\pi d^2}. \tag{3.7}$$

To account for the finite speed of light, the Hamaker constant becomes a distance-dependent Hamaker coefficient in the Casimir-Lifshitz formulation: $A_0 \to A(d)$. The Hamaker coefficient reduces to the Hamaker constant at short ranges [3, 81]. This distance dependence encodes the effect of retardation, or the finite speed of light. Retardation weakens Casimir-Lifshitz interactions between isotropic slabs, and $A(d)$ decays from A_0 to 0 as d increases. For two birefringent plates, the Hamaker coefficient depends on the relative angle between the plates, resulting in an angular dependence of the free energy per unit area:

$$\Omega(d, \theta) = -\frac{A(d, \theta)}{12\pi d^2}, \tag{3.8}$$

and hence a torque per unit area $M(d, \theta)$ arises between the two materials:

$$M(d, \theta) = -\frac{\partial \Omega(d, \theta)}{\partial \theta}. \tag{3.9}$$

In this section, we explore the effect of retardation on the Casimir-Lifshitz torque and find two surprising situations that lead to an enhancement of the torque. The geometry of the system is shown in the inset of Fig. 3.7, and the two effects in question are apparent in the plotted torques per unit area between parallel TiO_2 slabs at a separation of 30 nm. First, we demonstrate that the

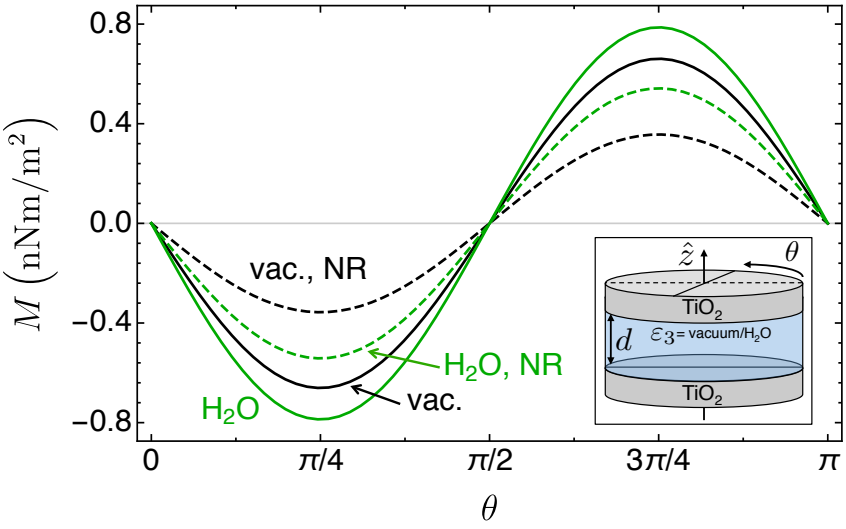

Figure 3.7: Casimir-Lifshitz torque per unit area between two TiO_2 slabs separated by 30 nanometers of vacuum (black) or water (green). In the nonretarded approximation (dashed), the Casimir-Lifshitz torque reduces to the van der Waals torque. The calculated torque is increased by the intervening dielectric as well as by retardation effects. Inset: geometry of the system in question.

anisotropic part of the Hamaker coefficient (corresponding to the Casimir-Lifshitz torque) between semi-infinite dielectric slabs is generally increased by retardation at small separations. For common birefringent crystals such as TiO_2, the enhancement is most prominent when the slabs are separated by tens of nanometers. As a result, the calculated torque is significantly greater when retardation effects are included than when they are neglected. Furthermore, we demonstrate that the insertion of a dielectric medium can increase the Casimir-Lifshitz torque at small separations. We demonstrate that common dielectric materials (such as liquids with optical refractive indices near 1.5), can increase the calculated Casimir-Lifshitz torque between TiO_2 slabs by as much as a factor of two. This effect persists throughout the experimentally accessible regime of separations on the order of 1–100 nm.

Heuristically, we can describe this effect by noting that the Casimir-Lifshitz torque depends on the relative orientation of the two plates. Even if the strength of the Casimir-Lifshitz interaction $\Omega(d, \theta)$ is decreased for all θ by inserting a dielectric medium, it may be decreased more for $\theta = \pi/2$ than for $\theta = 0$. As a result, the energy difference between the two orientations is increased, which corresponds to an enhancement of the torque.

As a result of these two effects, the calculated Casimir-Lifshitz torque can be greatly increased when retardation effects and intervening dielectric media are included. The enhancement of the torque by retardation implies that calculations that neglect retardation should be reexamined, as they may significantly underestimate the torque. A similar retardation effect was predicted for the Casimir-Lifshitz force in special cases involving systems with thin metallic films [82] or high anisotropy [27, 28]. The enhancement of the torque by insertion of a dielectric implies that an intermediate dielectric may be helpful in experiments designed to measure the Casimir-Lifshitz torque. To our knowledge, there is no analogous effect for the Casimir-Lifshitz force. Together, these results open new venues for manipulation of fluctuation forces at the nanoscale and have major implications for the design of Casimir-Lifshitz torque experiments.

3.3.1 Small anisotropy approximation

We consider a system of two parallel, semi-infinite, half-spaces of birefringent materials separated by distance d, as shown in the inset of Fig. 3.7. The materials

have their optic axes in the xy plane but are rotated by angle θ relative to each other. The Hamaker coefficient $A(d,\theta)$, can be split into isotropic and anisotropic parts $A^{(0)}(d)$ and $A^{(2)}(d)$, respectively:

$$A(d,\theta) \approx A^{(0)}(d) + A^{(2)}(d)\cos(2\theta)\,. \tag{3.10}$$

The cosine-like dependence in Eq. 3.10 is valid for materials with small birefringence. We define the isotropic and anisotropic parts of the Hamaker coefficient as in [28]: $A^{(0)}(d) = A(d,\pi/4)$, $A^{(2)}(d) = A(d,\pi/2) - A(d,0)$. The Casimir-Lifshitz torque is then approximated by:

$$M(d,\theta) \approx -\frac{A^{(2)}(d)\sin(2\theta)}{6\pi d^2}. \tag{3.11}$$

The effects of retardation on the Casimir-Lifshitz torque are encoded in $A^{(2)}(d)$.

With substitution of the dimensionless $\chi = rd$ in Eq. 2.2, the retarded Hamaker coefficient can be written as a sum of contributions at the Matsubara frequencies:

$$A(d,\theta) = {\sum_{n=0}^{\infty}}' A_n(d,\theta) \tag{3.12a}$$

$$A_n(d,\theta) = -\frac{3k_{\mathrm{B}}T}{\pi}\int_0^{\infty}\chi\mathrm{d}\chi\int_0^{2\pi}\mathrm{d}\varphi\ln D_n(\chi,\varphi)\,. \tag{3.12b}$$

To examine the effects of retardation, we consider the dependence of a single Matsubara term $A_n(d,\theta)$ on the dimensionless $r_n = 2\sqrt{\varepsilon_3}\xi_n d/c$. Physically, r_n is the ratio of round-trip travel time for light between the plates ($2\sqrt{\varepsilon_3}d/c$) to the characteristic decay time of the Matsubara frequency ($1/\xi_n$) [3]. Therefore, r_n is a measure of retardance: as $d/c \to 0$, $r_n \to 0$. The contribution from a Matsubara

term depends only on r_n and the dielectric properties at the corresponding imaginary frequency ξ_n. Each Matsubara term is split into isotropic and anisotropic terms as above: $A_n^{(0)}(r_n) = A_n(r_n, 0)$, $A_n^{(2)}(r_n) = A_n(r_n, \pi/2) - A_n(r_n, 0)$. By isolating $A_n^{(2)}(r_n)$, we can examine the effect of retardation on individual Matsubara terms that contribute to the Casimir-Lifshitz torque.

Following the notation of [27, 28], we define the anisotropy of the ith material as:

$$\delta_{i\perp} = \frac{\varepsilon_{i\perp} - \varepsilon_3}{\varepsilon_3}, \quad \delta_{i\parallel} = \frac{\varepsilon_{i\parallel} - \varepsilon_3}{\varepsilon_3}, \tag{3.13}$$

where ε is the real part of the dielectric function evaluated at imaginary frequency iξ. As in [28], we expand the integrand of Eq. 3.12b for small $\delta_{i\perp}$ and $\delta_{i\parallel}$ to second order (there is no zeroth or first order contribution). The integral over wavevectors is carried out analytically with the use of the exponential integral $\mathrm{Ei}(x) = -\int_{-x}^{\infty} \frac{e^{-t}}{t} \mathrm{d}t$:

$$A_n(r_n, \theta) = A_n^{(0)}(r_n) + A_n^{(2)}(r_n) \cos(2\theta) + ... \tag{3.14a}$$

$$A_n^{(2)}(r_n) = \frac{3k_\mathrm{B}T}{256} \left(\delta_{1\parallel} - \delta_{1\perp}\right) \left(\delta_{2\parallel} - \delta_{2\perp}\right) \zeta(r_n) \tag{3.14b}$$

$$\zeta(r_n) = \frac{1}{2}\Big[e^{-r_n} \left(-r_n^3 + r_n^2 + 2r_n + 2\right) - \mathrm{Ei}(-r_n) \left(r_n^4 + 4r_n^2\right) \Big]. \tag{3.15}$$

To second order in $\delta_{i\perp}$ and $\delta_{i\parallel}$, the $\cos(2\theta)$ dependence is exact. The $A_n^{(0)}(r_n)$ term is independent of θ and does not contribute to the torque. In the nonretarded

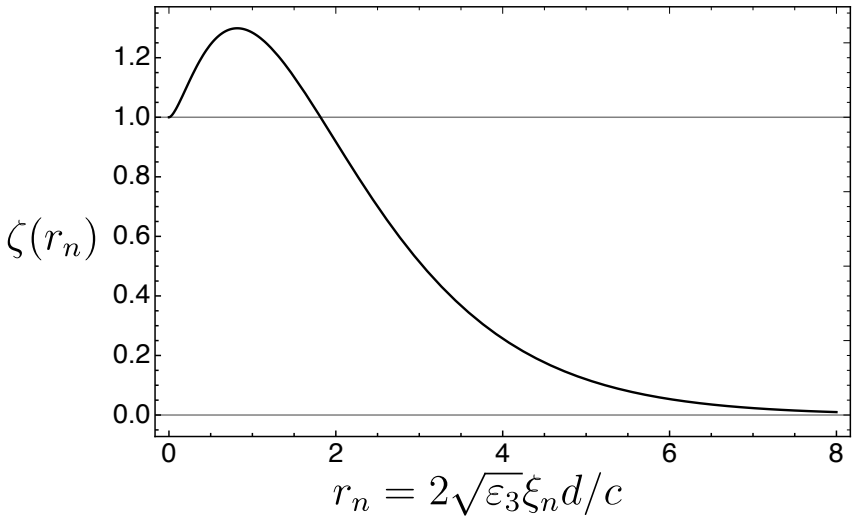

Figure 3.8: For small birefringence, contributions of Matsubara terms to the anisotropic part of the Hamaker coefficient (and therefore the Casimir-Lifshitz torque), which is proportional to $\zeta(r_n)$, are increased by retardation at small separations.

limit, $\zeta(r_n \to 0) = 1$, Eq. 3.14b reduces to:

$$A^{(2)}_{n,\mathrm{NR}} = \frac{3k_\mathrm{B}T}{256}\left(\delta_{1\parallel} - \delta_{1\perp}\right)\left(\delta_{2\parallel} - \delta_{2\perp}\right). \tag{3.16}$$

Now we examine the dependence of $A^{(2)}_n(r_n)$ on r_n, which is wholly contained within $\zeta(r_n)$ (Eq. 3.15). This function is plotted in Fig. 3.8. The nonmonotonicity of $\zeta(r_n)$ is surprising—it implies that for small values of r_n, the contribution of a single Matsubara term to the Casimir-Lifshitz torque is increased by retardation. We can make an even stronger claim: for small d, the total Casimir-Lifshitz torque is also increased by retardation. This behavior is because for real materials, a finite number of Matsubara terms contribute to Casimir-Lifshitz interactions (all materials become optically transparent as $\xi \to \infty$). As the distance between two materials approaches 0, the set of r_n's corresponding to this finite set of Matsubara terms will fall in the retardation-enhancement region where $r_n \lesssim 1.82$ and $\zeta(r_n) > 1$. This means that

the sum of Matsubara terms will also be enhanced by retardation in this limit. Therefore, for small separations and small birefringence, retardation will generally cause an increase in the Casimir-Lifshitz torque.

3.3.2 Numerical demonstration of retardation enhancement

This calculation is to second order in $\delta_{i,\perp}$ and $\delta_{i,\parallel}$, but for materials with higher anisotropy (such as those chosen to maximize the Casimir-Lifshitz torque) the approximation is less accurate. However, this nonmonotonicity persists in the analytic expansion to third order in $\delta_{i\perp}$ and $\delta_{i\parallel}$ as well. Furthermore, numerical exploration of the parameter space shows that all combinations of dielectric constants produce a nonmonotonic dependence on r_n of the anisotropic part of the Hamaker coefficient. To demonstrate the generality of this effect, we calculate the anisotropic part of the Casimir-Lifshitz interaction for two $BaTiO_3$ slabs (strong birefringence), two TiO_2 slabs, and one $BaTiO_3$ and one TiO_2 slab in Fig. 3.9. The material dispersions in this paper are modeled using the parameters from [74] and [75]. The anisotropic part of the Hamaker coefficient $A_n^{(2)}(d)$ is plotted for these material combinations in Fig. 3.9a. The nonmonotonicity of $A_n^{(2)}(d)$ and the increase due to the inclusion of water is clear. The effect of retardation is even clearer in Fig. 3.9b, which plots the ratio of the full calculation to the nonretarded approximation: the full calculation yields a torque several times stronger than the nonretarded calculation (by nearly a factor of 12). When the plates are separated by $\approx$ 30 nm, the calculated torque is typically $\gtrsim$ 50% stronger when retardation

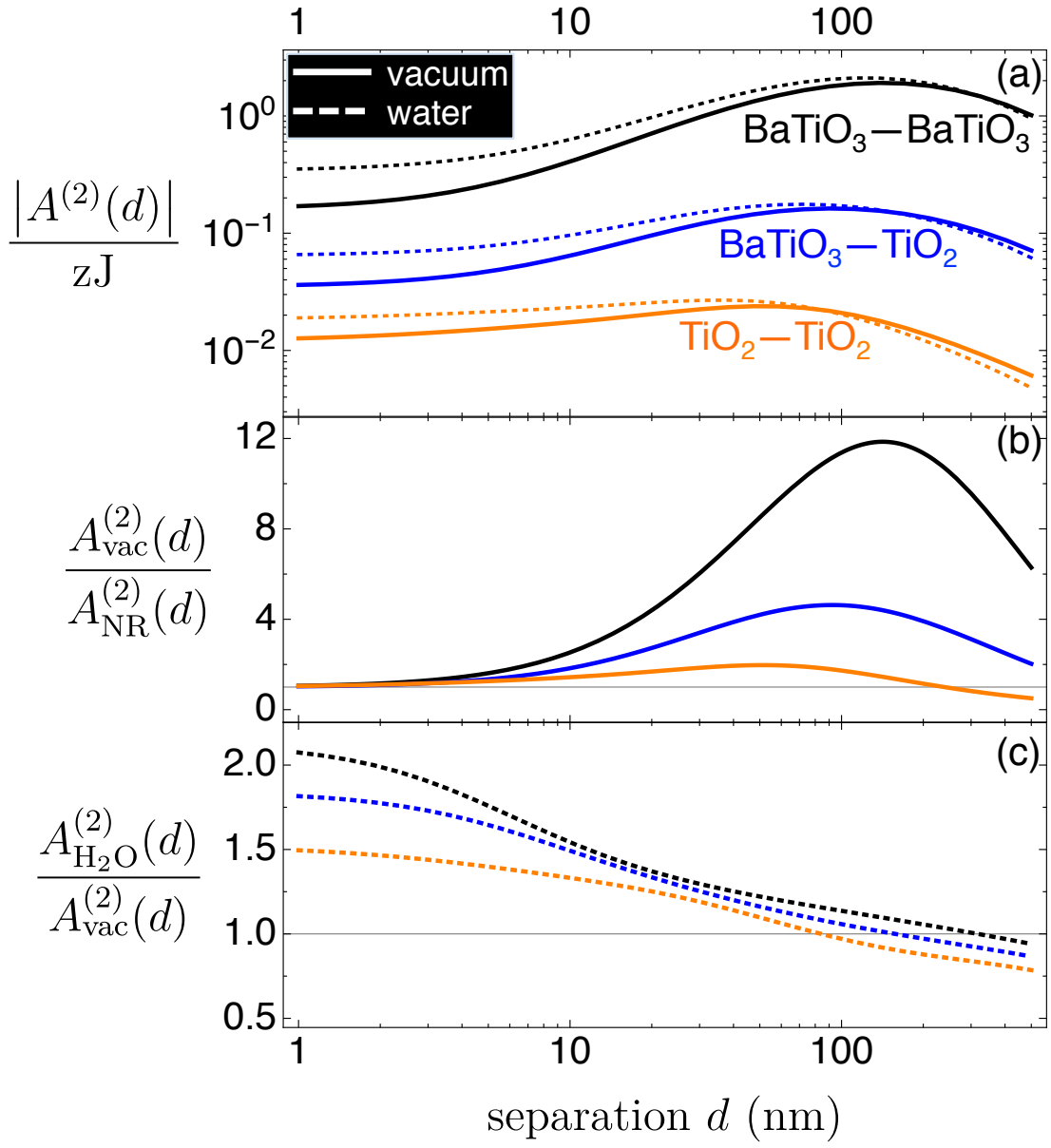

Figure 3.9: The effects of retardation and insertion of a water layer on the anisotropic part of the Casimir-Lifshitz energy. (a) Anisotropic part of the Hamaker coefficient for three material combinations ($BaTiO_3$–$BaTiO_3$, $BaTiO_3$–TiO_2, and TiO_2–TiO_2 in black, blue, and orange) when the materials are separated by vacuum (solid) and water (dashed). (b) Ratio of the anisotropic part of Hamaker coefficients with retardation effects to the nonretarded approximation. (c) Ratio of the anisotropic part of Hamaker coefficients for materials separated by water to those separated by vacuum. For $d \lesssim 90$ nm, the torque is enhanced by retardation and by the intervening water for all three material combinations.

effects are included. However, the magnitude of the enhancement is highly dependent on the choice of birefringent material.

3.3.3 Torque enhancement by dielectric media

Retardation effects are always an experimental reality, so the difference between the nonretarded and full calculations cannot be measured. However, one could choose to include an intervening dielectric medium between two birefringent materials. This addition modifies the dispersion relation $D_n(r, \varphi)$, which can significantly increase the Casimir-Lifshitz torque. Figures 3.9a and 3.9c show the effect of filling the vacuum gap with water, which causes a significant increase in the torque over a broad range of separations.

We examine the effect of the intervening dielectric in more detail by comparing $A^{(2)}(d)$ for two TiO_2 slabs separated by vacuum and several distinct fluids in Fig. 3.10. The inclusion of dielectrics with higher refractive indices at optical frequencies (which dominate short-range Casimir-Lifshitz interactions) results in higher Casimir-Lifshitz torques at small separations. In fact, torques are enhanced for most experimentally accessible separations ($\approx$ 75 nm for these materials—beyond this separation, the torques are extremely weak). For $d \lesssim 100$ nm, the torque is also enhanced by retardation effects. Beyond this point, retardation effects weaken the torque (affecting the systems with dielectric media the most). At very large separations at room temperature, only the $n = 0$ Matsubara term contributes—this term is dominated by thermal fluctuations and

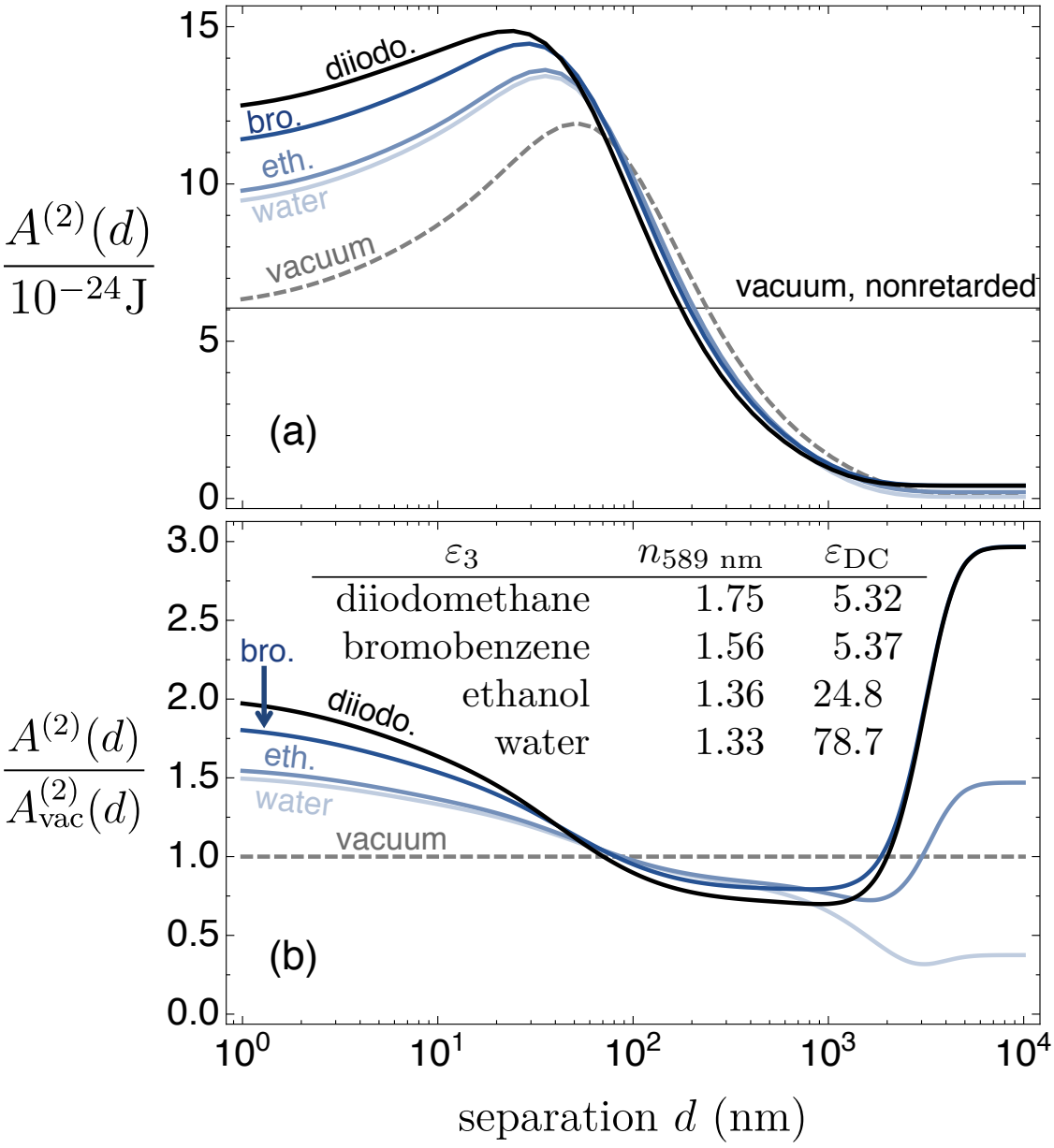

Figure 3.10: (a) The combined effects of retardation and an intervening dielectric media on anisotropy of Casimir-Lifshitz free energy between two parallel slabs of TiO_2. The anisotropic part of the Hamaker coefficient is increased by these two effects for $d \lesssim 100$ nm. (b) The effect of the intervening dielectric media are isolated by scaling $A^{(2)}(d)$ to the value when the plates are separated by vacuum. At small separations ($d < 50$ nm), the liquids with higher optical refractive indices cause the greatest increase in the torque. At very large separations ($d > 50$ μm), the $n = 0$ Matsubara term dominates, so only the DC dielectric constant is relevant.

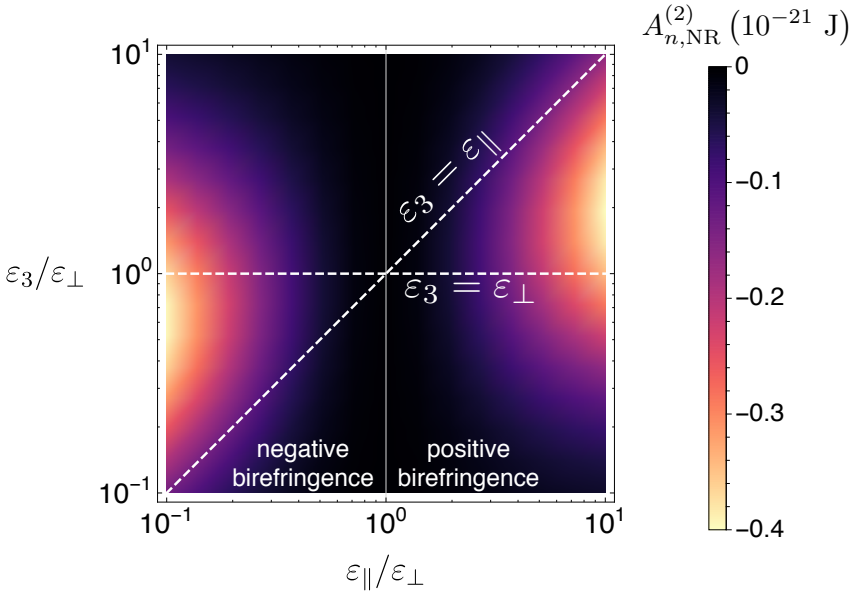

Figure 3.11: Each Matsubara term contributes $A^{(2)}_{n,\mathrm{NR}}$ to the anisotropy of the Casimir-Lifshitz interaction. For two identical birefringent slabs, the ε_3 that maximizes $A^{(2)}_{n,\mathrm{NR}}$ (and therefore the Casimir-Lifshitz torque) is between $\varepsilon_\perp$ and $\varepsilon_\parallel$.

is not affected by retardation [3, 81]. Therefore, the same torque enhancement seen at short ranges reappears for three of the materials for $d > 2$ μm. The DC dielectric constant for water and ethanol, however, are so high that the long-range torque is reduced instead of enhanced. We note that the Casimir-Lifshitz torque at separations $>$ µm may be too small to measure in currently proposed experiments when a dielectric medium is introduced. At a separation of $d = 30$ nm, the maximum nonretarded torque between the plates across vacuum is 3.6×10^{-10} Nm/m^2. This is increased by a factor of 1.9 when retardation effects are included, and by a factor of 2.2 when retardation effects and an intervening diiodomethane medium are included. Although intervening media can cause other experimental difficulties, a large increase in the torque may represent a worthwhile trade-off.

In Fig. 3.11, we calculate how the nonretarded torque is affected, more

generally, by a dielectric medium. The torque is increased by inserting a medium with a dielectric function somewhere between $\varepsilon_\perp$ and $\varepsilon_\parallel$ of the birefringent material. For a given choice of $\varepsilon_\perp$ and $\varepsilon_\parallel$, $\varepsilon_3 = 1$ does not typically maximize the torque. For example, with $\varepsilon_\perp = 5.81$ and $\varepsilon_\parallel = 6.62$ (as for the DC dielectric terms of TiO_2 in Bergström's model [74]), the optimal ε_3 is about 6. In this case, the contribution to the Casimir-Lifshitz torque is nearly tripled by the insertion of such a dielectric (compared to vacuum).

The distance dependence of Casimir-Lifshitz interactions is further complicated by retardation screening of high frequency contributions at larger separations. The interplay of dielectric functions can lead to a rich variety of unusual effects, as demonstrated in Refs. [72, 83]. However, we emphasize that the effects we demonstrate here are distinct from those that rely on particular combinations of dielectric materials. The torque enhancement by retardation is independent of dielectric functions, and the enhancement by the inclusion of a dielectric medium is quite general and appears even in the nonretarded calculation.

In this section we have shown that, at short distances, the Casimir-Lifshitz torque between parallel slabs is increased by retardation. The nonretarded approximation can underestimate the torque by as much as an order of magnitude. This is the case even at separations on the order of 10 nm, a regime in which retardation effects are often ignored. Furthermore, an intervening dielectric medium often increases the Casimir-Lifshitz torque by a significant amount. A carefully selected dielectric liquid can make the torque stronger and more experimentally accessible. We encourage researchers to include the effects of

retardation and an intervening medium, as they may make measurements realizable in surprising conditions.

Chapter 4: Nematic liquid crystals

4.1 Overview

In this section, we provide a brief overview of the physics of liquid crystals, which act as both the measurement probe and as one of the birefringent materials in our experiment. There are many useful primers on the subject of liquid crystals [84, 85], but here we briefly outline their properties relevant to the present work.

For some materials, there exists a liquid crystal phase at a temperature between the solid and liquid phases. It is characterized by long-range molecular ordering, even as the individual molecules jitter. Though there are several types of liquid crystals, we restrict our focus to nematic liquid crystals, the molecules of which exhibit orientational but not positional ordering (Fig. 4.1).

4.2 Oseen-Frank theory

Liquid crystals molecules tend to align with their neighbors, and there is an elastic free energy penalty associated with spatial variations of the director (the locally-preferred molecular orientation). The phenomenological Oseen-Frank theory provides a convenient formulation to describe this free energy [86, 87]. In

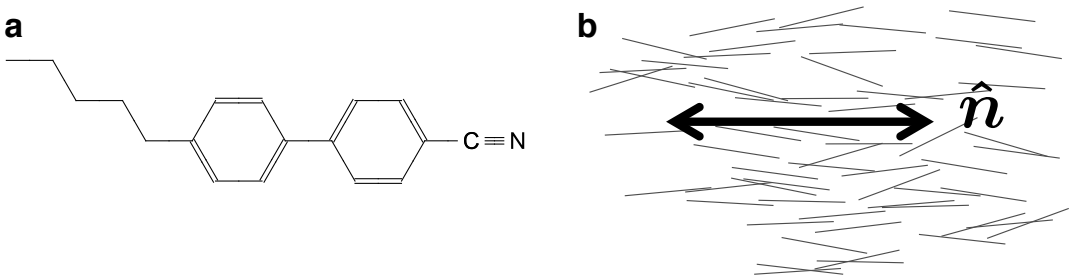

Figure 4.1: a) 5CB molecule. The extraordinary axis is along the long axis of the molecule. b) The 5CB molecules are depicted as lines. In the nematic state, the liquid has average molecular orientation along the director $\hat{\boldsymbol{n}}$. Optically, the liquid crystal can behave as a solid birefringent crystal with extraordinary axis parallel to the director.

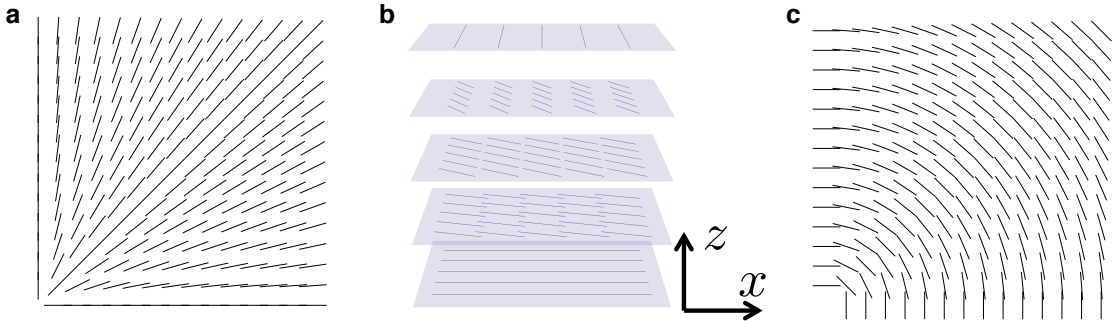

Figure 4.2: The three elastic modes in the Oseen-Frank free energy. a) Bend mode b) Twist mode c) Splay mode.

this formulation, the free energy density associated with elastic distortions is split into "bend," "twist," and "splay" modes with corresponding elastic constants k_{11}, k_{22}, and k_{33} (Fig. 4.2):

$$F_{\mathrm{OF}} = \frac{k_{11}}{2}\left|\nabla\cdot\boldsymbol{n}\right|^2 + \frac{k_{22}}{2}\left|\boldsymbol{n}\cdot(\nabla\times\boldsymbol{n})\right|^2 + \frac{k_{33}}{2}\left|\boldsymbol{n}\times(\nabla\times\boldsymbol{n})\right|^2. \tag{4.1}$$

In the twisted-nematic geometry (depicted in Fig. 4.2b), the director can be written as $\hat{\boldsymbol{n}} = (\cos(\theta(z)), \sin(\theta(z)), 0)$, where $\theta(z)$ is the azimuthal angle from x-axis. In this configuration, only the twist mode is present. This yields a Frank-Oseen free

energy density reminiscent of a simple harmonic oscillator:

$$F_{\mathrm{TN}} = \frac{k_{22}}{2}\theta'(z)^2. \tag{4.2}$$

We use the twisted nematic geometry for Chapters 5–7.

4.3 Twisted nematic liquid crystal displays

In a typical application, a liquid crystal layer of a few µm is sandwiched between transparent electrodes. The substrates are also treated in a way to cause uniform alignment of the liquid crystal in a chosen direction in the plane of the substrates. This alignment can be achieved by many means, including a rubbed polymer layer, oblique deposition of columnar structures, or photoalignment (in which a polymer layer is cured with polarized UV light) [88]. In the twisted-nematic display, these substrates are rotated 90° from each other. Using calculus of variations, it can be shown that the liquid crystal orientation with minimal free energy is a linear twist through the thickness of the cell:

$$\hat{\boldsymbol{n}} = (\cos(\theta(z)), \sin(\theta(z)), 0) \tag{4.3}$$

$$\theta(z) = \theta_i + (\theta_f - \theta_i)z/t \tag{4.4}$$

where t is the thickness of the cell, θ_i is the anchoring angle at $z = 0$, and θ_f is the anchoring angle at $z = t$. This results in a twisted birefringent material; in the following section we show how this can rotate the polarization direction of linearly polarized light from θ_i to θ_f.

By applying a voltage difference across the electrodes, the liquid crystal

director is aligned in the z-direction, resulting in a material that appears isotropic when viewed along z. Modern display technologies use many refinements of this method to increase contrast, viewing angle, and switching rate, but the basic principles are largely the same [89].

4.4 Van der Waals alignment of liquid crystals

Short-range anisotropic van der Waals interactions have long been suspected to cause liquid crystal alignment [90]. Okano *et al.* calculated the effect of short-range van der Waals interactions between a liquid crystal and substrate, using the molecular size of a liquid crystal molecule as the separation distance [91]. Blinov and Sonin carried out a clever experiment with liquid crystal droplets on mica surfaces covered with stearic acid monolayers, that showed that there was some effective range (10–50 nm) of these interactions [92]. Schadt *et al.* were the first to show that van der Waals interactions alone were sufficient to align liquid crystals [102]. Gwag *et al.* suggested that the mechanism of liquid crystal alignment caused by a rubbed polyimide is a nonretarded van der Waals interaction [93]. Nishikawa *et al.* compared the dichroism and alignment strength of polyimide layers cured with linearly-polarized UV light [94]. Hwang *et al.* demonstrated that the in-plane or out-of-plane alignment of liquid crystals on inorganic substrates depends on the sign of the liquid crystal birefringence, consistent with a van der Waals interaction [95]. In a review article, Ishihara includes van der Waals torques as a mechanism for liquid crystal alignment [88]. As a whole, these works demonstrate that the alignment

of liquid crystals is influenced by the anisotropic van der Waals/Casimir torque. However, none of them quantitatively measure the distance or angular dependence of the torque, and none of them consider the effects of retardation.

4.5 Jones analysis of twisted liquid crystals

In this section, we describe the effect of twisted liquid crystals on the polarization of transmitted light using Jones calculus [96]. Consider transverse light propagating through a planar material in the z-direction. A birefringent crystal of thickness t and refractive indices n_x and n_y imparts phase ϕ_x and ϕ_y to E_x and E_y, respectively, and has the Jones matrix:

$$M_{\text{brf}} = \begin{pmatrix} e^{i\phi_x} & 0 \\ 0 & e^{i\phi_y} \end{pmatrix} = e^{i\frac{(\phi_x+\phi_y)}{2}} \begin{pmatrix} e^{-\frac{i\Delta\phi}{2}} & 0 \\ 0 & e^{\frac{i\Delta\phi}{2}} \end{pmatrix} \tag{4.5}$$

$$\Delta\phi = \phi_y - \phi_x = \frac{2\pi(n_y - n_x)t}{\lambda} = \frac{2\pi\Delta n t}{\lambda} \tag{4.6a}$$

$$\Delta n = n_y - n_x \tag{4.6b}$$

where λ is the wavelength of the light. The overall phase $e^{i\frac{(\phi_x+\phi_y)}{2}}$ is irrelevant in our analysis, and will be ignored whenever convenient.

A twisted nematic has a rotation angle that varies linearly across the cell from θ_i to θ_f, according to Oseen-Frank theory. It has the Jones matrix [97].

$$M_{\text{LC}} = R_{\theta_f} \begin{pmatrix} \cos X - \frac{i\Delta\phi}{2}\operatorname{sinc} X & \Delta\theta \operatorname{sinc} X \\ -\Delta\theta \operatorname{sinc} X & \cos X + \frac{i\Delta\phi}{2}\operatorname{sinc} X \end{pmatrix} R_{-\theta_i} \tag{4.7a}$$

$$X = \sqrt{\Delta\theta^2 + \Delta\phi^2/4} \tag{4.7b}$$

$$\Delta\theta = \theta_f - \theta_i \tag{4.7c}$$

For thick liquid crystal layers, $\Delta\phi \gg \Delta\theta$ and, to leading order, the the liquid crystal matrix reduces to

$$M_{\mathrm{LC},0} = R_{\theta_f} \begin{pmatrix} e^{-\frac{i\Delta\phi}{2}} & 0 \\ 0 & e^{\frac{i\Delta\phi}{2}} \end{pmatrix} R_{-\theta_i}. \tag{4.8}$$

This approximation is well-justified for our experiment; typical values for the twisted nematic layer are $\Delta n = 0.2$, $t = 50\,\mu\mathrm{m}$, $\lambda = 0.5\,\mu\mathrm{m}$, and $\Delta\theta = \pi/4$, which yield $\Delta\theta/\Delta\phi = 1/80$. This formulation clarifies the roles of the liquid crystal layer in display technologies. The effect of a thick, twisted liquid crystal on light incident with polarization angle θ_i (matching the alignment of the liquid crystal upon entry) is:

$$M_{\mathrm{LC},0} R_{\theta_i} \begin{pmatrix} 1 \\ 0 \end{pmatrix} = R_{\theta_f} \begin{pmatrix} e^{-\frac{i\Delta\phi}{2}} & 0 \\ 0 & e^{\frac{i\Delta\phi}{2}} \end{pmatrix} R_{-\theta_i} R_{\theta_i} \begin{pmatrix} 1 \\ 0 \end{pmatrix} \tag{4.9a}$$

$$= R_{\theta_f} \begin{pmatrix} e^{-\frac{i\Delta\phi}{2}} \\ 0 \end{pmatrix}, \tag{4.9b}$$

which is linearly polarized along θ_f (modulo some overall phase). The polarization of linearly polarized light follows the liquid crystal twist. In the twisted-nematic display, this is used to pass polarized light through a second polarizer rotated to 90°. When a voltage is applied across the electrodes, the liquid crystal director is aligned in the propagation direction of light and the layer appears isotropic, having no effect on the polarization state. In the on state, the second polarizer blocks the

transmission of light.

Chapter 5: An experimental proposal for measuring Casimir-Lifshitz torques

5.1 Introduction

We published the experimental design for a Casimir torque measurement in 2015 [37]. Since then, we changed and updated several aspects of the experiment. They are detailed in Section 5.8. We include the original proposal here for completeness.

5.2 Overview of experimental design

Experiments that use a torsion pendulum can measure torques with very high sensitivity [98], so they seem a natural choice for measuring a Casimir torque. Munday *et al.* considered a measurement of the Casimir torque between a $BaTiO_3$ plate and $CaCO_3$ using a torsion pendulum, but concluded that it would be technically difficult to hold large plates (1 cm in diameter) in parallel at submicron distances [32]. Chen and Spence considered a similar experiment, which replaced one of the plates with a curved surface [34]. The Casimir torque would affect the period of natural oscillations of the torsion pendulum, allowing for its detection.

They considered carefully several sources of noise and error and concluded that a measurement with a torsion pendulum was feasible; however, they have not published any experimental results to date.

Here we propose a method that is in analogy to a static torsion pendulum with a thick liquid crystal layer as the twisted bulk. As the uniformly aligned liquid crystal is brought near a birefringent crystal, the Casimir torque aligns the liquid crystal molecules with the solid crystal's optic axis, which in turn causes a twist through the bulk of the liquid crystal. A similar experiment was proposed by Smith and Ninham in 1973 [38] but, to our knowledge, was never carried out. Here we provide a calculation of the expected results for a similar geometry including retardation effects, as well as detailed experimental considerations.

Instead of using the liquid crystal in the isotropic phase as a spacer layer (which is experimentally unfeasible), a thin layer of SiO_2 separates the liquid crystal from the solid crystal. Varying the SiO_2 thickness is equivalent to changing the distance between parallel plates. If both the liquid crystal and birefringent crystal have positive uniaxial anisotropy, then the Casimir torque causes the liquid crystal molecules to twist towards the extraordinary axis of the solid crystal. Because the liquid crystal is anchored at the glass interface, the director is twisted through the bulk by the Casimir torque at the boundary at the opposite interface. This geometry is depicted in Fig. 5.1. This experimental design is similar to methods for measuring the azimuthal anchoring energy of liquid crystals on treated substrates [99].

The mechanism of liquid crystal alignment induced by a rubbed polymer layer itself is the subject of much study but is thought to include physical grooves, aligned

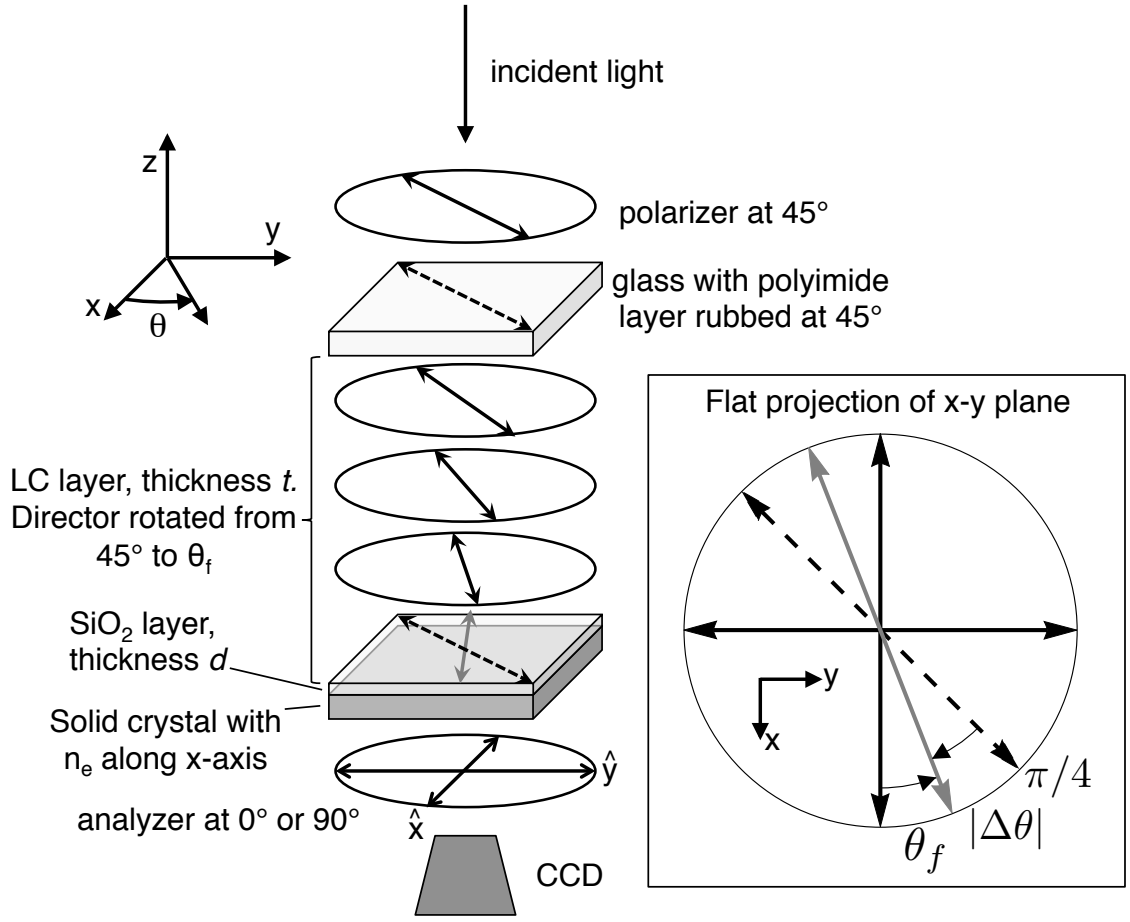

Figure 5.1: Experimental setup. The liquid crystal director is fixed at 45° at the top surface, but a Casimir torque at the bottom surface causes a linear twist throughout the bulk (thickness $t = 50\,\mu\text{m}$). Incident light polarized at 45° is adiabatically twisted with the liquid crystal director to a final polarization state θ_f which can be measured optically. Stronger Casimir torques cause a greater director twist. The inset shows a flat projection of the x-y plane.

polymer chains, and the van der Waals torque for surfaces in contact [88,94,100,101]. The last of these is equivalent to the short-ranged Casimir torque of our proposed study, though distinguishing the van der Waals effect from other alignment effects is difficult. However, previous experiments have suggested the anisotropic van der Waals effect as the mechanism of liquid crystal alignment at a surface.

Schadt *et al.* used linearly photopolymerized layers to align liquid crystals with a van der Waals interaction [102]. Lu *et al.* also provided evidence that the van der Waals interaction is an important component of the liquid crystal alignment at treated polymer layers [103]. However, these experiments do not isolate the van der Waals torque from other surface effects, because the liquid crystal is in contact with the substrate. Our proposed experiment would demonstrate this effect over a distance of tens of nanometers (and in doing so measure the long-range retardation effects of the Casimir torque). Finally, we can relate measured data to Casimir torques calculated from the dispersive properties of the materials.

Smith and Ninham considered the non-retarded case of this system and predicted measurable distortions of the liquid crystal director. Here we carry out the full retarded calculation of the Casimir torque, by considering its effect on a thin boundary layer. That is, in comparison to the liquid crystal bulk with thickness $t > 50$ µm, most of the Casimir torque is felt by a thin layer of thickness $\delta t < 50$ nm. Also, because the total liquid crystal twist through the bulk is less than 45°, the liquid crystal in the region of δt is nearly uniformly aligned. Therefore, we approximate the Casimir torque on this layer from the uniaxial crystal to be the same as that experienced by a uniformly aligned and semi-infinite

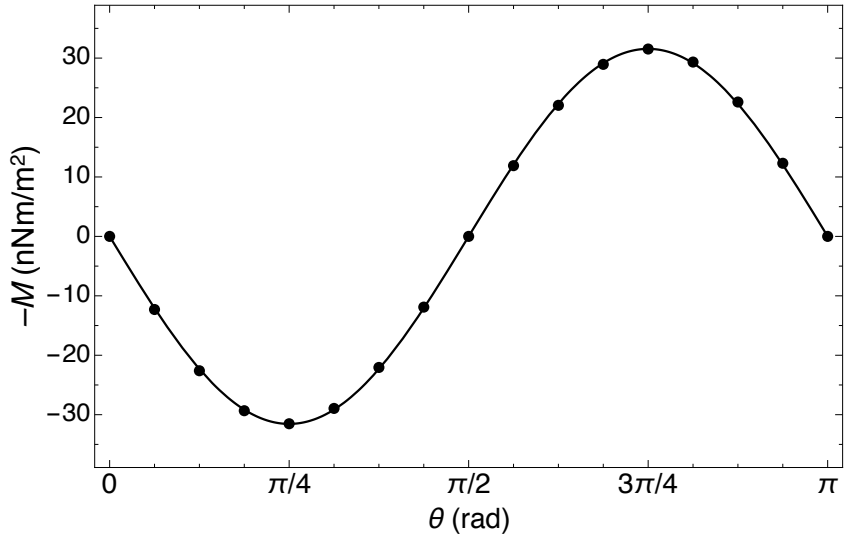

Figure 5.2: Calculated torque between $BaTiO_3$ and uniform 5CB bulk separated by 10 nm of SiO_2 as a function of angle θ between the extraordinary axes of the birefringent materials. The line is a fit to a $\sin(2\theta)$ dependence. The difference between the fit and full calculation is at most 2%, and is less than 0.1% for $\theta = \pi/4$.

liquid crystal slab. These approximations are treated with more detail in Section 5.5.

5.3 Casimir interaction between two infinite slabs

In our regime of interest, the energy has $\sin(2\theta)$ dependence to an excellent approximation, as in Fig. 5.2. The Casimir torque is then

$$M(d,\theta) = -\frac{\partial \Omega}{\partial \theta} \approx a(d)\sin(2\theta), \tag{5.1}$$

where $a(d)$ is a negative for the materials considered here (which have positive birefringence). We use the Ninham-Parsegian oscillator model to describe the dispersion of the solid crystals [104]:

$$\epsilon(i\xi) = 1 + \sum_{j=1}^{N} \frac{C_j}{1 + \frac{\xi^2}{\omega_j^2}}. \tag{5.2}$$

Table 5.1: Model parameters for dielectric functions of relevant materials. Oscillator data for $BaTiO_3$, $CaCO_3$, TiO_2, and SiO_2 are from Ref. [74].

		C_1	ω_1 (eV)	C_2	ω_2 (eV)	C_3	ω_3 (eV)	C_4	ω_4 (eV)
5CB	$\perp$	0.0374	4.40	0.1075	5.91	0.414	9.19	–	–
	$\parallel$	0.0612	4.40	0.1025	5.91	0.460	9.19	–	–
$BaTiO_3$	$\perp$	3595	0.056	4.128	5.54	–	–	–	–
	$\parallel$	145.0	0.138	4.064	5.90	–	–		
$CaCO_3$	$\perp$	5.3	0.177	1.683	10.92	–	–	–	–
	$\parallel$	6.3	0.177	1.182	10.92	–	–	–	–
TiO_2	$\perp$	4.81	5.069	–	–	–	–	–	–
	$\parallel$	5.62	4.516	–	–	–	–	–	–
SiO_2	iso.	0.829	0.057	0.095	0.099	0.798	0.133	1.098	13.39

For the 5CB liquid crystal, we use the dispersive properties at 298.2 K calculated by Kornilovitch using data from Wu [80, 105]. There, the index of refraction is fit with a three-oscillator model, so the dielectric function is:

$$\epsilon_{5\mathrm{CB}}(i\xi) = 1 + 2\sum_{j=1}^{3} \frac{C_j}{1+\frac{\xi^2}{\omega_j^2}} + \left(\sum_{j=1}^{3} \frac{C_j}{1+\frac{\xi^2}{\omega_j^2}}\right)^2 . \tag{5.3}$$

For the birefringent materials, there are separate functions describing the ordinary and extraordinary axes. The model data used for our calculations is summarized in Table 5.1.

The results for the calculated Casimir torque between an infinite half-space of 5CB liquid crystal and an infinite half-space of several birefringent crystals for $\theta = 45^\circ$ are shown in Fig. 5.3. Note that torques per unit area on the order of $10^{-9}\,\mathrm{Nm/m^2}$ are found for separations of $d = 10$ nm.

5.4 Torque balance method for measuring liquid crystal anchoring

The Casimir torque causing a director twist at one boundary competes with the restoring torque from the twisted liquid crystal. The latter is modeled using

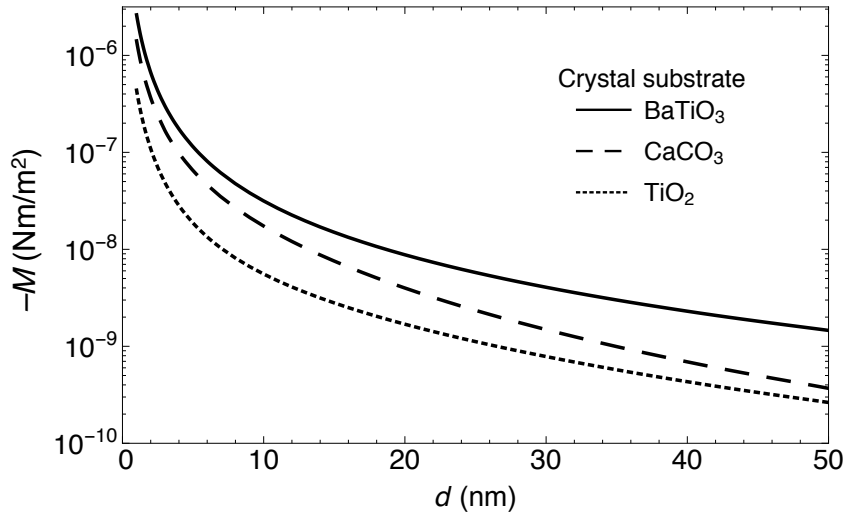

Figure 5.3: Casimir torque per unit area between a half-slab of aligned 5CB and various birefringent crystals, when separated by a SiO_2 layer of thickness d with a relative angle of 45° between the extraordinary axes.

the Frank free energy density, as described in Section 4.2 [87]. In our geometry, the director is always aligned in the $xy-$plane so its orientation can be written in Cartesian coordinates as $\boldsymbol{n} = \{\cos\theta(z), \sin\theta(z), 0\}$. There is no bend or splay of the liquid crystal, so only the twist term contributes to the distortion energy. The twist contribution is given by:

$$F_d = \frac{k_{22}}{2}(\boldsymbol{n} \cdot \nabla \times \boldsymbol{n})^2, \tag{5.4}$$

where $k_{22} = 3.6$ pN is the twist elastic constant of the 5CB [106]. Substituting our expression for $\boldsymbol{n}$, the Frank free energy density is

$$F_d = \frac{k_{22}}{2}\left(\frac{\partial\theta}{\partial z}\right)^2, \tag{5.5}$$

and the Frank free energy per unit area is:

$$E_{\text{elastic}} = \int_0^t F_d \mathrm{d}z = \frac{k_{22}}{2}\int_0^t \left(\frac{\partial\theta}{\partial z}\right)^2 \mathrm{d}z, \tag{5.6}$$

where t is the thickness of the liquid crystal layer. In our geometry (as in Fig. 5.1), the extraordinary axis of the solid crystal is along the x-axis, so the top boundary at $z = d + t$ (where the liquid crystal is in contact with glass) is treated to induce alignment along $\theta(t + d) = \pi/4$.

A torque applied at $z = d$ twists the director to $\theta(d) = \theta_f$. Using calculus of variations, the lowest energy configuration is given by a linear twist, $\theta(z) = \frac{\pi}{4} + \frac{\Delta\theta}{t}(z - d - t)$, where $\Delta\theta = \pi/4 - \theta_f$. The elastic energy of the bulk per unit area is then:

$$E_{\text{elastic}} = \frac{k_{22}}{2}\frac{\Delta\theta^2}{t}. \tag{5.7}$$

If the director at $z = d$ is twisted to θ_f, there is an energy penalty and associated restoring torque at that boundary. The restoring torque of the elastic bulk is given by:

$$M_{\text{elastic}} = -\frac{\partial E_{\text{elastic}}}{\partial \Delta\theta} = -\frac{k_{22}\Delta\theta}{t}. \tag{5.8}$$

M_{elastic} is the torque that must be applied at the boundary $z = d$ to twist the director to $\theta(d) = \theta_f$. The torque applied at the boundary twists the director until the torque balance equation is satisfied: $M_{\text{elastic}} + M_{\text{external}} = 0$. If the Casimir torque is in the approximate form $M_{\text{elastic}} \approx a\sin(2\theta)$, where θ is the angle between the two extraordinary axes of the birefringent materials, then the torque is approximately $M_{\text{Casimir}} = a\sin(2\theta_f) = a\cos(2\Delta\theta)$ (which has the same form as the planar Rapini-Papoular approximation [107]), and the torque balance equation yields:

$$-\frac{k_{22}\Delta\theta}{t} + a(d)\cos(2\Delta\theta) = 0. \tag{5.9}$$

To predict the director twist for our proposed experiment, we calculate $a(d)$ then

numerically solve Eq. 5.9 to find the twist caused by the Casimir torque, $\Delta\theta$. In the proposed experiment, $\Delta\theta$ (or θ_f) will be measured to obtain $a(d)$ via

$$a(d) = \frac{k_{22}}{t}\Delta\theta \sec(2\Delta\theta). \tag{5.10}$$

5.5 The boundary layer approximation

The liquid crystal can be treated as an anisotropic bulk material for the calculation because the twisting is small throughout the thickness that experiences the Casimir interaction. The spacing between the liquid crystal and solid birefringent crystal is on the order of $\sim$ 10 nm, and the liquid crystal layer is about 100 µm thick. Following Parsegian [3], the penetration depth of the Casimir interaction is on the order of the material separation. So, the most important region of the liquid crystal is the 10 nm in contact with the SiO_2 (or conservatively, 100 nm). This 100 nm is the 0.1% of the liquid crystal nearest the birefringent crystal. Because the liquid crystal will be twisted a maximum of $\pi/4$ radians throughout the bulk, the liquid crystal director will vary by a maximum of $\sim 0.05^\circ$ in the relevant region for the Casimir torque, which has no appreciable effect on the torque's magnitude.

This approximation can also be justified by considering the reflection matrix of the liquid crystal stack. The Casimir energy of the system is a function of the reflection matrices of the two materials at the Matsubara frequencies. Our method assumes that, at the Matsubara frequencies, the reflection matrix of the slowly twisted liquid crystal is nearly the same as that of an untwisted, bulk liquid crystal

with the same alignment at the boundary. The first Matsubara frequency at room temperature, $\xi_1 = 2\pi k_B T/\hbar \approx 39$ THz, corresponds to a wavelength of $\lambda_1 \approx 7.7$ µm. The higher frequences correspond to shorter wavelengths, so this first term has the longest penetration depth. We calculated the reflection matrices at this frequency between the twisted and untwisted stacks using the Berreman 4×4 matrix method, and found them to be numerically identical to several significant figures [108]. The Casimir interaction energy is largely unaffected by the slow twist of the liquid crystal throughout the bulk. Hence, to several significant figures, the torque experienced by the liquid crystal layer is felt entirely at the nearest boundary and is only a function of the director orientation at that boundary.

5.6 Proposed experiment

Common methods for fabricating single liquid crystal cells have been previously reported in [109, 110] and can be used for this experiment. A rubbed alignment layer of polyvinyl alcohol (PVA) can be used to cause the liquid crystal molecules to align along the rubbed direction at the surface. The birefringent crystal with a thin, isotropic SiO_2 layer (with thickness $d \sim 20$ nm) is sandwiched with the PVA-treated glass with a spacing of $t \approx 100$ µm (this value can be measured optically). Liquid crystal is then introduced into the cell via capillary action. The filling process may induce some alignment along the direction of liquid crystal flow; however, baking the sample above the liquid crystal clearing temperature (35° C for 5CB) and allowing it to cool slowly will eliminate this

effect. As the liquid crystal cools to room temperature, the director settles into the lowest energy state described in Sec. 5.4. The magnitude of the Casimir torque effect can then be measured by observing the twist of the liquid crystal director.

The final director twist θ_f can be measured optically. This method is similar to a technique for measuring azimuthal surface anchoring strengths of liquid crystals [111, 112]. When linearly polarized light is incident on an adiabatically twisted nematic liquid crystal stack (in which the pitch of the twist is much larger than the wavelength of light), the polarization state is rotated to follow the liquid crystal director. This is known as the adiabatic approximation for twisted nematics and is the principle behind twisted-nematic liquid crystal displays [108]. In this experiment, white light polarized at 45° shines onto the stack as in Fig. 5.1. The Jones vector of this light is $\sqrt{I/2}\begin{pmatrix}1\\1\end{pmatrix}$, where I is the intensity. The light polarization follows the director of the twisted nematic and is incident on the transparent SiO_2 layer with polarization θ_f. Its Jones vector is now $\sqrt{I}\begin{pmatrix}\cos\theta_f\\\sin\theta_f\end{pmatrix}$. In a typical measurement of an anchoring force, the liquid crystal is sandwiched between two glass slides that do not interfere with the polarization state of the light, as in [99]. Then, the polarization state θ_f can be measured with a second polarizer.

To calculate the expected results from an experiment, we consider a liquid crystal layer thickness of 100 µm and calculate the lowest energy state of the system using Eq. 5.9. Figure 5.4 shows expected results for this case. The liquid crystal bulk is predicted to twist by over 35° when the stack is separated by 5 nm from $BaTiO_3$,

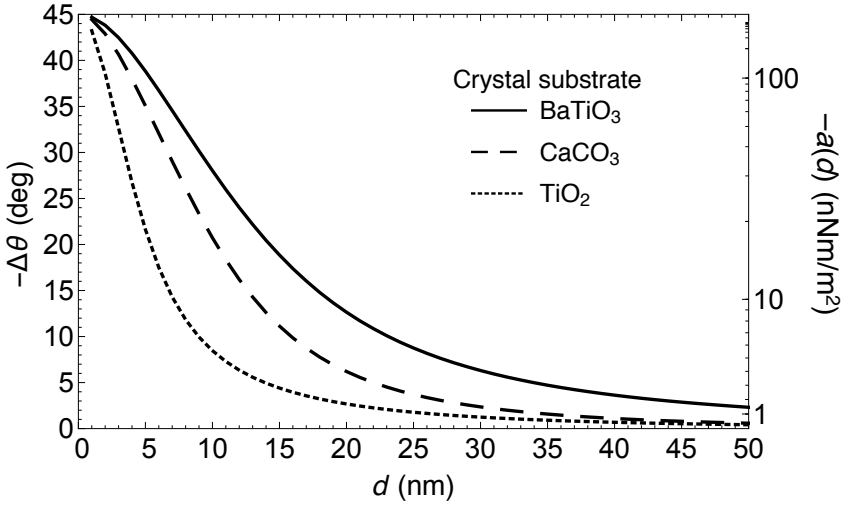

Figure 5.4: Calculated twist of a 100 µm layer of 5CB caused by a Casimir torque induced by various birefringent crystals at distance d from one end of the liquid crystal stack. The incident light is polarized at 45° to the ordinary axis at the top of the 5CB stack, but the director is twisted by the Casimir torque, which causes the light polarization to rotate $\Delta\theta$ towards the extraordinary axis at 0°.

and a twist of several degrees is expected for separations of $d \sim 50$ nm (well into the Casimir regime). When near a birefringent material that has negative birefringence over a large frequency range (such as lithium niobate), the liquid crystal would twist towards the ordinary axis instead of the extraordinary axis. This would provide further confirmation that dispersion effects are causing the director to twist.

5.7 Summary of proposed experiment

We have proposed an experiment for measuring a Casimir torque between a birefringent crystal and a liquid crystal separated by an isotropic spacer layer. We provide complete calculations of the expected results for several materials at a range of separations and include details for a proposed experiment. This experimental design avoids many of the difficulties involved with a torsion pendulum or levitating

microdiscs. Using oscillator models for dispersion fit to experimental data, we have predicted a measurable effect at separations of several tens of nanometers. The Casimir torque could cause a liquid crystal stack to twist by as much as 40° through its bulk. The result would be the first explicit measurement of a Casimir torque.

5.8 Updated experimental details

The Casimir torque measurement evolved in the time since the publication of our first proposal to measure the torque, although the general idea remains the same. Most notably, the spacer layer of SiO_2 deposited with plasma-enhanced chemical vapor deposition (PE-CVD) was not smooth or uniform enough to measure the distance dependence of the torque. The SiO_2 thickness could vary by several nm over even a small cell. Instead, we used a spacer layer of Al_2O_3 deposited with atomic layer deposition (ALD), which reproducibly deposits layers that vary by less than a nm over a cm^2 area. We also used Kapton tape masks to achieve several different thicknesses of Al_2O_3 on each sample. Instead of only using linearly-rubbed PVA alignment layers, we also include circularly-rubbed layers. These allow us to probe the angular dependence of the torque and visualize the broken symmetry caused by the torque. Typically, twisted nematic liquid crystal cells are only a few µm thick. We found that 100 µm thick cells produced nonuniform and unpredictable liquid crystal configurations. We decreased the cell thickness to 50 µm, sacrificing some sensitivity (as the liquid crystal twist is proportional to the thickness) but gaining reproducibility and robustness.

The optical measurement is carried out slightly differently than described in this chapter. It is easier to flip the sample over and set the first polarizer so that the incident light is polarized along the solid crystal's extraordinary axis. This eliminates any additional retardance effect from the thick birefringent crystal, which confounds any polarization measurement. In light of this modification, we clearly define the angles used in the rest of the text in the next section. Lastly, we used different substrates for convenience and cost. The expensive $BaTiO_3$ substrates were replaced with $LiNbO_3$ and YVO_4. The measurement apparatus, which is detailed in the next chapter, was also built after the publication of the paper described in this Chapter.

Chapter 6: Experimental methods for Casimir-Lifshitz torque measurements

6.1 Overview of experiment

An early version of our experimental design, described in Chapter 5, was first published in 2015 [37]. In this chapter and the next, the experiment is described as it was carried out. Figure 6.1 shows the angular variables used in the rest of this work. The coordinate axes are defined such that the extraordinary axis of the solid crystal θ_2 is along the x-axis so that $\theta_2 = 0$. For graphical clarity, this schematic is upside-down compared to the sample as measured on our inverted microscope. The incident white light is linearly polarized along the x-axis so that the birefringent crystal has no effect on its polarization state. The relevant parameters that must be measured optically to extract the Casimir torque are the liquid crystal thickness t and anchoring directions θ_1 and θ_{rub}. In many liquid crystal measurements, a laser is used as the light source. By using white light, we avoid additional effects of coherent interference. Furthermore, the measurement with white light allows us to simultaneously measure liquid crystal thickness and anchoring directions.

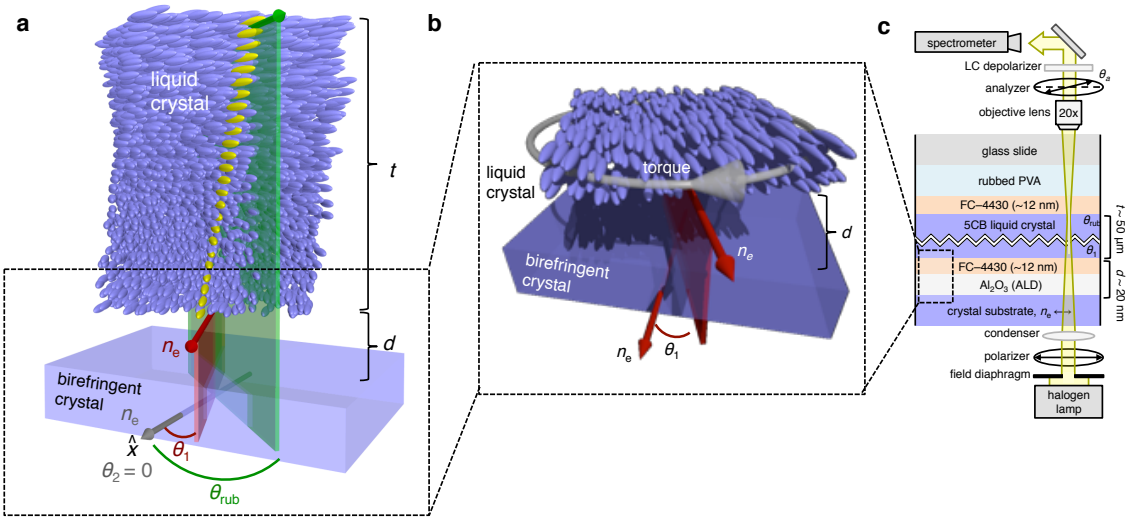

Figure 6.1: a) Illustration showing liquid crystal twist caused by the Casimir torque from a solid birefringent crystal (not to scale, $t \gg d$). b) Zoom on the region of interaction between the solid and liquid crystals c) Optical path and sample cross section.

6.2 Sample fabrication

The samples are created in the Maryland Nanocenter FabLab and characterized in the Munday lab in IREAP. The recipe for constructing a Casimir torque measurement cell is outlined in Appendix A. For all samples in Chapter 7, the 5CB liquid crystal is mixed with FC-4430 fluorosurfactant (3M) at a concentration of 0.5% to prevent sticking to the Al_2O_3 surface [113]. This adds an additional layer between the solid and liquid crystals; we measure its effective thickness with atomic force microscopy in Section 7.5.

6.3 Experimental apparatus

The optical measurement takes place on a Nikon Ti-U Eclipse inverted microscope with a Thorlabs XYR1 stage mounted on top (Fig. 6.2). The XYR1

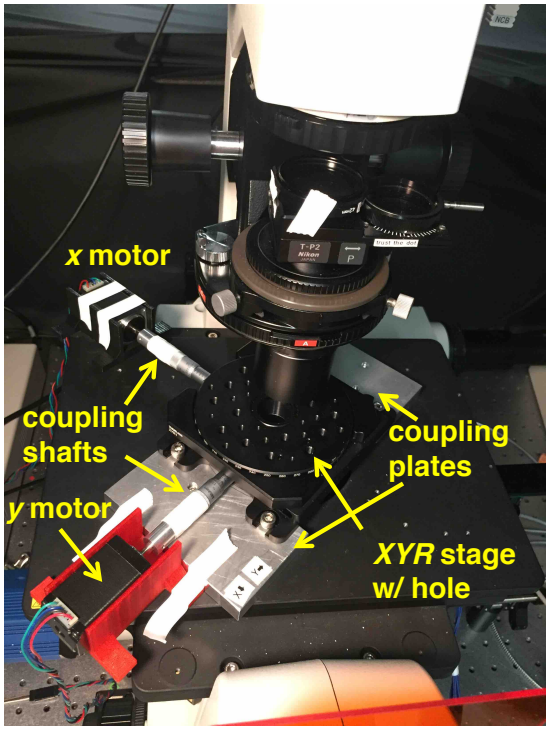

Figure 6.2: XYR stage mounted on Nikon Ti-U Eclipse inverted microscope. Coupling plates were machined to mount the XYR stage at 45° due to space constraints. Stepper motors controlled with Arduino and LabVIEW allow for automated xy-translation. The XYR stage has a 1" threaded hole in the center, and a sample is mounted on the underside near the objective lenses.

stage allows for precision actuation of xy-translation and rotation. The micrometer heads that drive the translation are coupled to stepper motors to allow for automated measurements. A lens tube screws into the bottom of the XYR1 stage, and a retaining ring holds in place a 3D-printed sample mount (Fig. 6.3). Below the objective lens is a rotatable analyzer. The analyzer provided by Nikon is smaller than the slot provided for optical devices, so an adapter was 3D printed (Fig. 6.4). Another stepper motor with attached gear turns the analyzer. A 3D-printing shield that couples an Arduino Nano with three A4988 stepper motor drivers is used to control the motors. This allows us to step any of the three motors with a digital pulse from the Arduino Nano. The Arduino Nano is

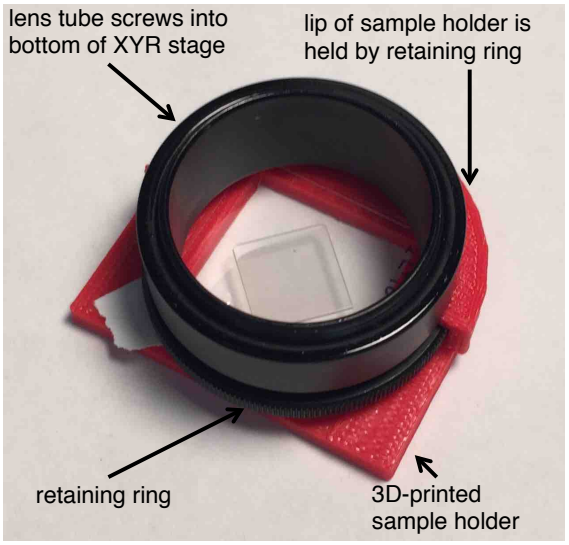

Figure 6.3: A 3D-printed sample mount holds $(22\,\mathrm{mm})^2$ cover slips (the substrates for our samples) and is held by a lens tube with a retaining ring. When the lens tube is screwed into the underside of the XYR stage, the sample can be translated, rotated, and quickly removed by loosening the retaining ring. The small crystal in the center is a $(1\,\mathrm{cm})^2$ birefringent crystal attached to the cover slip.

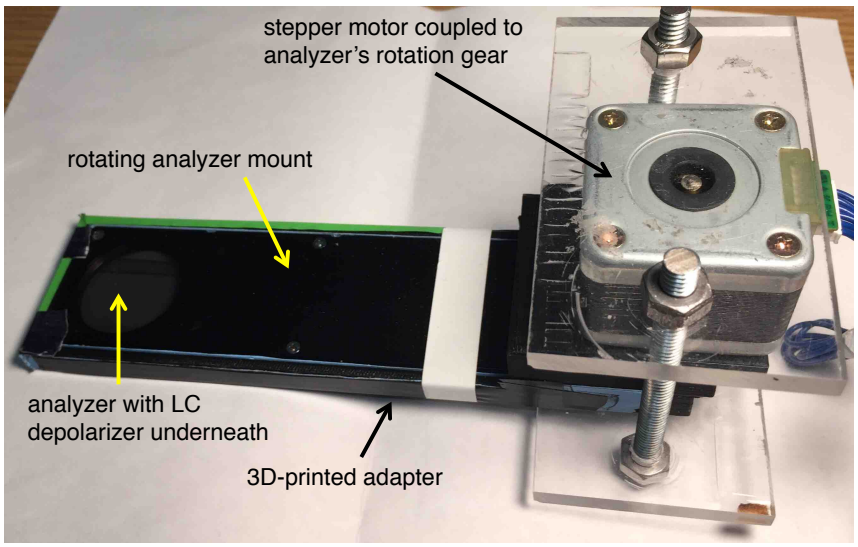

Figure 6.4: Analyzer mounted in a 3D-printed adapter plate and coupled to stepper motor.

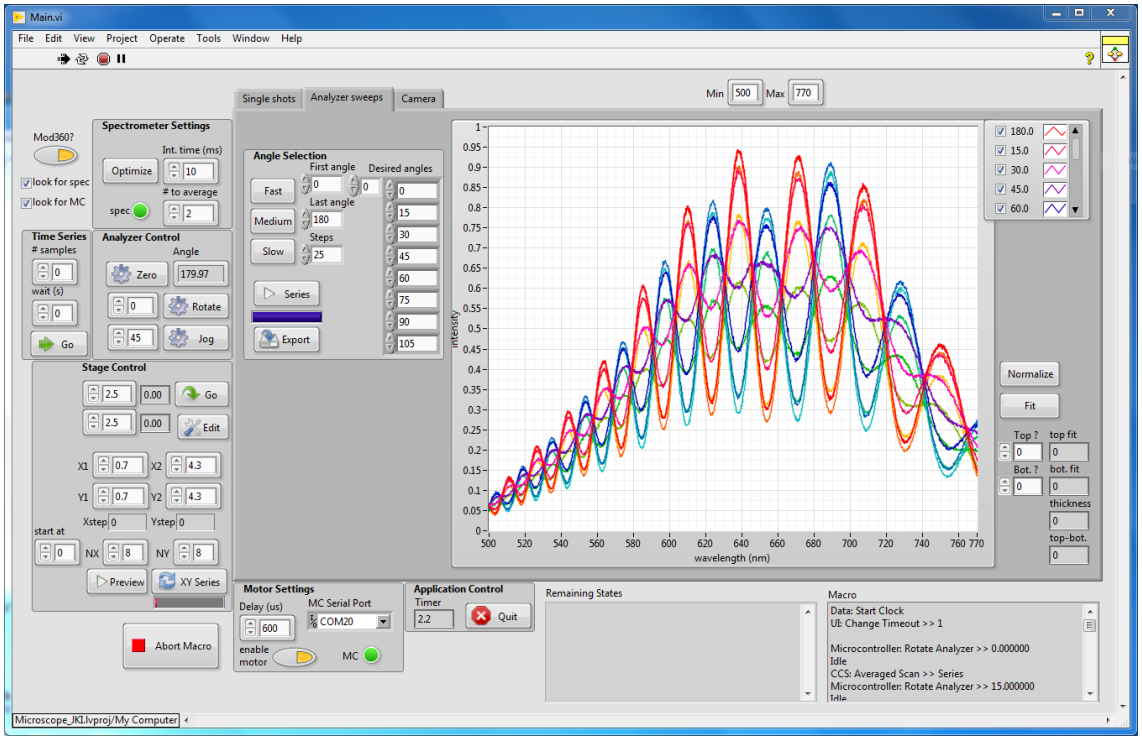

Figure 6.5: Front panel of the LabVIEW program that controls the xy-translation motors, analyzer motor, spectrometer, and CCD camera. The plot shows spectral scans of 25 different spectral measurements of a twisted liquid crystal as the analyzer rotates.

controlled with LabVIEW (National Instruments) using LINX (Digilent). In this way, we can scan over a sample and rotate the analyzer using LabVIEW, which is also used to control a Photometrics CoolSNAP CCD camera and ThorLabs CCS175 spectrometer. Custom macros allow for automated scanning across the sample, rotating the analyzer and taking spectral measurements at each location (Fig. 6.5). The microscope aperture is narrowed to a 400 µm diameter spot size to permit local measurements of liquid crystal behavior. For most of the cm^2 cells, measurements are taken in a 25×25 grid with 25 analyzer angles from 0° to 180° and 25x objective lens. This means that for each sample, 15,625 spectral measurements are taken in about one hour. Before the spectral measurement, a

7×9 grid of images are taken with the camera with a 5x objective lens. These images are are then stitched together to form one large image of the sample. In this way, the xy-location of the measurement can be correlated to a point in an image of the cell.

6.4 Data analysis

Data analysis is carried out in Mathematica. For each sample, the images are stitched together. A locator panel is used to draw regions on the stitched image corresponding to a measurement region (for example, a region with a given Al_2O_3 thickness or the usable region of the sample), as demonstrated in Fig. 6.6. Because

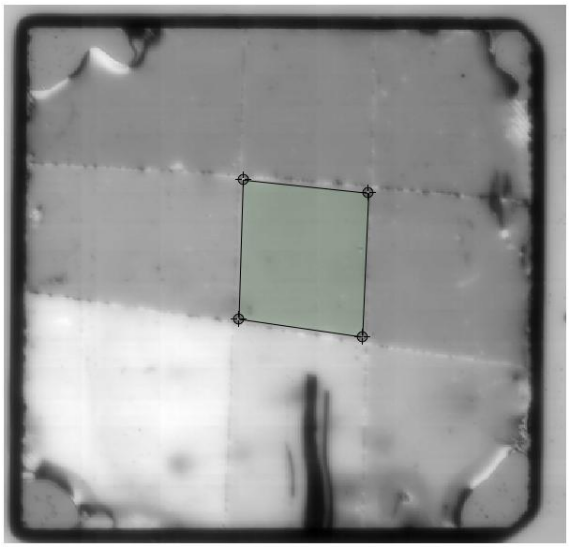

Figure 6.6: In Mathematica, a locator panel is used to define measurement regions of a given sample. Regions with different Al_2O_3 thickness are separated, and unusable regions with obvious defects and scratches (such as the glue spots in the corners or the scratch in the lower, center of this sample) are excluded.

the image coordinates can be correlated to local spectral measurements, the spectral measurements can be separated according to the regions defined in the locator panel.

6.4.1 Fitting procedures

At each measurement location, there are several spectral measurements with different analyzer angles. First, the intensity at each wavelength is normalized by dividing by double the mean intensity across all angles. The maximum intensity cannot be used for normalization because the light is elliptically polarized, but the intensity oscillates about the mean value as the analyzer rotates. Using the Jones analysis developed in Section 4.5, this 2D measurement (intensity I vs. wavelength λ and analyzer angle θ_a) will be fit to the following intensity:

$$I(\theta_a, \lambda) = \left| \begin{pmatrix} \cos^2\theta_a & \sin\theta_a\cos\theta_a \\ \sin\theta_a\cos\theta_a & \sin^2\theta_a \end{pmatrix} M_{\mathrm{LC}} \begin{pmatrix} 1 \\ 0 \end{pmatrix} \right|^2, \tag{6.1}$$

where

$$M_{\mathrm{LC}} = R_{\theta_f} \begin{pmatrix} \cos X - \frac{i\Delta\phi}{2}\operatorname{sinc} X & \Delta\theta \operatorname{sinc} X \\ -\Delta\theta \operatorname{sinc} X & \cos X + \frac{i\Delta\phi}{2}\operatorname{sinc} X \end{pmatrix} R_{-\theta_i}, \tag{6.2}$$

$X = \sqrt{\Delta\theta^2 + \Delta\phi^2/4}$, $\Delta\theta = \theta_{\mathrm{rub}} - \theta_1$, and $\Delta\phi = 2\pi\Delta n t/\lambda$ (the retardance of the liquid crystal layer). Explicitly, the intensity function becomes

$$\begin{aligned} I(\theta_a, \lambda) =& \frac{1}{4}\Delta\phi^2 \operatorname{sinc}(X)^2 \cos^2\left(\theta_a + \Delta\theta - 2\theta_{\mathrm{rub}}\right) \\ &+ \left[\Delta\theta \operatorname{sinc}(X)\sin\left(\Delta\theta - \theta_a\right) + \cos(X)\cos\left(\Delta\theta - \theta_a\right)\right]^2 \end{aligned} \tag{6.3}$$

Several steps are used in the fitting procedure to avoid local minima. The first of these relies on the expansion of $\Delta\phi \gg \Delta\theta$, which using Eq. 4.8 yields

$$I(\theta_a, \lambda) = \frac{1}{2} + \frac{1}{2}\cos\left(2\theta_1\right)\cos\left(2\left(\theta_a - \theta_{\mathrm{rub}}\right)\right) - \frac{1}{2}\cos(\Delta\phi)\sin\left(2\theta_1\right)\sin\left(2\left(\theta_a - \theta_{\mathrm{rub}}\right)\right). \tag{6.4}$$

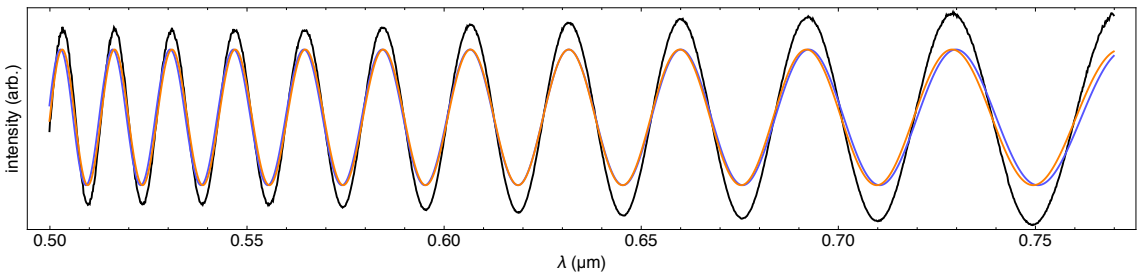

Figure 6.7: The first step of the fitting procedure uses the spectral data at one θ_a (black), fits a thickness using the known Δn of 5CB (blue), then refits for Δn (orange) to ensure that the fit is not confounded by slight variations in birefringence.

Note that the wavelength dependence is wholly contained in the cosine of the retardance $\Delta\phi = 2\pi\Delta n t/\lambda$. Ignoring for now θ_1 and θ_{rub}, we fit for the thickness of the cell by rewriting this equation as $I(\theta_a, \lambda) \approx a + b\cos(\Delta\phi)$, selecting a particular θ_a with highly oscillatory intensity across wavelengths, and fitting the intensity at this θ_a with the known Δn of 5CB [114]. This procedure yields the liquid crystal thickness t independently from its anchoring or twist angles. The next step is somewhat counterintuitive, but can be crucial. After fitting for the thickness, Δn is refit to a phenomenological Cauchy equation[1] (Fig. 6.7). The Δn curve is highly sensitive to small changes in temperature, so even with a good thickness fit, there can be some error in Δn that can have a dramatic effect on the rest of the fitting procedure. As a consistency check, any data where the refitted Δn varies from the known Δn by more than 0.3% at any wavelength is excluded.

With the fitted t and Δn, the measured spectra at all analyzer angles are fit with a least-squares nonlinear fitting algorithm to yield θ_1 and θ_{rub} with a standard error on the order of $< 1°$. The measurement uncertainty corresponding to liquid crystal angles at a single location ($< 10\%$) is small compared to variations across

[1] $\Delta n(\lambda) = B_0 + B_1/\lambda^2 + B_2/\lambda^4$, with fit parameters B_0, B_1, and B_2.

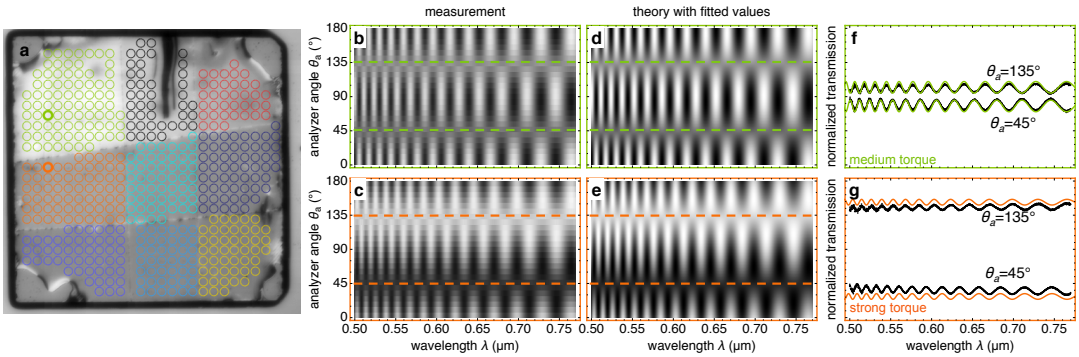

Figure 6.8: Demonstration of the polarized spectrometry measurement. a) Polarized micrograph of a sample with nine measurement regions. b–c) Measured spectra at varying analyzer angles at two locations. d–e) Corresponding fit results to the measured spectra. f–g) Individual measured spectra at the θ_a corresponding to θ_{rub} and $\theta_{\text{rub}} - 90°$.

a measurement region; the measured torques in a single region (consisting of ~ 60 separate measurements) in aggregate typically have a standard deviation of at least 50% of the mean. Therefore, the measurement uncertainty is dominated by the aggregate statistics on measurements in a region, and we ignore the uncertainties from individual measurements.

Figure 6.8 summarizes the measurement procedure on a linearly-rubbed sample with nine different Al_2O_3 thicknesses. Figure 6.8a is a polarized image of the sample with circles corresponding to the spot size of individual measurements. The different colors indicate different regions that have been distinguished as described above (Fig. 6.6). The rest of the figure examines measurements at the two highlighted regions in more detail. In Fig. 6.8b–c, the normalized, measured transmission is plotted as a function of analyzer angle and wavelength at regions with thick (b) and thin (c) Al_2O_3 layers. The dashed lines indicate θ_{rub} and $\theta_{\text{rub}} - 90°$. Figure 6.8d–e plots a simulated spectra from the fit parameters,

showing good agreement to the measured data. The effect of the torque is most easily seen at the measurement where $\theta_a = \theta_{\rm rub}$ and $\theta_a = \theta_{\rm rub} - 90°$. These transmission spectra are plotted in Fig. 6.8f–g. Transmitted intensities (black dots for measured values, solid colored lines for theory fits) along $\theta_a = \theta_{\rm rub} = 135°$ and $\theta_a = \theta_{\rm rub} - 90° = 45°$ are shown for the thick (f) and thin (g) Al_2O_3 layers. A strong torque causes a larger difference in transmission between $\theta_a = \theta_{\rm rub}$ and $\theta_a = \theta_{\rm rub} - 90°$ (for example, see (g) compared to (f)). The slight offset between fit and measurement in Figure 6.8g is because only two out of 25 measurements used in the fit are plotted. Combining all measurements, the error in the angle is $< 4°$.

6.5 Dielectric models

Calculations of Casimir-Lifshitz interactions require the dielectric properties of the relevant materials at all frequencies. The dielectric functions are evaluated at imaginary frequencies $\omega = \mathrm{i}\xi$. The Ninham-Parsegian model for dielectric functions is convenient and consistent with the Kramers-Kronig relations:

$$\varepsilon(\mathrm{i}\xi) = 1 + \sum_j \frac{d_j}{1 + \xi\tau_j} + \sum_j \frac{f_j}{\omega_j^2 + g_j\xi + \xi^2}, \tag{6.5}$$

where the first sum corresponds to microwave-frequency Debye oscillations (with strength d_j and relaxation time τ_j) and the second sum corresponds to damped oscillations (with strength f_j, resonance frequency ω_j, and damping constant g_j) [3]. At room temperature, the first Matsubara frequency is $\xi_1 = 2\pi k_{\rm B}\,(298\,{\rm K})\,/\hbar = 0.161\,{\rm eV}$, well beyond the characteristic frequencies of Debye oscillations (for example, $1/\tau = 65\,\mu{\rm eV}$ for water) [74]. Therefore, the

contributions corresponding to these terms appear only in the zero-frequency terms $\varepsilon(0)$. According to Parsegian and Bergström, inorganic materials can be modeled with reasonable accuracy by considering only two undamped oscillations: one in the infrared and one in the ultraviolet. In this case, the dielectric model can be written

$$\varepsilon(\mathrm{i}\xi) = 1 + \frac{C_{\mathrm{IR}}}{1 + \xi^2/\omega_{\mathrm{IR}}^2} + \frac{C_{\mathrm{UV}}}{1 + \xi^2/\omega_{\mathrm{UV}}^2}, \tag{6.6}$$

where $C_j = f_j/\omega_j^2$ is the contribution of the jth oscillation to $\varepsilon(0)$.

Bergström summarizes a method developed by Hough and White for fitting the measured refractive indices at visible wavelengths to produce complete models in the form of Eq. 6.6 [73]. The visible refractive index is assumed to be dominated by the UV term, so Eq. 6.6 is rewritten (substituting $\xi = \omega/\mathrm{i}$ and $\varepsilon = n^2$) as

$$n^2 - 1 = \left(n^2 - 1\right)\omega^2/\omega_{\mathrm{UV}}^2 + C_{\mathrm{UV}}. \tag{6.7}$$

Using the measured refractive index, Eq. 6.7 is fit for C_{UV} and ω_{UV}. These coefficients are combined with a known $\varepsilon(0)$ and an ω_{IR} estimated from the characteristic absorption frequency to form the complete model. To summarize, ε_0 and ω_{IR} are taken from the literature, C_{UV} and ω_{UV} are fit from the refractive index in the visible regime, and C_{IR} is calculated from $\varepsilon_0 = 1 + C_{\mathrm{UV}} + C_{\mathrm{IR}}$. The parameters resulting from this procedure are listed in Table 6.1. The model used for the intervening dielectric has less effect than those of the birefringent materials; for the Al_2O_3, we use Bergström's model [74].

The liquid crystal 5CB is a special case: some of the assumptions made above do not apply for an organic liquid. We use a dielectric model assembled by

Table 6.1: Oscillator parameters used to model the birefringent crystals and Al_2O_3.

		ε_0	$C_{\rm UV}$	$C_{\rm IR}$	$\omega_{\rm UV}$ (eV)	$\omega_{\rm IR}$ (eV)
$CaCO_3$	$\perp$	7.98	1.69	5.30	11.07	0.177
	$\parallel$	8.48	1.18	6.30	14.12	0.177
$LiNbO_3$	$\perp$	43.69	3.86	38.83	6.65	0.019
	$\parallel$	25.60	3.54	21.06	6.96	0.031
TiO_2	$\perp$	85.77	4.80	80.00	4.97	0.066
	$\parallel$	170.01	6.04	163.00	4.79	0.066
YVO_4	$\perp$	8.93	2.75	5.18	7.19	0.183
	$\parallel$	14.02	3.56	9.46	6.56	0.183
Al_2O_3		10.1	2.07	7.03	13.16	0.066

Kornilovitch using data and fits from Wu *et al.* [80, 105, 115]. We note that Table 1 in Ref. [80] contains typographical errors, confirmed by Kornilovitch in private communication. At 298.2 K, the dielectric models are:

$$\varepsilon_{\rm 5CB,\perp} = \left[1 + \frac{0.414}{1+\left(\frac{\xi}{9.19\,\rm eV}\right)^2} + \frac{0.05960}{1+\left(\frac{\xi}{5.91\,\rm eV}\right)^2} + \frac{0.03737}{1+\left(\frac{\xi}{4.40\,\rm eV}\right)^2}\right]^2 \tag{6.8a}$$

$$\varepsilon_{\rm 5CB,\parallel} = \left[1 + \frac{0.460}{1+\left(\frac{\xi}{9.19\,\rm eV}\right)^2} + \frac{0.10253}{1+\left(\frac{\xi}{5.91\,\rm eV}\right)^2} + \frac{0.11110}{1+\left(\frac{\xi}{4.40\,\rm eV}\right)^2}\right]^2 \tag{6.8b}$$

The dielectric models for all materials are plotted in Fig. 6.9.

Of these materials, $CaCO_3$ is unique in that it has $\varepsilon(0) < 0$ but $\varepsilon(\xi_n) > 0$ for the first few hundred Matsubara frequencies. Consider separately the frequency contributions to the Casimir-Lifshitz torque $M = \sum_{n=0}^{\infty}{}' M_n(\xi_n)$. Because $CaCO_3$ has a different sign of M_0 than for $M_{n>0}$, and the relative contributions of the M_n's depends on the separation of the materials, the sign of the torque between $CaCO_3$ and some another material can change as a function of separation. The possibility of a sign change due to a change in the retardation-dependence frequency sampling was first pointed out by Thiyam *et al.* in a system with black phosphorous and 2D-monolayer phosphorous [14].

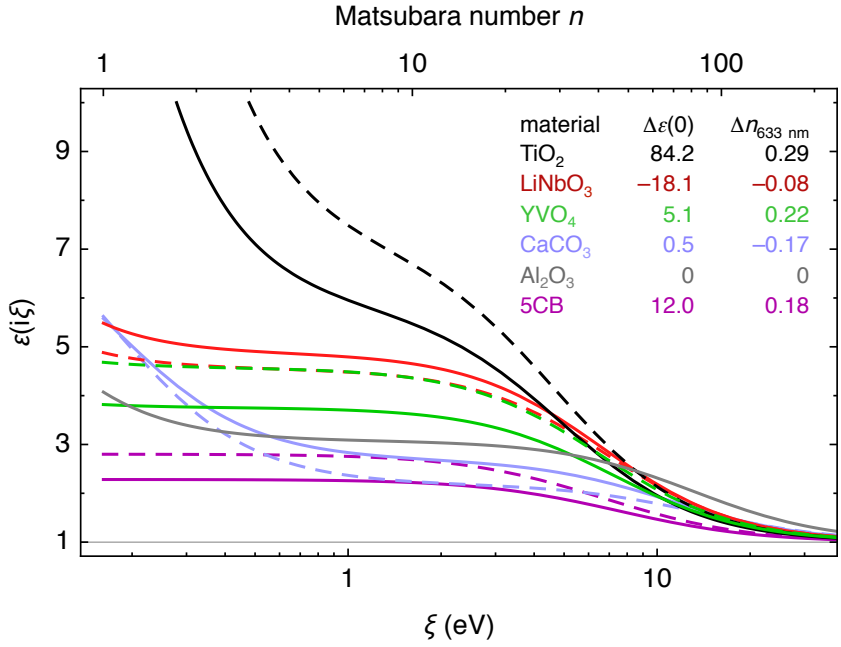

Figure 6.9: The Casimir-Lifshitz free energy is calculated using the dielectric functions of the materials evaluated at imaginary frequencies. For each material, the solid and dashed lines indicate the dielectric function along the ordinary and extraordinary axis, respectively. Al_2O_3 is isotropic and represented by a solid gray line.

Chapter 7: Measured Casimir-Lifshitz torques

7.1 Overview

In this chapter, we summarize the results of the experiment outlined in Chapter 6. With this experiment, we validate the theoretical dependence of the Casimir torque on separation, angle, and optical properties.

7.2 Angular dependence

The measured Casimir torque has a $\sin(2\theta_1)$ dependence for all four birefringent substrates, and the sign and magnitude of the torque depends on the optical properties of the crystals (Fig. 7.1). To probe the angular dependence, we deposit 6 nm of Al_2O_3 on four different birefringent substrates and assemble cells with circularly-rubbed PVA counterplates as described in Chapter 6. This produces a uniform distribution of $\theta_{\rm rub}$, which allows us to measure the torque as a function of θ_1 (see Fig. 6.1). All four crystal substrates show a $\sin(2\theta_1)$ dependence of the torque with a sign corresponding to the rotation needed to align the principal optical axes with the highest refractive index in the visible portion of the spectrum. The microscope images of the samples between crossed polarizers

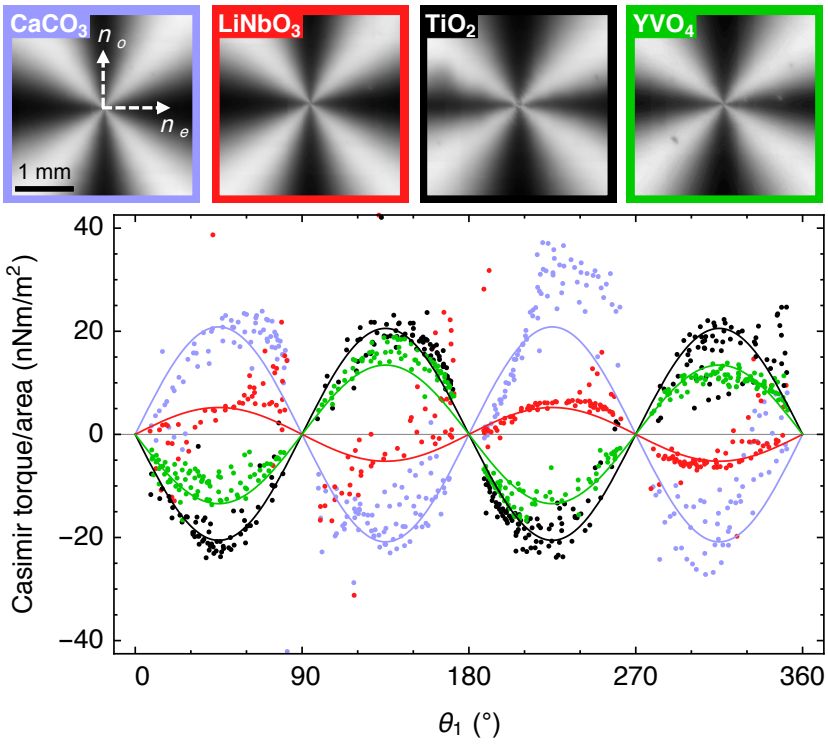

Figure 7.1: Top: Polarized optical micrographs of cells with circularly rubbed PVA and four different birefringent substrates separated by ∼18 nm from the birefringent liquid crystal. In each case, the dark brushes along the preferred axis are narrowed: ordinary axis for $CaCO_3$ and $LiNbO_3$ ($\Delta n < 0$), and extraordinary axis for TiO_2 and YVO_4 which ($\Delta n > 0$). Bottom: Measured torque across each cell as a function of θ_1 (dots). Overlaid are fits (solid lines) to $\sin(2\theta_1)$.

(Fig. 7.1, top panel) show the broken symmetry caused by the Casimir torque: in each case, the dark regions are narrowed along the preferred alignment axis. The data are fit to a $\sin(2\theta_1)$ function to determine the amplitude of the torque (solid lines in bottom panel of Fig. 7.1). We also build circularly-rubbed cells with an isotropic glass substrate replacing the birefringent substrate to demonstrate a null result (Fig. 7.2). For these samples, $\theta_1 \approx \theta_{\text{rub}}$ and $\Delta\theta \approx 0$. The glass slides are coated with either unrubbed PVA, which is known to yield degenerate planar anchoring [93], or 6 nm of Al_2O_3 (as in Fig. 7.1), which should also yield no

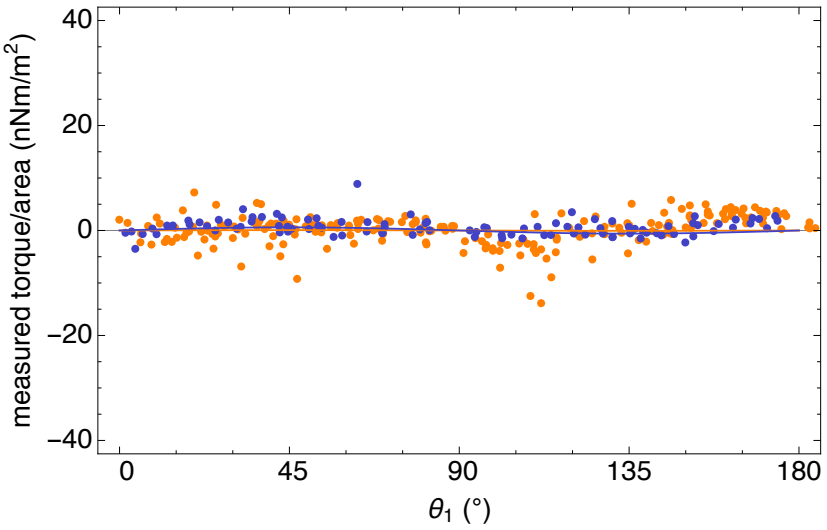

Figure 7.2: Glass substrates are coated with 6 nm of Al_2O_3 (orange) or ∼6 nm PVA (purple). A fit to a $\sin(2\theta_1)$ dependence (solid lines) yields no measurable torque.

preferred azimuthal direction. These measurements confirm that the Al_2O_3 by itself has no anchoring effect on the 5CB.

7.3 Separation dependence

We determine the distance dependence of the Casimir torque using 27 different Al_2O_3 thicknesses (0–25 nm) per crystal substrate and measure the rotation angle to discern the maximum torque at each separation. For these experiments, the PVA layer is rubbed to $\theta_{\text{rub}} \sim 45^\circ$, and nine separations are measured on a single 1 cm^2 sample. Three samples are constructed for each of the four crystal types to achieve 27 distinct separations (Fig. 7.3). The maximum torque per area a for each separation is obtained by calculating the torque associated with the liquid crystal twist and assuming a $\sin(2\theta)$ dependence of the torque:

$$a \sin(2\theta_1) = k_{22}\Delta\theta/t \tag{7.1a}$$

$$a = \frac{k_{22}\Delta\theta}{t \sin(2\theta_1)} \tag{7.1b}$$

To compare these measurements with the full Casimir torque calculation, we include a 12 nm offset to the distance between the interacting crystals due to the surfactant (which we assume to form an isotropic layer of constant effective thickness on the substrate) and sample roughness (Sec. 7.5). Agreement is found between the measured (symbols) and calculated (solid lines) values of the torque to within the uncertainties in the measurements and tabulated optical properties.

7.4 Comparison of measured Casimir torque to calculations

The sign of the Casimir torque depends on the optical properties of the interacting birefringent crystals and can be changed from positive to negative. We categorize these birefringent materials by the sign of the difference in refractive index n (and dielectric constant ε_0) between the ordinary and extraordinary axes for wavelengths in the visible, $\Delta n = n_\mathrm{e} - n_\mathrm{o}$, and at DC, $\Delta\varepsilon_0 = \varepsilon_{0,\parallel} - \varepsilon_{0,\perp}$. TiO_2 and YVO_4 crystals, for which $\Delta n > 0$ and $\Delta\varepsilon_0 > 0$, cause 5CB ($\Delta n > 0$ and $\Delta\varepsilon_0 > 0$) to twist towards the extraordinary axis, resulting in a negative torque (Fig. 7.3). $LiNbO_3$ has $\Delta n < 0$ and $\Delta\varepsilon_0 < 0$ but weaker anisotropy, which causes a smaller twist towards the ordinary axis and a positive torque. $CaCO_3$ ($\Delta n < 0$, $\Delta\varepsilon_0 > 0$) is a special case: low frequency fluctuations should contribute to a torque on 5CB towards the extraordinary axis, while higher frequency fluctuations should contribute to a torque of opposite sign towards the ordinary axis. The full Casimir torque calculation using the available dielectric data predicts that the higher

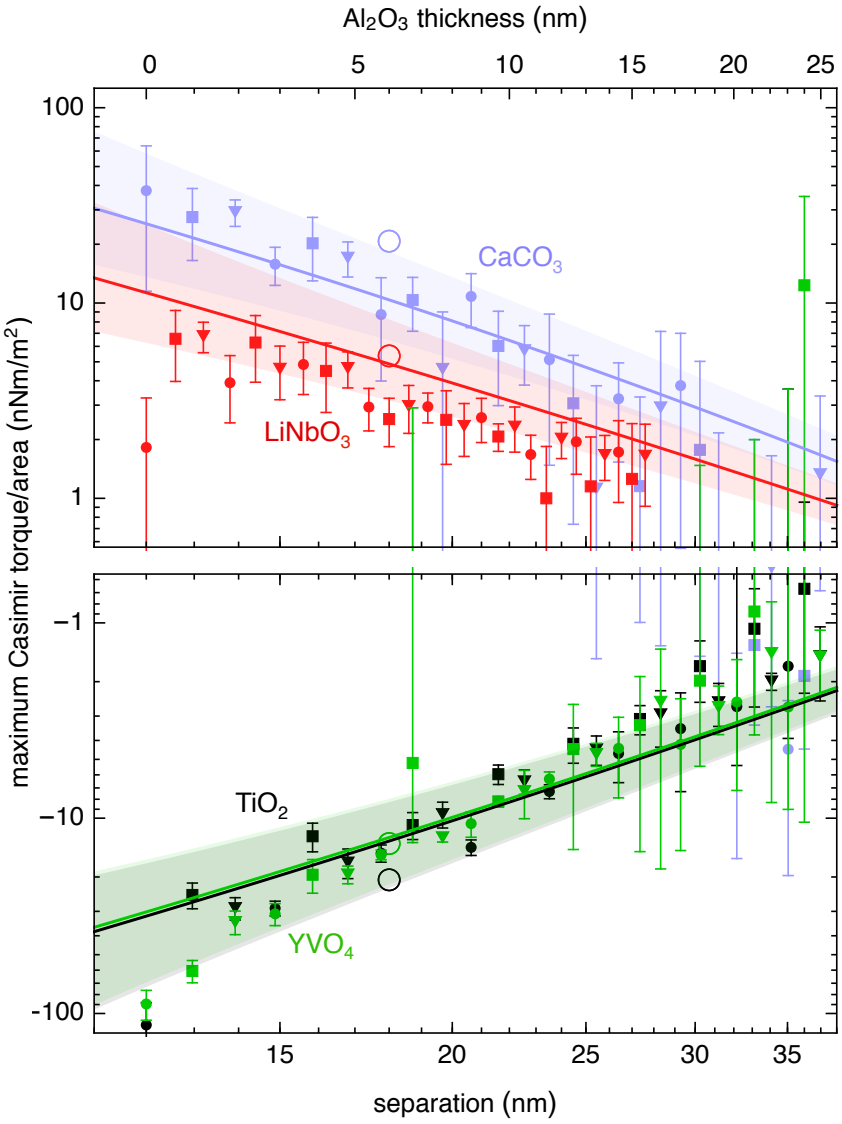

Figure 7.3: Amplitude of the Casimir torque between 5CB and four different birefringent substrates: $CaCO_3$, $LiNbO_3$, TiO_2, or YVO_4, as function of separation. The separation includes the known Al_2O_3 thickness and a constant offset of 12 nm due to the surfactant and surface roughness. Solid lines represent the calculated torque with shaded regions corresponding to the value resulting from a range of constant offsets from 8 nm to 16 nm. Error bars denote the standard deviation of the torques measured at different locations within each region and the symbols (●, ■, ▼) represent different samples of the same crystal type. The open circles (○) represent the torque amplitudes of the fitted $\sin(2\theta_1)$ curves from Fig. 7.1.

frequency terms should dominate at the separations in our experiment, leading to a positive torque. This is also consistent with our measurement, which demonstrates a torque towards the ordinary axis. At larger separations, the lower frequency terms dominate and the sign of the torque should be reversed [14]; however, no crossover behavior is observed (or predicted) within one standard deviation of the data in the distance regime probed in our experiments. Our results are all consistent with the expected signs and relative strengths of the calculated torque. For comparison, the fitted torque amplitudes from the circularly-rubbed samples (Fig. 7.1) are also plotted (open circles) in Fig. 7.3, showing consistency between these different methods.

7.5 Effective distance offset

An atomic force microscope (AFM) is used to probe the thickness of the FC-4430 surfactant layer that forms between the 5CB liquid crystal and solid substrate. The sample was prepared by spreading the 0.5% FC-4430 in 5CB mixture across the substrate (glass or template-stripped Au) to allow for segregation of the materials. The results of these measurements are summarized in Fig. 7.4. In Fig. 7.4a, an AFM topography scan shows the formation of a thin, uniform layer on the glass. We conclude that this layer, which does not appear when 5CB without FC-4430 is spread on a sample, is a monolayer of FC-4430 molecules. In Fig. 7.4b, a line scan across this monolayer shows the step height of the surfactant film on glass (dashed red line in a) to be 4.5 ± 0.3 nm. This measurement puts a minimum bound on the

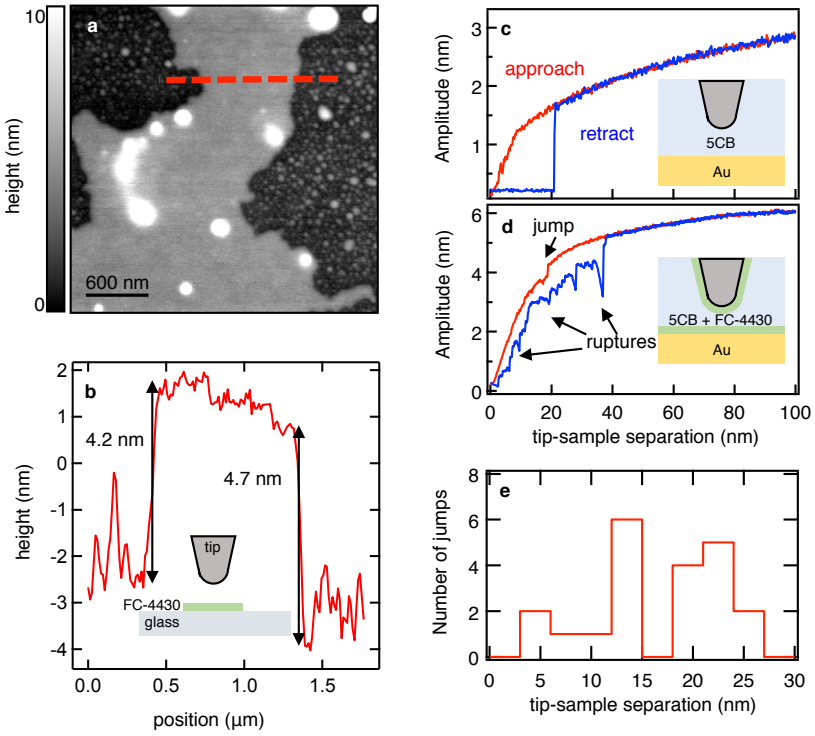

Figure 7.4: a) AFM scan (dynamic mode) of surfactant monolayer (gray) on glass (black) with 5CB droplets observed (white). b) Line scan across surfactant layer. c) Amplitude of piezoelectrically-driven oscillation of a platinum AFM tip approaching the 5CB/gold boundary under 3 V AC bias without any surfactant. d) Amplitude of tip oscillation approaching 5CB/surfactant/gold boundary under 3 V AC bias

surfactant layer thickness, because when immersed in 5CB (as done in the torque experiments), the surfactant molecules will likely extend further from the surface. To determine the total extent of the surfactant *in situ*, a second set of experiments is performed. In Figs. 7.4c, and 7.4d, a platinum AFM tip approaches and retracts from a gold surface while immersed in 5CB without (c) and with (d) the added FC-4430. Figure 7.4c shows smooth amplitude curves except where the tip sticks to the surface after contact (tip-sample separation of zero). Figure 7.4d, shows an amplitude that is observed to decrease rapidly at a certain separation ($\sim$20 nm for this scan), indicating the distance at which the surfactant layers on each surface (substrate and tip) join together (*i.e.*, "jump" to contact). On retraction, multiple features are observed at locations where molecules attached to both surfaces separate (*i.e.*, "rupture"). Figure 7.4e contains a histogram that shows separations at which jumps occur over several distinct distance sweeps for samples with the tip immersed in the FC-4430/5CB mixture. A jump is observed in 21 of 31 approach/retract curves and occurs at an average tip-sample separation of 16.6 nm, which would imply a 8.3 nm surfactant layer on each surface when immersed in 5CB. Considering the measured surface roughness of 4–5 nm, we use a distance offset of 12 ± 4 nm. This offset is added to the Al_2O_3 thickness to yield the separation between liquid and solid crystals. We also note that we calculate the torque as if this spacer layer was entirely Al_2O_3. This has a relatively small effect on the calculated torques. Lacking a dielectric model for the FC-4430, we also calculate the torque with a 12 nm layer of water (a notably strong dielectric) using the dielectric model from Ref. [3]. The calculated torque between YVO_4 and 5CB, for example, decreases by only 6% when

12 nm of Al_2O_3 is replaced with water.

7.6 Measurement sensitivity

In order of decreasing importance, the sensitivity of our measurement is limited by nonuniformities in the liquid crystal cells, the optical measurement technique, and Brownian motion. The first of these is the dominating factor in our measurements and can be estimated by the large-separation torques in Fig. 7.3. At large separations for the $LiNbO_3$, TiO_2, and YVO_4, we can resolve torques of magnitude $3 \times 10^{-9}\,\mathrm{Nm/m^2}$. The $CaCO_3$ substrates, which are softer than the others, are more susceptible to surface defects in fabrication, which limits the sample quality. With an ideal fabrication process that produces uniform and defect-free samples, the optical measurement would limit the sensitivity. From the torque balance equation $a\sin(2\theta_1) = k_{22}\Delta\theta/t$, the smallest measurable torque is limited by the smallest measurable twist angle $\Delta\theta$. For a cell with $t = 50\,\mu\mathrm{m}$, a measurement of $\Delta\theta$ with a resolution of 0.1° corresponds to a torque sensitivity of $10^{-10}\,\mathrm{Nm/m^2}$. The resolution of the torque measurement can be improved by increasing t, but this introduces other practical experimental issues, such as polarization-dependent absorption and long-range liquid crystal defects. If all other factors were mitigated, the minimum noise level of our measurement technique would be dominated by thermal noise of magnitude $k_\mathrm{B}T$. The measured torque per unit area is $k_{22}\Delta\theta/t$, and the free energy associated with the dependent variable $\Delta\theta$ is $k_{22}\Delta\theta^2/(2t)$. Setting this equal to $k_\mathrm{B}T/S$ (where S is the area of the

measured spot size), we find that the minimum resolvable $\Delta\theta$ due to thermal noise is $\sqrt{k_{\mathrm{B}}Tt/(Sk_{22})}$. With $T = 300\,\mathrm{K}$, $t = 50\,\mu\mathrm{m}$, and $S = 1\,\mathrm{mm}^2$, this is about 0.01°, which corresponds to a best possible torque per unit area sensitivity of $10^{-11}\,\mathrm{Nm/m}^2$.

7.7 Summary of results

We have experimentally verified the existence of the Casimir torque between two optically anisotropic materials and have quantified the distance and angular dependence of this phenomenon. With our technique, we can measure torques as small as a few $\mathrm{nNm/m}^2$ and have found the results to agree with calculations of the Casimir torque both in terms of sign and magnitude.

Chapter 8: Future research directions

8.1 Overview

The experimental design and apparatus described in Chapters 6–7 open the door for more measurements of the Casimir torque. During their development, we came across several promising ideas and phenomena that warrant further exploration.

8.2 Next steps for the current measurement apparatus

The results of Chapter 7 represent the first measurements of the Casimir torque, but there are many more measurements that could be carried out immediately. We could explore different sample cleaning procedures and improve the fabrication of the liquid crystal cells. Because sample consistency has the largest effect on our measurement sensitivity, we may be able to resolve smaller torques with less uncertainty by using higher quality samples. With high enough sensitivity, we could test the predictions of Section 3.3, which outlines increases in the torque due to intervening dielectrics and retardation. As an example, we could replace the Al_2O_3 layer with different dielectric films, such as TiO_2, to see if there

is a measurable change in the torque.

With different solid or liquid crystals, we could further explore the role of the dielectric function on the Casimir torque. For example, the common liquid crystal MBBA has $\Delta\varepsilon_0 < 0$ but $\Delta n > 0$. Like $CaCO_3$, the Casimir torque would depend on a balance between low-frequency and high-frequency contributions of opposite sign. Further exploration of the torques using materials with mismatched signs of $\Delta\varepsilon_0$ and Δn may yield a torque that switches sign with a change in separation.

Instead of a birefringent crystal, we could fabricate a surface with metal corrugations or nanorods. A flat surface with 1D conduction should also cause a Casimir torque on liquid crystals. With such an experiment, we could explore the effects of geometric anisotropy on the torque as well as optical anisotropy. The same measurement described in the previous chapters could be used, although the incident light would be polarized perpendicular to the conduction direction in order to transmit into the cell.

8.3 Microdroplets

One promising direction for measuring small torques involves "microdroplets" of liquid crystal on an aligning surface. [92, 116]. The work in this section was done with undergraduate researchers Patrick Goggins and Bart Tararuj as part of PHYS 299B, a research-based course.

A liquid crystal droplet on an aligning surface has a director configuration that depends on the bulk elastic energy and surface anchoring energy. These two

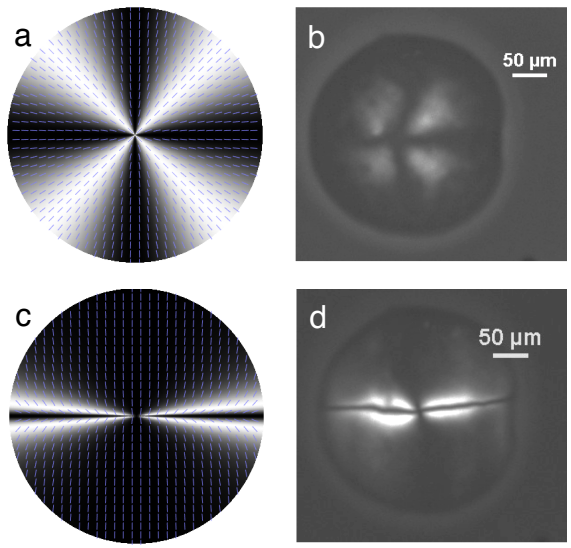

Figure 8.1: Simulation (a,c) and polarized microscopy images (b,d) of liquid crystal hemispheres without (a,b) and with (c,d) alignment on the flat surface. The droplet in b) rests on a substrate that has not been treated for any alignment. The droplet in d) rests on a PVA layer that has been rubbed vertically.

contributions scale differently with the droplet size. The bulk elastic energy will scale with the Oseen-Frank elastic terms (r^{-2} dependence) integrated over the volume (r^3), so $E_{\text{bulk}} \sim r$. The surface anchoring energy contributes a constant amount per unit area so, after integrating over the aligning surface, $E_{\text{surf.}} \sim r^2$. Large droplets have configurations dominated by the surface anchoring and small droplets have configurations dominated by the elastic free energy. At the air interface, the liquid crystal director aligns normal to the liquid-crystal/air interface. With no aligning torque on the flat surface, the droplets form a "hedgehog" structure. With a strong torque, a disclination line forms normal to the direction of the torque. These two orientations are easily distinguished under a polarizing microscope (Fig. 8.1.).

By dimensional analysis, we can estimate that the droplet radius r at which

the two energies are comparable satisfies

$$E_{\text{bulk}} \approx E_{\text{surf.}} \tag{8.1a}$$

$$kr \approx Mr^2 \tag{8.1b}$$

$$r \approx k/M \tag{8.1c}$$

where k is the the elastic constant in the one-constant approximation, *i.e.* $k = k_{11} = k_{22} = k_{33}$, and is on the order of 5 pN. From our dimensional analysis, we can predict that for a Casimir torque of $0.5\,\text{nNm/m}^2$ (smaller than the torques resolved in Chapter 6), there may be a transition from hedgehog orientation to disclination orientation when $r \approx 100\,\mu\text{m}$. Droplets of this size could be easily imaged with our polarizing microscope. By spraying liquid crystal on a surface and taking a large image with hundreds of droplets of different size, we could use image processing techniques to determine the transition size of the droplets. Figure 8.2 is a demonstration of this method. As a 5CB droplet on an aligning surface cools from the isotropic phase, various configurations are apparent. A four-brush texture indicates a hedgehog orientation, while a disclination line indicates an aligned droplet.

Although this experiment is relatively simple, we have made a number of simplifying assumptions. In order to extract a torque from this technique, more careful theoretical work is necessary. For example, the dimensional analysis above needs to be verified with numerical simulations of liquid crystal director orientations. The wetting angle will also play a factor, as the droplets would not have heights equal to their radii. Undergraduate researcher Sean Gillen developed numerical tools

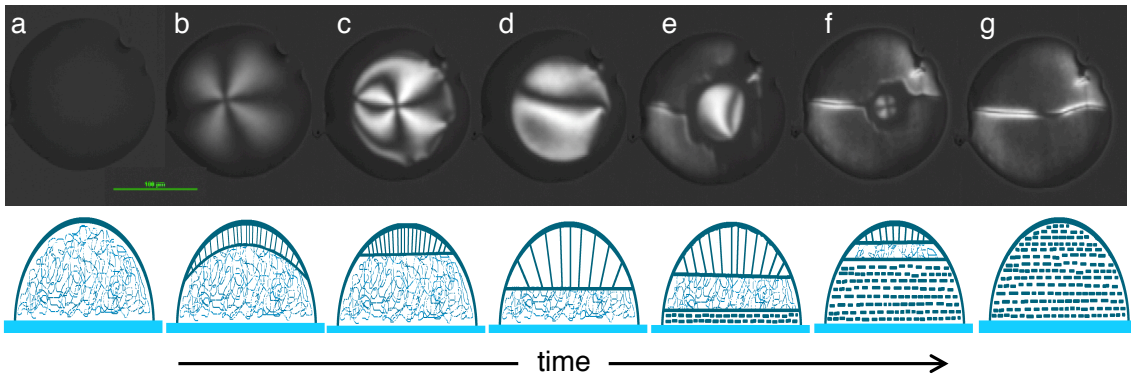

Figure 8.2: Top: Polarized photographs of a single droplet on an aligning surface as it cools from the melted state in a) to an aligned nematic state in g). The top of the droplet appears to cool to the nematic phase, followed by the bottom, then finally the center. b), the bottom layer is still melted and the cooled top layer forms a hedgehog texture. f), a small hedgehog texture in the center is surrounded by a texture that indicates uniform alignment. g) the droplet is cooled to the nematic state and exhibits uniform alignment. Bottom: hypothesized liquid crystal alignment corresponding to the observed textures.

with which we can calculate the director configuration of minimal energy for liquid crystal hemispheres of varying dimensions with varying surface energies, based on the Q-tensor formulation outlined in Ref. [117]. With these calculations, it may be possible to extract a measured Casimir torque from this experiment. Although there are many complications that require further study, the high precision and striking visual effect make this a promising experiment.

8.4 Devices

Because the Casimir torque can cause strong and weak liquid crystal alignment, it may be useful in liquid crystal displays. A birefringent crystal causes liquid crystal alignment with no processing step, which could be appealing compared to fabrication methods that require multiple coatings and rubbing or

UV curing. Twisted nematic displays with weak alignment (which can be achieved with an isotropic spacer layer) can switch more quickly and with lower voltage than those with strong alignment [113]. With a particular cleave of birefringent crystal, the liquid crystal could be aligned at a well-determined tilt angle. The cost of single-crystal birefringent substrates is prohibitive for use in display technologies for the time being, but any birefringent material could be used for liquid crystal alignment.

8.5 Concave droplets

We end this thesis with an open mystery. On several occasions, we noticed a strange behavior of MBBA and 5CB liquid crystals. When a small amount ($\sim$10 µL) was expelled from a pipette tip, it would often form a crater-like droplet as it hung from the tip (8.3). Sometimes, this was preceded by an air bubble that filled out the crater before popping. In an ordinary liquid, the crater-like droplet would collapse to a smooth curved surface due to surface tension. Evidently, this force is somehow opposed by an elastic force unique to liquid crystals. Perhaps the elastic tension due to the director configuration is strong enough to oppose the surface tension. With a repeatable apparatus that could produce this structure under a polarizing microscope, it may be possible to solve this little puzzle.

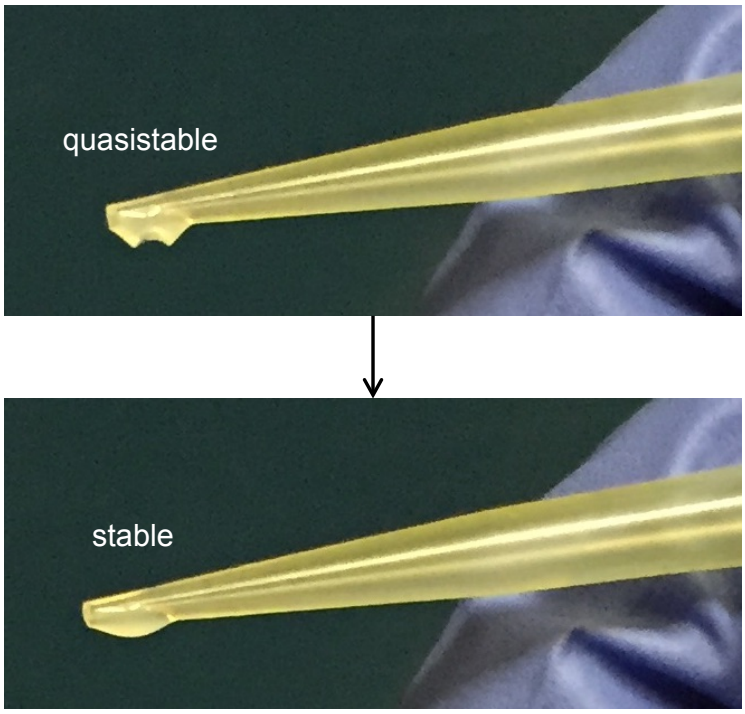

Figure 8.3: A droplet of MBBA liquid crystal hangs from a pipette tip. Sometimes, a quasistable crater-like droplet forms before "popping" to form an ordinary liquid droplet.

8.6 Conclusions

In this Thesis, we have outlined an easier method for calculating Casimir-Lifsthiz interactions in planar systems, demonstrated a few theoretical oddities relating to anisotropic systems, and demonstrated the first working experiment for Casimir torque measurements. We hope that it leads to continued advancements in the field of fluctuation forces and helps to open the door to advanced technologies.

Appendix A: Fabrication techniques

A.1 Atomic layer deposition

The separation between the solid and liquid crystal is controlled by depositing Al_2O_3 layers of varying thickness onto the solid birefringent crystal substrate via atomic layer deposition (ALD). To produce a range of Al_2O_3 thicknesses on a single sample, regions of the substrate are masked using Kapton tape. The Kapton tape prevents Al_2O_3 growth by prohibiting gas flow at the surface and can be easily removed without residue after the deposition process. With Kapton tape masking, nine different thicknesses on a single cell can be achieved with four deposition steps (Fig. A.1). The ALD is done in the Beneq ALD machine in the UMD FabLab at 150 °C and 3 mbar using the recipe "Al2O3_Baseline_150C_1000Cy". The following procedure is carried out for each deposition step:

1. Rinse substrate in acetone, methanol, then IPA.
2. Blow dry with N_2.
3. Place substrates in Ossila UV/ozone cleaner for 3 min.
4. Remove substrates and pressurize the ALD.

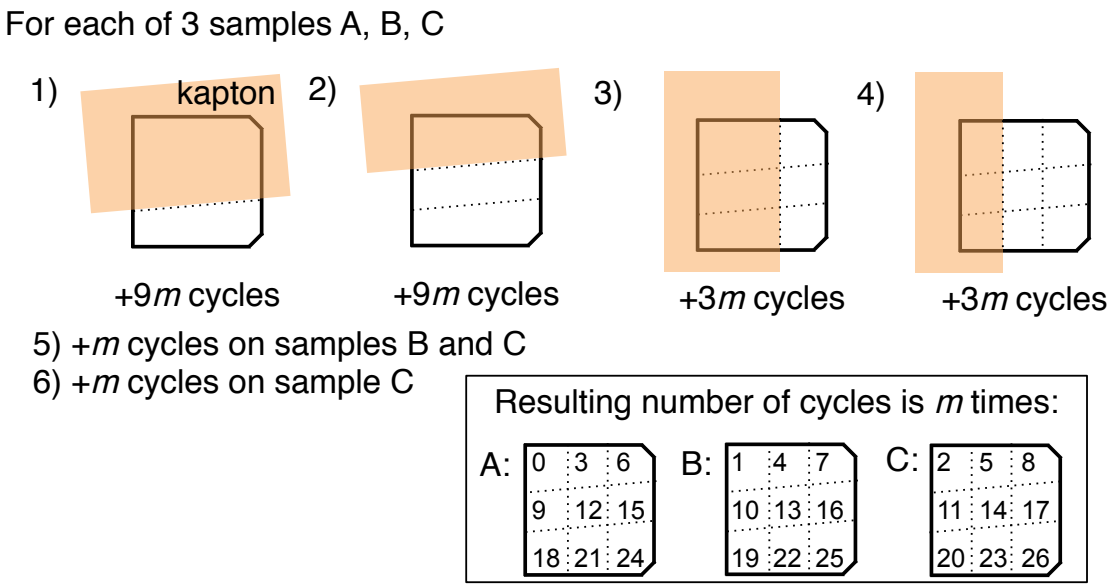

Figure A.1: Process to achieve 27 thicknesses in six ALD processes on three cm^2 substrates (A, B, and C). Kapton tape is used to mask different regions of the substrates in steps 1–4, then additional thin layers are deposited on two of the three substrates in steps 5–6. The Kapton tape leaves visible lines at the edges, so, by applying it at an angle, the front and back of the samples are easily determined. The inset shows the total number of cycles deposited in each region from this process for some integer m.

5. Place Kapton tape on the substrates, taping them onto a clean silicon carrier wafer to prevent sliding.

6. Blow with N_2 to remove dust.

7. Load the samples.

8. Follow the ALD instructions to deposit the desired thickness using the recipe "Al2O3_Baseline_150C_1000Cy" (0.12 nm/cycle).

9. When done, remove the sample from the ALD and peel off the Kapton tape.

The substrates are handled by the edges only to minimize scratches and other defects.

A.2 Polyvinyl(alcohol) alignment layer

The rubbed PVA layers are created on 1" square borosilicate glass cover slides (Ted Pella). The procedure begins in the cleanroom in UMD's FabLab:

1. Wipe slides with dust-free wipes soaked in IPA to remove large particulate.

2. Rinse slides in acetone, methanol, then IPA and dry with N_2.

3. Place slides in UV/ozone cleaner to promote wetting.

4. On the polymer spin coater, static dispense 1% PVA in H_2O to cover the center of the slide.

5. Spin at 2000 rpm for 30 s with 5 s acceleration/deceleration time[1].

6. Bake on hot plate at 105 °C for 30 min to ensure the water has evaporated.

The rubbing is done in our lab. For unidirectional rubbing, the samples are rubbed at least 20 times with a velvet cloth. For circular rubbing, the samples are mounted on a motor while a cloth is lowered into contact with the PVA. The cloth is raised after the sample has completed at least 20 revolutions.

A.3 Cell construction

The samples are assembled in the cleanroom:

1. Reclean the crystal substrate with Al_2O_3 layers (solvent rinse and UV/ozone).

While the substrate is in the UV/ozone cleaner,

2. Blow the rubbed PVA slide with N_2 to remove dust.

3. Mix NOA68 UV-curable adhesive (Norland Optics, purchased from Thorlabs) with 50 µm spacer beads (Cospheric).

Taking the substrate from the UV/ozone cleaner and moving quickly,

4. Place a small dot of NOA68/spacer bead mixture at each corner of the crystal substrate.

[1] the thickness of this layer does not need to be precisely controlled, but this recipe produces thicknesses of ∼150 nm (measured with atomic force microscopy)

5. Use a Milty Zerostat gun on both PVA slide and substrate to reduce static charging (this prevents unwanted static attraction and may also mitigate alignment effects from static charges).

6. Place the rubbed PVA slide facedown on the substrate and gently press together.

7. Use a UV light to cure the glue. A handheld UV light takes about 3 min, and the contact aligner can cure the glue in about 30 s.

8. Place the sample on a hotplate at 50 °C (well above the clearing point of 5CB) with crystal substrate on top.

9. While the sample heats for 1 min, use a pipette to stir the FC-4430/5CB mixture in case the surfactant has settled.

10. Inject the FC-4430/5CB mixture into the cell.

11. Once the capillary action has caused the cell gap to fill completely, carefully wipe away the excess liquid crystal.

12. Turn off the hotplate and allow the cell to slowly cool to room temperature (1 hour).

13. Carry out the optical measurement immediately to avoid long-term degradation of the sample.

Bibliography

[1] H. B. G. Casimir. On the attraction between two perfectly conducting plates. *Proc. K. Ned. Akad. Wet*, 51:793–795, 1948.

[2] Fritz London. The General Theory of Molecular Forces. *Transactions of the Faraday Society*, 33:8b–26, 1937.

[3] V. Adrian Parsegian. *Van der Waals Forces*. Cambridge University Press, Cambridge, 2005.

[4] H.C. Hamaker. The Londonvan der Waals attraction between spherical particles. *Physica*, 4(10):1058–1072, October 1937.

[5] H. B. G. Casimir and D. Polder. The Influence of Retardation on the London-van der Waals Forces. *Physical Review*, 73(4):360–372, February 1948.

[6] E. M. Lifshitz. The theory of molecular attractive forces between solids. *J. Exper. Theoret. Phys.*, 2:73–83, 1956.

[7] I. E. Dzyaloshinskii, E. M. Lifshitz, and Lev P. Pitaevskii. General Theory of Van der Waals' Forces. *Soviet Physics Uspekhi*, 4(2):153–176, February 1961.

[8] Jacob N Israelachvili. *Intermolecular and surface forces*. Academic Press, 1992.

[9] Peter W. Milonni. *The Quantum Vacuum: An Introduction to Quantum Electrodynamics*. Academic Press, Boston, November 1993.

[10] K A Milton. *The Casimir Effect*. World Scientific, October 2001.

[11] V. A. Parsegian and George H. Weiss. Dielectric Anisotropy and the van der Waals Interaction between Bulk Media. *The Journal of Adhesion*, 3(4):259–267, March 1972.

[12] Yu. S. Barash. Moment of van der Waals forces between anisotropic bodies. *Radiophysics and Quantum Electronics*, 21(11):1138–1143, November 1978.

[13] T. G. Philbin and U. Leonhardt. Alternative calculation of the Casimir forces between birefringent plates. *Physical Review A*, 78(4):042107–042107, October 2008.

[14] Priyadarshini Thiyam, Prachi Parashar, K.V. Shajesh, Oleksandr I. Malyi, Mathias Boström, Kimball A. Milton, Iver Brevik, and Clas Persson. Distance-Dependent Sign Reversal in the Casimir-Lifshitz Torque. *Physical Review Letters*, 120(13):131601–131601, March 2018.

[15] L.M. Woods, D.A.R. Dalvit, A. Tkatchenko, P. Rodriguez-Lopez, A.W. Rodriguez, and R. Podgornik. Materials perspective on Casimir and van der Waals interactions. *Reviews of Modern Physics*, 88(4):045003–045003, November 2016.

[16] S. J. van Enk. Casimir torque between dielectrics. *Physical Review A*, 52(4):2569–2575, October 1995.

[17] O. Kenneth and S. Nussinov. New polarized version of the Casimir effect is measurable. *Physical Review D*, 63(12):121701–121701, May 2001.

[18] Cheng Gang Shao, Ai Hong Tong, and Jun Luo. Casimir torque between two birefringent plates. *Physical Review A*, 72(2):022102–022102, August 2005.

[19] J. C. Torres-Guzmán and W. L. Mochán. Casimir torque. *Journal of Physics A: Mathematical and General*, 39(21):6791–6798, May 2006.

[20] J. C. Torres-Guzmán and W. L. Mochán. The Casimir Effect for Arbitrary Optically Anisotropic Materials. *arXiv preprint arXiv:1301.7306*, pages 1–18, 2013.

[21] V. Adrian Parsegian. Nonretarded van der Waals Interaction between Anisotropic Long Thin Rods at All Angles. *The Journal of Chemical Physics*, 56(9):4393–4393, 1972.

[22] Hidefumi Imura. van der Waals-Lifshitz forces between anisotropic ellipsoidal particles. *The Journal of Chemical Physics*, 58(7):2763–2763, April 1973.

[23] Tiago A Morgado, Stanislav I Maslovski, and Mário G Silveirinha. Ultrahigh Casimir interaction torque in nanowire systems. *Optics Express*, 21(12):14943–14943, June 2013.

[24] Robson B Rodrigues, Paulo a Maia Neto, Astrid Lambrecht, and Serge Reynaud. Casimir torque between corrugated metallic plates. *Journal of Physics A: Mathematical and Theoretical*, 41(16):164019–164019, April 2008.

[25] Xiang Chen. Casimir Torque on Two Rotating Plates. *International Journal of Modern Physics B*, 27(14):1350066–1350066, June 2013.

[26] Bing-Sui Lu and Rudolf Podgornik. van der Waals torque and force between dielectrically anisotropic layered media. *The Journal of Chemical Physics*, 145(4):044707, July 2016.

[27] Daniel M. Dryden, Jaime C. Hopkins, Lin K. Denoyer, Lokendra Poudel, Nicole F. Steinmetz, Wai-Yim Ching, Rudolf Podgornik, Adrian Parsegian, and Roger H. French. van der Waals Interactions on the Mesoscale: Open-Science Implementation, Anisotropy, Retardation, and Solvent Effects. *Langmuir*, 31(37):10145–10153, September 2015.

[28] Jaime C. Hopkins, Rudolf Podgornik, Wai-Yim Ching, Roger H. French, and V. Adrian Parsegian. Disentangling the Effects of Shape and Dielectric Response in van der Waals Interactions between Anisotropic Bodies. *The Journal of Physical Chemistry C*, 119(33):19083–19094, August 2015.

[29] Jaehun Chun, Je-Luen Li, Roberto Car, Ilhan A. Aksay, and D. A. Saville. Anisotropic Adsorption of Molecular Assemblies on Crystalline Surfaces. *The Journal of Physical Chemistry B*, 110(33):16624–16632, August 2006.

[30] Je-Luen Li, Hannes C. Schniepp, Ilhan Aksay, and Roberto Car. Phonon-induced anisotropic dispersion forces on a metallic substrate. *Nano LIFE*, 02(02):1240001–1240001, June 2012.

[31] Kyuichi Yasui and Kazumi Kato. Oriented attachment of cubic or spherical batio$_3$ nanocrystals by van der waals torque. *The Journal of Physical Chemistry C*, 119(43):24597–24605, October 2015.

[32] Jeremy N. Munday, Davide Iannuzzi, Yuri Barash, and Federico Capasso. Torque on birefringent plates induced by quantum fluctuations. *Physical Review A*, 71(4):042102–042102, April 2005.

[33] Jeremy N. Munday, Davide Iannuzzi, and Federico Capasso. Quantum electrodynamical torques in the presence of Brownian motion. *New Journal of Physics*, 8(10):244–244, October 2006.

[34] Xiang Chen and John C. H. Spence. On the measurement of the Casimir torque. *physica status solidi (b)*, 248(9):2064–2071, June 2011.

[35] R. Esquivel-Sirvent and George C. Schatz. Van der Waals Torque Coupling between Slabs Composed of Planar Arrays of Nanoparticles. *The Journal of Physical Chemistry C*, 117(10):5492–5496, March 2013.

[36] R. Guérout, C. Genet, A. Lambrecht, and S. Reynaud. Casimir torque between nanostructured plates. *EPL (Europhysics Letters)*, 111(4):44001–44001, August 2015.

[37] David A. T. Somers and Jeremy N. Munday. Rotation of a liquid crystal by the Casimir torque. *Physical Review A*, 91(3):032520–032520, March 2015.

[38] E. R. Smith and B. W. Ninham. Response of nematic liquid crystals to van der Waals forces. *Physica*, 66(1):111–130, May 1973.

[39] Zhujing Xu and Tongcang Li. Detecting Casimir torque with an optically levitated nanorod. *Physical Review A*, 96(3):033843, 2017.

[40] Federico Capasso, Jeremy N. Munday, Davide Iannuzzi, and H. B. Chan. Casimir Forces and Quantum Electrodynamical Torques: Physics and Nanomechanics. *IEEE Journal of Selected Topics in Quantum Electronics*, 13(2):400–414, 2007.

[41] H B Chan. Quantum Mechanical Actuation of Microelectromechanical Systems by the Casimir Force. *Science*, 291(5510):1941–1944, March 2001.

[42] H. B. Chan, V. A. Aksyuk, R. N. Kleiman, D. J. Bishop, and Federico Capasso. Nonlinear Micromechanical Casimir Oscillator. *Physical Review Letters*, 87(21), October 2001.

[43] L. Tang, M. Wang, C. Y. Ng, M. Nikolic, C. T. Chan, A. W. Rodriguez, and H. B. Chan. Measurement of non-monotonic Casimir forces between silicon nanostructures. *Nature Photonics*, 11(2):97–101, February 2017.

[44] T. Emig. Casimir-Force-Driven Ratchets. *Physical Review Letters*, 98(16):160801–160801, April 2007.

[45] D. P. Sheehan. Casimir chemistry. *The Journal of Chemical Physics*, 131(10):104706–104706, 2009.

[46] F. Michael Serry, Dirk Walliser, and G. Jordan Maclay. The role of the Casimir effect in the static deflection and stiction of membrane strips in microelectromechanical systems (MEMS). *Journal of Applied Physics*, 84(5):2501–2501, 1998.

[47] J N Munday, Federico Capasso, and V Adrian Parsegian. Measured long-range repulsive Casimir-Lifshitz forces. *Nature*, 457(7226):170–173, January 2009.

[48] Kellar Autumn, Yiching A. Liang, S. Tonia Hsieh, Wolfgang Zesch, Wai Pang Chan, Thomas W. Kenny, Ronald Fearing, and Robert J. Full. Adhesive force of a single gecko foot-hair. *Nature*, 405(6787):681–685, June 2000.

[49] David A. T. Somers and Jeremy N. Munday. Conditions for repulsive Casimir forces between identical birefringent materials. *Physical Review A*, 95(2):022509–022509, February 2017.

[50] Mark B. Romanowsky and Federico Capasso. Orientation-dependent Casimir force arising from highly anisotropic crystals: Application to $Bi_2sr_2cacu_2o_8$ + *ndelta*. *Physical Review A*, 78(4):042110–042110, October 2008.

[51] A. A. Banishev, J. Wagner, T. Emig, R. Zandi, and U. Mohideen. Demonstration of Angle-Dependent Casimir Force between Corrugations. *Physical Review Letters*, 110(25):250403–250403, June 2013.

[52] Cheng Gang Shao, Da Lei Zheng, and Jun Luo. Repulsive Casimir effect between anisotropic dielectric and permeable plates. *Physical Review A*, 74(1):012103–012103, 2006.

[53] F. S. S. Rosa, D. A. R. Dalvit, and P. W. Milonni. Casimir interactions for anisotropic magnetodielectric metamaterials. *Physical Review A*, 78(3), September 2008.

[54] Ran Zeng, Yaping Yang, and Shiyao Zhu. Casimir force between anisotropic single-negative metamaterials. *Physical Review A*, 87(6):063823–063823, June 2013.

[55] Alejandro W. Rodriguez, David Woolf, Alexander P. McCauley, Federico Capasso, John D. Joannopoulos, and Steven G. Johnson. Achieving a Strongly Temperature-Dependent Casimir Effect. *Physical Review Letters*, 105(6):060401–060401, August 2010.

[56] E. I. Kats. Influence of nonlocality effects on van der Waals interaction. *Sov. Phys. JETP*, 46(1):109–113, 1977.

[57] Astrid Lambrecht, Paulo A Maia Neto, and Serge Reynaud. The Casimir effect within scattering theory. *New Journal of Physics*, 8(10):243–243, October 2006.

[58] John Lekner. Reflection and refraction by uniaxial crystals. *Journal of Physics: Condensed Matter*, 3(32):6121–6133, August 1991.

[59] Qing-Dong Jiang and Frank Wilczek. Chiral Casimir Forces: Repulsive, Enhanced, Tunable. *arXiv:1805.07994 [cond-mat]*, May 2018. arXiv: 1805.07994.

[60] David A.T. Somers and Jeremy N. Munday. Casimir-Lifshitz Torque Enhancement by Retardation and Intervening Dielectrics. *Physical Review Letters*, 119(18):183001, November 2017.

[61] Makoto Ishikawa, Norio Inui, Masaya Ichikawa, and Kouji Miura. Repulsive Casimir Force in Liquid. *Journal of the Physical Society of Japan*, 80(11):114601–114601, November 2011.

[62] Luigi Rosa and Astrid Lambrecht. Repulsive Casimir force: Sufficient conditions. *Physical Review D*, 82(6):065025–065025, September 2010.

[63] Timothy H. Boyer. Van der Waals forces and zero-point energy for dielectric and permeable materials. *Physical Review A*, 9(5):2078–2084, May 1974.

[64] O. Kenneth, I. Klich, A. Mann, and M. Revzen. Repulsive Casimir Forces. *Physical Review Letters*, 89(3):033001–033001, June 2002.

[65] Venkatesh K. Pappakrishnan, Pattabhiraju C. Mundru, and Dentcho A. Genov. Repulsive Casimir force in magnetodielectric plate configurations. *Physical Review B*, 89(4):045430–045430, January 2014.

[66] Michael Levin, Alexander P. McCauley, Alejandro W. Rodriguez, M. T. H. Reid, and Steven G. Johnson. Casimir Repulsion between Metallic Objects in Vacuum. *Physical Review Letters*, 105(9):090403–090403, August 2010.

[67] Mohammad F. Maghrebi. Diagrammatic expansion of the Casimir energy in multiple reflections: Theory and applications. *Physical Review D*, 83(4):045004–045004, February 2011.

[68] Gang Deng, Zhong-Zhu Liu, and Jun Luo. Attractive-repulsive transition of the Casimir force between anisotropic plates. *Physical Review A*, 78(6):062111–062111, December 2008.

[69] Oded Kenneth and Israel Klich. Opposites Attract: A Theorem about the Casimir Force. *Physical Review Letters*, 97(16):160401–160401, October 2006.

[70] R. S. Decca, D. Lpez, E. Fischbach, G. L. Klimchitskaya, D. E. Krause, and V. M. Mostepanenko. Tests of new physics from precise measurements of the Casimir pressure between two gold-coated plates. *Physical Review D*, 75(7):077101–077101, April 2007.

[71] P. J. van Zwol and G. Palasantzas. Repulsive Casimir forces between solid materials with high-refractive-index intervening liquids. *Physical Review A*, 81(6):062502–062502, June 2010.

[72] Mathias Boström, Bo E. Sernelius, Iver Brevik, and Barry W. Ninham. Retardation turns the van der Waals attraction into a Casimir repulsion as close as 3 nm. *Physical Review A*, 85(1):010701–010701, January 2012.

[73] David B. Hough and Lee R. White. The calculation of Hamaker constants from Lifshitz theory with applications to wetting phenomena. *Advances in Colloid and Interface Science*, 14(1):3–41, December 1980.

[74] Lennart Bergström. Hamaker constants of inorganic materials. *Advances in Colloid and Interface Science*, 70:125–169, July 1997.

[75] P. J. van Zwol, G. Palasantzas, and J. Th. M. De Hosson. Influence of dielectric properties on van der Waals/Casimir forces in solid-liquid systems. *Physical Review B*, 79(19):195428–195428, May 2009.

[76] G. G. Gurzadyan and P. Tzankov. Dielectrics and Electrooptics. In Werner Martienssen and Hans Warlimont, editors, *Handbook of Condensed Matter and Materials Data*. Springer Science & Business Media, 2006.

[77] Michael M. Choy and Robert L. Byer. Accurate second-order susceptibility measurements of visible and infrared nonlinear crystals. *Physical Review B*, 14(4):1693–1706, August 1976.

[78] D. Eimerl, L. Davis, S. Velsko, E. K. Graham, and A. Zalkin. Optical, mechanical, and thermal properties of barium borate. *Journal of Applied Physics*, 62(5):1968–1968, 1987.

[79] W. Maier and G. Meier. Eine einfache Theorie der dielektrischen Eigenschaften homogen orientierter kristallinflssiger Phasen des nematischen Typs. *Zeitschrift fr Naturforschung A*, 16(3):262–267, January 1961.

[80] Pavel E Kornilovitch. Van der Waals interaction in uniaxial anisotropic media. *Journal of Physics: Condensed Matter*, 25(3):035102–035102, January 2013.

[81] A. O. Sushkov, W. J. Kim, D. A. R. Dalvit, and S. K. Lamoreaux. Observation of the thermal Casimir force. *Nature Physics*, 7(3):230–233, March 2011.

[82] Mathias Boström and B. E. Sernelius. Retardation-enhanced van der Waals force between thin metal films. *Physical Review B*, 62(11):7523–7526, 2000.

[83] A. Šiber, R F Rajter, R H French, W Y Ching, V A Parsegian, and R Podgornik. Optically anisotropic infinite cylinder above an optically anisotropic half space: Dispersion interaction of a single-walled carbon nanotube with a substrate. *Journal of Vacuum Science & Technology B, Nanotechnology and Microelectronics: Materials, Processing, Measurement, and Phenomena*, 28(3):C4A17–C4A24, May 2010.

[84] Hans Kelker and Rolf Hatz. *Handbook of liquid crystals*. Wiley-VCH, 1980.

[85] Shri Singh and David A. Dunmur. *Liquid Crystals: Fundamentals*. World Scientific, 2002. Google-Books-ID: eAso5CIN44MC.

[86] CW Oseen. The theory of liquid crystals. *Transactions of the Faraday Society*, 29(140):883–899, 1933.

[87] FC Frank. Liquid crystals. On the theory of liquid crystals. *Discussions of the Faraday Society*, 25(1):19–28, 1958.

[88] Shoichi Ishihara. How Far Has the Molecular Alignment of Liquid Crystals Been Elucidated? *Journal of Display Technology*, 1(1):30–40, September 2005.

[89] Hari Singh Nalwa, editor. *Liquid crystals, display, and laser materials*. Number ed. by Hari Singh Nalwa ; Vol. 7 in Handbook of advanced electronic and photonic materials and devices. Acad. Press, San Diego, Calif., 2001. OCLC: 313555778.

[90] E. Dubois-Violette and P.G. De Gennes. Effects of long range van der Waals forces on the anchoring of a nematic fluid at an interface. *Journal of Colloid and Interface Science*, 57(3):403–410, December 1976.

[91] Koji Okano, Naoki Matsuura, and Shunsuke Kobayashi. Alignment of a Liquid Crystal on an Anisotropic Substrate. *Japanese Journal of Applied Physics*, 21(Part 2, No. 2):L109–L110, February 1982.

[92] L. M. Blinov and A. A. Sonin. Anisotropy and effective range of the van der Waals forces of the solid crystalline substrates investigated by means of liquid crystals. *Langmuir*, 3(5):660–661, September 1987.

[93] Jin Seog Gwag, Jae Chang Kim, Tae-Hoon Yoon, and Seong Jin Cho. Effect of polyimide layer surfaces on pretilt angles and polar anchoring energy of liquid crystals. *Journal of Applied Physics*, 100(9):093502–093502, 2006.

[94] M. Nishikawa, B. Taheri, and J. L. West. Mechanism of unidirectional liquid-crystal alignment on polyimides with linearly polarized ultraviolet light exposure. *Applied Physics Letters*, 72(19):2403–2403, 1998.

[95] Byoung Har Hwang, Han Jin Ahn, Soon Joon Rho, Soo Sang Chae, and Hong Koo Baik. Vertical Alignment of Liquid Crystals with Negative Dielectric Anisotropy on an Inorganic Thin Film with a Hydrophilic Surface. *Langmuir*, 25(14):8306–8312, July 2009.

[96] Eugene Hecht. *Optics*. Pearson Education, 2016.

[97] Makoto Yamauchi. Jones-matrix models for twisted-nematic liquid-crystal devices. *Applied Optics*, 44(21):4484, July 2005.

[98] Richard A Beth. Mechanical detection and measurement of the angular momentum of light. *Physical Review*, 50(2):115, 1936.

[99] S. Faetti and G C Mutinati. Light transmission from a twisted nematic liquid crystal: Accurate methods to measure the azimuthal anchoring energy. *Physical Review E*, 68(2):026601–026601, August 2003.

[100] H. M. Wu, J. H. Tang, Q Luo, Z. M. Sun, Y. M. Zhu, Z. H. Lu, and Y. Wei. Liquid-crystal alignment of rubbed polyimide films: A microscopic investigation. *Applied Physics B Laser and Optics*, 62(6):613–618, June 1996.

[101] A. Pizzirusso, R. Berardi, L. Muccioli, M. Ricci, and C. Zannoni. Predicting surface anchoring: molecular organization across a thin film of 5cb liquid crystal on silicon. *Chem. Sci.*, 3(2):573–579, 2012.

[102] Martin Schadt, Klaus Schmitt, Vladimir Kozinkov, and Vladimir Chigrinov. Surface-Induced Parallel Alignment of Liquid Crystals by Linearly Polymerized Photopolymers. *Japanese Journal of Applied Physics*, 31(Part 1, No. 7):2155–2164, July 1992.

[103] Minhua Lu. Liquid Crystal Orientation Induced by van der Waals Interaction. *Japanese Journal of Applied Physics*, 43(12):8156–8160, December 2004.

[104] J. Mahanty and Barry W. Ninham. *Dispersion forces*. Academic Press, London, 1976.

[105] Shin-Tson Wu, Chiung-Sheng Wu, Marc Warenghem, and Mimoun Ismaili. Refractive index dispersions of liquid crystals. *Optical Engineering*, 32(8):1775–1781, 1993.

[106] Takehiro Toyooka, Guo-ping Chen, Hideo Takezoe, and Atsuo Fukuda. Determination of twist elastic constant k_22 in 5cb by four independent light-scattering techniques. *Japanese Journal of Applied Physics*, 26(Part 1, No. 12):1959–1966, December 1987.

[107] A. Rapini and M. Papoular. Distorsion d'une lamelle nématique sous champ magnétique conditions d'ancrage aux parois. *Le Journal de Physique Colloques*, 30(C4):C4–54–C4–56, November 1969.

[108] Dwight W. Berreman. Optics in Stratified and Anisotropic Media: 4x4-Matrix Formulation. *Journal of the Optical Society of America*, 62(4):502–502, April 1972.

[109] Daniel S Miller, Rebecca J Carlton, Peter C Mushenheim, and Nicholas L Abbott. Introduction to Optical Methods for Characterizing Liquid Crystals at Interfaces. *Langmuir*, 29(10):3154–3169, 2013.

[110] Penny S. Hale, Joe G. Shapter, Nico H. Voelcker, Michael J. Ford, and Eric R. Waclawik. Liquid-Crystal Displays: Fabrication and Measurement of a Twisted Nematic Liquid-Crystal Cell. *Journal of Chemical Education*, 81(6):854–854, June 2004.

[111] S. Faetti and C. Lazzari. Measurement of azimuthal anchoring energy in nematic liquid crystals by transmitted and reflected light methods. *Journal of Applied Physics*, 71(7):3204–3204, 1992.

[112] Seo Hern Lee, Tae-Hoon Yoon, and Jae Chang Kim. Determination of azimuthal anchoring energy in a twisted nematic liquid crystal. *Physical Review E*, 72(6):061705–061705, December 2005.

[113] G. P. Bryan-Brown, E. L. Wood, and I. C. Sage. Weak surface anchoring of liquid crystals. *Nature*, 399(6734):338–340, May 1999.

[114] Jun Li and Shin Tson Wu. Extended Cauchy equations for the refractive indices of liquid crystals. *Journal of Applied Physics*, 95(3):896–901, 2004.

[115] Shin Tson Wu. A semiempirical model for liquid-crystal refractive index dispersions. *Journal of Applied Physics*, 69(4):2080–2087, 1991.

[116] O. O. Prishchepa, A. V. Shabanov, and V. Ya Zyryanov. Director configurations in nematic droplets with inhomogeneous boundary conditions. *Physical Review E*, 72(3):031712–031712, September 2005.

[117] Hiroyuki Mori, Eugene C. Gartland, Jack R. Kelly, and Philip J. Bos. Multidimensional Director Modeling Using the Q Tensor Representation in a Liquid Crystal Cell and Its Application to the Cell with Patterned Electrodes. *Japanese Journal of Applied Physics*, 38(Part 1, No. 1A):135–146, January 1999.